

C.2

OCT 26 1981
NOV 18 1981

MAR 24 1989



A Study of Test Techniques for Evaluating Ablative Plasma Engines in Vacuum Test Cells

R. Dawbarn, S. L. Steely,
R. L. McGuire, and L. L. Price
Calspan Field Services, Inc.

October 1981

Interim Report, April 14, 1979 – December 31, 1980

Approved for public release, distribution unlimited.

3
10000-01-0001
**ARNOLD ENGINEERING DEVELOPMENT CENTER
ARNOLD AIR FORCE STATION, TENNESSEE
AIR FORCE SYSTEMS COMMAND
UNITED STATES AIR FORCE**

NOTICES

When U. S. Government drawings, specifications, or other data are used for any purpose other than a definitely related Government procurement operation, the Government thereby incurs no responsibility nor any obligation whatsoever, and the fact that the Government may have formulated, furnished, or in any way supplied the said drawings, specifications, or other data, is not to be regarded by implication or otherwise, or in any manner licensing the holder or any other person or corporation, or conveying any rights or permission to manufacture, use, or sell any patented invention that may in any way be related thereto.

Qualified users may obtain copies of this report from the Defense Technical Information Center.

References to named commercial products in this report are not to be considered in any sense as an indorsement of the product by the United States Air Force or the Government.

This report has been reviewed by the Office of Public Affairs (PA) and is releasable to the National Technical Information Service (NTIS). At NTIS, it will be available to the general public, including foreign nations.

APPROVAL STATEMENT

This report has been reviewed and approved.



KENNETH H. LENERS, Captain, USAF
Directorate of Technology
Deputy for Operations

Approved for publication:

FOR THE COMMANDER



MARION L. LASTER
Director of Technology
Deputy for Operations

UNCLASSIFIED

REPORT DOCUMENTATION PAGE		READ INSTRUCTIONS BEFORE COMPLETING FORM
1 REPORT NUMBER AEDC-TR-81-8	2 GOVT ACCESSION NO.	3 RECIPIENT'S CATALOG NUMBER
4 TITLE (and Subtitle) A STUDY OF TEST TECHNIQUES FOR EVALUATING ABLATIVE PLASMA ENGINES IN VACUUM TEST CELLS		5 TYPE OF REPORT & PERIOD COVERED Interim Report, April 14, 1979 - December 31, 1980
7 AUTHOR(s) R. Dawbarn, S. L. Steely, R. L. McGuire, and L. L. Price, Calspan Field Services, Inc., AEDC Division		6 PERFORMING ORG REPORT NUMBER
9 PERFORMING ORGANIZATION NAME AND ADDRESS Arnold Engineering Development Center/DOT Air Force Systems Command Arnold Air Force Station, TN 37389		10 PROGRAM ELEMENT, PROJECT, TASK AREA & WORK UNIT NUMBERS Program Element 62302F
11 CONTROLLING OFFICE NAME AND ADDRESS Arnold Engineering Development Center/DOS Air Force Systems Command Arnold Air Force Station, TN 37389		12 REPORT DATE October 1981
14 MONITORING AGENCY NAME & ADDRESS (if different from Controlling Office)		13 NUMBER OF PAGES 78
		15 SECURITY CLASS (of this report) UNCLASSIFIED
		15a DECLASSIFICATION/DOWNGRADING SCHEDULE N/A
16 DISTRIBUTION STATEMENT (of this Report) Approved for public release; distribution unlimited.		
17 DISTRIBUTION STATEMENT (of the abstract entered in Block 20, if different from Report)		
18 SUPPLEMENTARY NOTES Available in Defense Technical Information Center (DTIC).		
19 KEY WORDS (Continue on reverse side if necessary and identify by block number) electric propulsion plasma propulsion space chambers spacecraft contamination solid propellant		
20 ABSTRACT (Continue on reverse side if necessary and identify by block number) The Teflon® pulsed thruster is being considered as an attitude control and station-keeping device for spacecraft and satellites. In determining the compatibility of the pulsed plasma thruster with spacecraft systems, it is necessary to assess the potentially harmful effects the exhaust products may have on various spacecraft surfaces. Previous efforts to acquire data in space environmental chambers have had limited success due to the interferences caused by exhaust products scattering from the test facility walls and		

UNCLASSIFIED

20. ABSTRACT, Concluded.

pumping panels. The overall objective of this effort is to define the operating characteristics of prototype pulsed plasma engine and a test facility configuration suitable for contamination-type tests. The immediate objectives of the work reported herein are as follows: 1) to use a micropound and a millipound pulsed plasma engine to obtain information on the species in the plasma and how they react when they encounter the test chamber walls, and 2) to examine the effectiveness of possible diagnostic techniques; these include witness plates, electron multipliers, mass spectrometers, Faraday cups, attenuated total reflectance (ATR) plates, calorimeters, and UV spectroscopy.

UNCLASSIFIED

PREFACE

The work reported herein was performed by the Arnold Engineering Development Center (AEDC), Air Force Systems Command (AFSC) for the Air Force Rocket Propulsion Laboratories, Edwards Air Force Base, California. Lieutenant R. Furstenau was the AFRPL project manager. The planning and research phases of the project were carried out by Sverdrup Technology, Inc., AEDC Group (a Sverdrup Corporation Company), operating contractor for Aeropropulsion Testing at the AEDC, AFSC, Arnold Air Force Station, Tennessee, under project number V34M-28. The report was prepared by Calspan Field Services, Inc., AEDC Division, operating contractor for the Aerospace Flight Dynamics testing effort at the AEDC, under the project number D220VW. Captain Kenneth H. Leners, AEDC/DOT was the Air Force project manager. The manuscript was submitted for publication on April 6, 1981.

CONTENTS

	<u>Page</u>
1.0 INTRODUCTION	7
2.0 APPARATUS	
2.1 Pulsed Plasma Engines	8
2.2 Molecular Beam Vacuum Chamber	9
2.3 Instrumentation	10
3.0 PROCEDURES AND RESULTS	
3.1 Operation of the Plasma Engines	11
3.2 Species Produced by the Engine	15
3.3 Energy Accommodation Coefficient	38
3.4 Velocity of Plasma	41
3.5 Plume Profiles	45
3.6 Contamination Measurements	47
4.0 ANALYSIS OF BAFFLE SYSTEMS FOR ENGINE TESTS	
4.1 GUMRAP Computer Code	59
4.2 System Modeling	64
4.3 Results of the Cryopumping Simulation	68
5.0 SUMMARY	
5.1 Operation of Plasma Engines	71
5.2 Species Produced by the Engine	71
5.3 Energy Accommodation Coefficient	71
5.4 Velocity of Plasma	71
5.5 Plume Profile	72
5.6 Contamination Measurements	72
5.7 Analysis of Baffle Systems	72
6.0 CONCLUSIONS	73
REFERENCES	76

ILLUSTRATIONS

Figure

1. Schematic of Plasma Engine	9
2. Schematic of Vacuum Chamber	10
3. Photopulse and Ion Signal from Micropound Engine	11
4. Faraday Cup Signal from Millipound Engine (Short Electrodes)	12
5. Millipound Engine Firing	13

<u>Figure</u>	<u>Page</u>
6. Current Pulse (Plasma Engine)	14
7. Faraday Cup Signal from Millipound Engine (Long Electrodes)	15
8. Vapor Pressures of Pyrolysis Products	16
9. Mass Spectra from Vacuum Pyrolysis of Teflon®	16
10. Vacuum Chamber Pressure History	17
11. Mass Spectra from Engine Pulses (300°K Cryoliner)	19
12. Mass Spectra from Engine Pulses (77°K Cryoliner)	20
13. Mass Spectrometer Data: Partial Pressure Profiles from a Single Engine Pulse	20
14. Plan View of Optics for UV Spectrometer (Typical)	23
15. Representative Spectra (Micropound Engine)	24
16. Mercury Lamp Spectrum for Wavelength Calibration (Micropound Engine)	24
17. Wavelength Calibration (Micropound Engine)	25
18. Correction Terms for Wavelength Calibration	27
19. Calibration Curves	28
20. Intensifier Spectra	29
21. UV Spectra on Tri-X Film	33
22. Ceramic Insulator in Engine (Mykroy Material)	35
23. Electron Multiplier Signal	36
24. Engine Installation	38
25. Flat Plate Calorimeter	39
26. Angular Dependence of Energy Accommodation	40
27. Conical Calorimeter	40
28. Plasma Velocity	42
29. Velocity Profile (Horizontal)	43
30. Chopper Wheel	43
31. Plume Profile of Micropound Engine	45
32. Plume Profile of Millipound Engine (Vertical)	46
33. Plume Profile of Millipound Engine (Horizontal)	46
34. Plume Profile (Coil) (Horizontal)	47
35. IR Absorption Spectra of Contaminant and Fuel	48
36. IR Absorption Spectra of Contaminant and DC 704 Oil	49
37. IR Absorption Spectra of Deposit and Teflon® Fuel	50
38. IR Absorption Spectrum of C ₂ F ₄	51
39. IR Absorption Spectrum for C ₂ F ₆	52
40. Glass Sampling Slides on Nozzle	53
41. Particles from Engine	53
42. View of Single Droplet Deposited on Slide	54

<u>Figure</u>	<u>Page</u>
43. Droplets Viewed under SEM	55
44. Carbon Particles on Sample Plate (Mag. 120X)	56
45. Carbon Particles on Sample Plate (Mag. 1200X)	57
46. Carbon Flakes on Anode	57
47. 12V Chamber and Baffle System	58
48. Entrance Aperture and Molecular Beam Geometry	63
49. Coordinate Systems for Gas-Surface Interaction	64
50. Example of Chamber Configurations Modeled Using GUMRAP	65
51. Chamber Configurations (CC) Modeled Using GUMRAP	66

TABLES

1. Species Identification for Micropound Engine Plasma	25
2. GUMRAP Predictions for Energy Accommodation	41
3. Percent of Molecules Reaching the Exit Plane	69
NOMENCLATURE	77

1.0 INTRODUCTION

Electric propulsion engines using an inert fuel such as Teflon® and acquiring energy from the sun via solar panels offer lightweight, trouble-free, and extremely long-lived attitude control thrusters. The first generation of these thrusters is approaching operational status, and therefore there is a need for adequate ground test facilities to fully assess their performance in a space environment. In particular it is necessary to determine the potentially harmful effects the exhaust products may have on various spacecraft surfaces. Of special interest is the nature and the quantity of material which might be deposited in the backflow region of the engine. A requirement for making meaningful backflow contamination tests in a space simulation facility is that none of the plume species which leave the motor must rebound off the chamber walls or internal structure and return to the backflow region. Limited testing by both Fairchild, Inc. and the Jet Propulsion Laboratories have shown that the high velocity plasma pulse cannot be pumped on traditional cryopanels.

From the test effort described herein, there is also strong evidence of erosion of material from surfaces exposed to the more energetic core flow of the plasma. This suggests that material collected in the backflow region in previous tests was a composite of true backflow contamination, plasma material reflected from the chamber end walls, and materials sputtered from test chamber surfaces. For a successful evaluation of the amount of backflow contamination which might be expected from these engines when they are operating in a true space environment, all reflections and chamber-induced contaminants must thus be eliminated or suppressed to such a level that they can be distinguished from the actual backflow.

In previous work at AEDC it has been observed that collimated high-energy molecular beams (N_2 at 2 km/sec) are reflected from engineering surfaces with a strong specular lobe (Ref. 1). At these energies, the data have indicated an energy accommodation of approximately 85 percent. Experiments with similar high-energy beams directed at cryosurfaces showed an initial capture of the major portion of the beam with a slight specular reflected lobe. It was noted, however, that after a cryodeposit had started to form, the effective capture coefficient dropped drastically and the major portion of the beam was reflected (or possibly sputtered) in a specular lobe (Ref. 2). Extrapolating this information to the high velocity plasma would suggest specular reflections with zero capture regardless of the surface temperature. The possibility of specular reflections at the first surface encounter offers some hope of using a baffle system to control the main pulse of the plasma and thus to prevent its return to the backflow region of the engine.

The successful design of such a system, however, is strongly dependent on knowing the properties of the plasma and the plasma-surface interactions in more detail. The work reported in this document was performed to provide more information on the characteristics of the pulsed plasma engines operating in a vacuum test cell. The data are presented along with some preliminary conclusions and should be accepted as a status report of a continuing study.

Two sizes of pulsed plasma engines were used during these tests. The micropound engine was supplied by the Air Force Rocket Propulsion Laboratories (AFRPL) and refurbished at AEDC. The millipound engine was a refurbished engine built by Fairchild, Inc. and supplied by AFRPL.

The tests were performed in the AEDC Aerodynamic Molecular Beam Chamber, which was modified for this program. Along with the installation and operation of the engines, a companion effort was made to evaluate various diagnostics which might be useful both in these experiments and in future contamination tests.

2.0 APPARATUS

2.1 PULSED PLASMA ENGINES

A block diagram showing the components which are basic to both engines is presented in Fig. 1. The capacitors are connected directly to the engine electrodes. They are charged from a high voltage power supply. When the engine is in a vacuum environment, this voltage is not high enough to break down and arc across the electrodes.

The engine is fired by initiating a trigger pulse to a spark plug located in the gap between the electrodes. This provides a burst of electrons and ions sufficient to start the discharge of the main capacitors. The main discharge occurs across the face of the Teflon "fuel" rods and in the process removes a thin layer of the Teflon. The large current flowing in the arc produces a strong magnetic field which drives the flowing ions and electrons down the electrodes. The accelerated plasma arc leaves the end of the electrodes at high velocity, and the net momentum gained by the engine can be equated to that given to the plasma pulse. After a plasma pulse, the capacitors are recharged in readiness for the next pulse.

The main differences between the micropound and millipound engines are the quantity of energy stored in the capacitors and the electrode "fuel" geometry. The Teflon is fed from the rear in the micropound engine and from the side in the millipound engine.

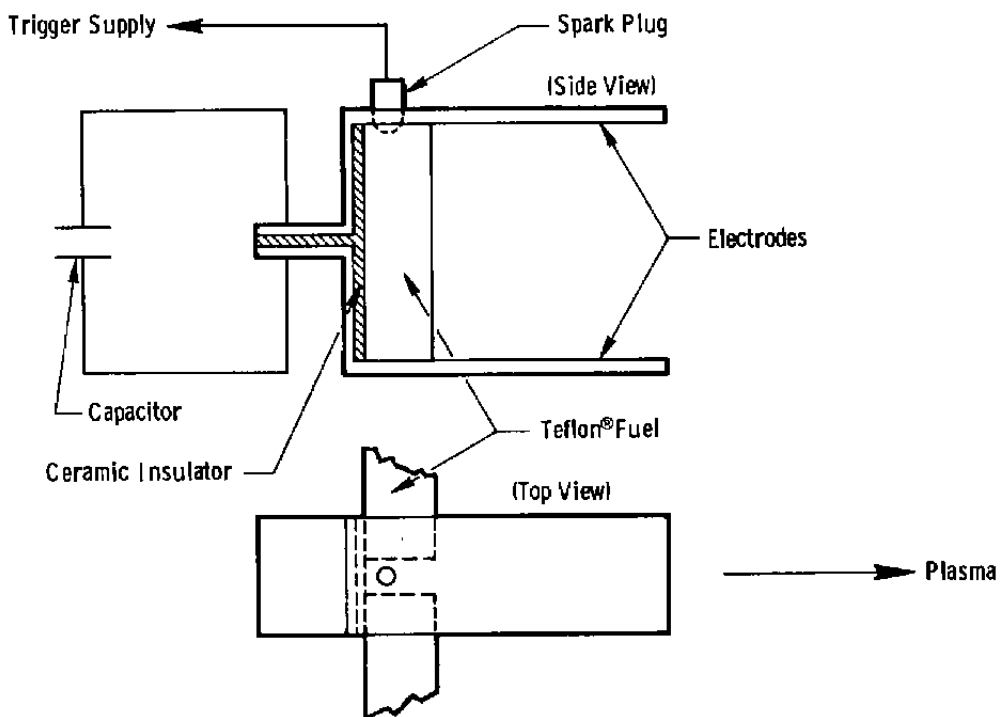


Figure 1. Schematic of plasma engine.

2.2 MOLECULAR BEAM VACUUM CHAMBER

The AEDC molecular beam chamber was modified slightly to conduct these experiments. A schematic of the chamber with the pulsed plasma thruster installed is shown in Fig. 2. The chamber is actually two separately pumped vacuum sections coupled via a small skimming orifice. The engine section had an LN_2 -cooled copper liner and was pumped with 6-in. diffusion pumps. Its base pressure in this configuration was 5×10^{-7} torr. As each motor was tested it was mounted on a rotatable positioning device. The axis of rotation was located through the exit plane of the electrode. A rotary feedthrough was used to position various devices into the plasma plume.

The test end of the vacuum chamber is pumped by a 10-in. and a 6-in. diffusion pump and has two LN_2 -cooled scavenging panels. Its base pressure in this configuration is 1×10^{-7} torr. A secondary collimating skimmer was installed for these tests. The instrument mounting platform in the test section can be remotely positioned in the X-Y plane. The Z-positioning mechanism and the rotary table were removed in order to provide more room on the platform for mounting a variety of diagnostic instruments. An extension tube was attached to the test end of the vacuum chamber in order to provide a longer flight distance for plasma velocity measurements.

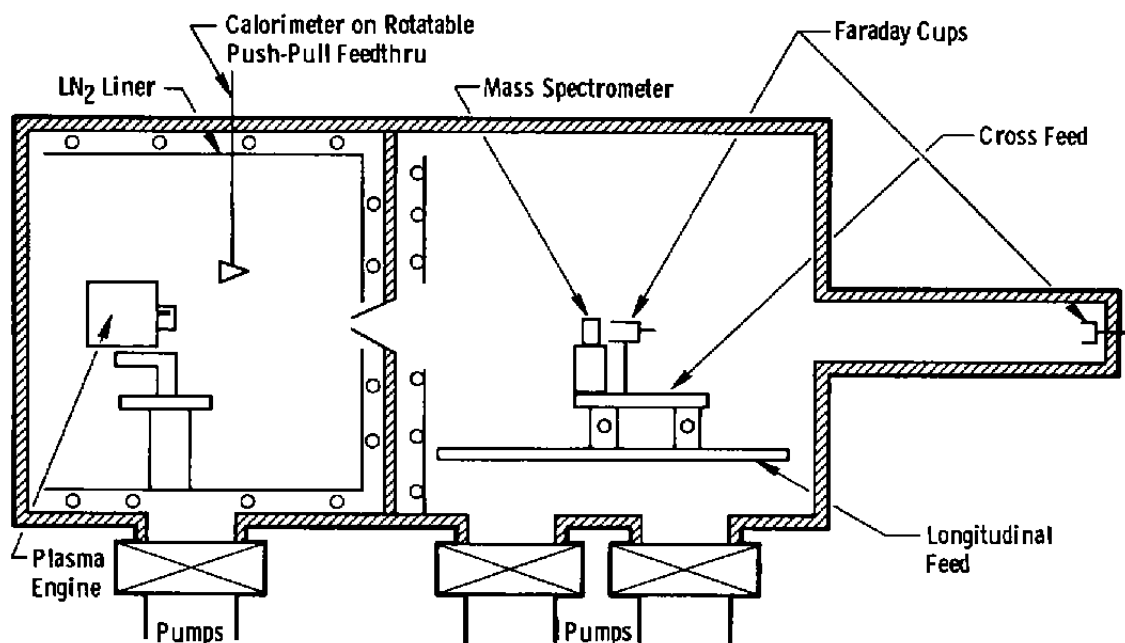


Figure 2. Schematic of vacuum chamber.

2.3 INSTRUMENTATION

The standard instrumentation on the vacuum chamber consists of Alphatron® and ion gages used to monitor vacuum conditions and thermocouples which record cryopanel temperatures. The additional instruments used for this test series are briefly noted at this point and are described in more detail in that portion of the text where they are the focal point of the specific measurement. These instruments included a quadrupole mass spectrometer with a mass range from 2 to 500 amu. When the mass spectrometer was installed on the X-Y traversing mechanism, the additional cabling reduced the effective mass range to 5 to 100 amu, which prevented any monitoring of the H₂ peak.

Faraday cups were used to detect both ions and electrons. Several designs, including ones with suppressor grids and deflection plates, were evaluated.

Calorimeters were built and installed to measure accommodation coefficients and to map the plasma flow field. Two types were used, flat discs and cones.

Attenuated total reflectance (ATR) plates were used to collect contaminant material in the chamber. These plates were operated at 300°K; they were removed from the vacuum system after a test sequence and were analyzed in a Beckman IR spectrometer. Absorption bands in the range from 2.5 to 50 μ m were recorded.

A UV spectrometer was used to view the plasma pulse as it was generated between the electrodes of the engine. The spectra from the micropound engine were low resolution and were taken primarily to check the feasibility of recording single-pulse data. A high resolution instrument was used to record spectra from the millipound engine.

3.0 PROCEDURES AND RESULTS

3.1 OPERATION OF THE PLASMA ENGINES

The micropound engine was installed in the vacuum chamber to be used as a source of typical gases which might be produced by the larger engines. The engine was not instrumented, and little information is available on the characteristics of its discharge cycle. The visible light output from the engine was monitored with a photomultiplier and is shown on the lower scope trace (Fig. 3). This indicates a single plasma pulse of approximately 20- μ sec duration. The positive ion signal collected by a Faraday cup located downstream of the engine is presented in the upper trace and also indicates a single plasma pulse. Repeated shots showed considerable variation in the intensity of both signals even though the capacitors were charged to a uniform 1500 volts. A typical chamber pressure rise after engine firing was from 5×10^{-7} torr to 5×10^{-6} torr. This was primarily mass 28 with no positive identification of mass peaks associated with Teflon. Later data indicate that this pressure rise was predominantly caused by the plasma's sputtering gases from the vacuum

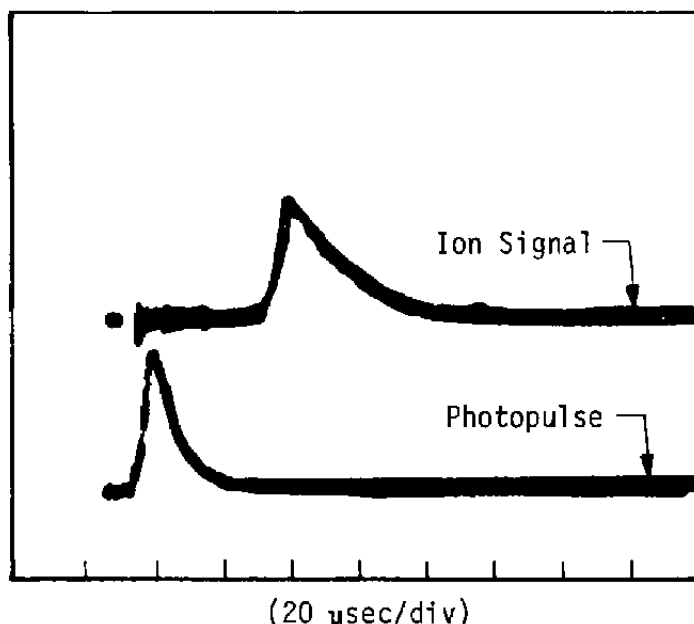


Figure 3. Photopulse and ion signal from micropound engine.

chamber walls. A miniature calorimeter was inserted into the plasma and recorded temperature rises of a few tenths of a degree Kelvin. These temperature rises were much more repeatable on a pulse-by-pulse basis than was expected from the variable Faraday cup data.

The first millipound engine was received after being used for tests at the NASA Jet Propulsion Laboratory (JPL). It had short electrodes, the anodes of which were heavily eroded. The engine was installed in the test cell, and after some minor problems with the charging and trigger circuits, the unit was operated. The first obvious difference was the intensity of the plasma source. The photomultiplier tube became completely saturated even with a total of 10^{-5} neutral density filters. The signals at the Faraday cup consisted of an initial small, negative signal from electrons produced by the UV photons followed by the arrival of the slower, positive ions. These signals are reproduced in Fig. 4 and indicate a

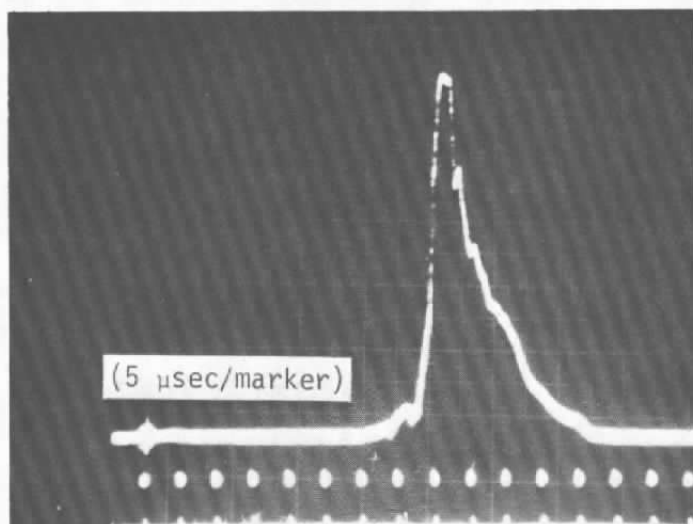


Figure 4. Faraday cup signal from millipound engine (short electrodes).

strong initial pulse. These data show that the intense pulse of the millipound engine has a much narrower width than that of the micropound engine. Several diagnostic techniques were tried in succession to determine feasibility. The UV spectrometer provided strong signals indicating C^{+++} , C^{++} , C^+ , F^+ , and F , as well as the H_α line. The mass spectrometer detected species at masses 12, 16, 28, 31, 48, and 69 which include the first indication of carbon-fluorine species. The calorimeter recorded temperature rises of $23^\circ K$. The pulses for the millipound engine were generally much more reproducible than those for the micropound engine for all data systems.

Before any sets of comprehensive data could be taken the engine was recalled for further tests at JPL, and a new millipound engine was supplied by Fairchild. The new engine had an identical capacitor bank and Teflon fuel feed system. The prime difference was in the length of the electrodes (≈ 6 in.) and the fact that these electrodes were enclosed with a more confining nozzle. The new engine was mounted in a 2 deg of freedom gimbal system and installed in the test chamber. Signals received by such instruments as the Faraday cups and electron multiplier were much more complex for this engine. Sufficient neutral density filters were used to obtain a photopulse; these data, along with a rate of change of current trace from an internal coil built around one of the electrodes, are presented in Fig. 5. It was understood that this coil was a Rogowski coil and thus should provide a direct measurement of the current flow. The shape of the data, especially the instantaneous rise at time zero, strongly suggested that the coil was a simple loop with a pulse transformer and thus was measuring the rate of change of current flow. The data were thus integrated, and the current flow is shown in Fig. 6.

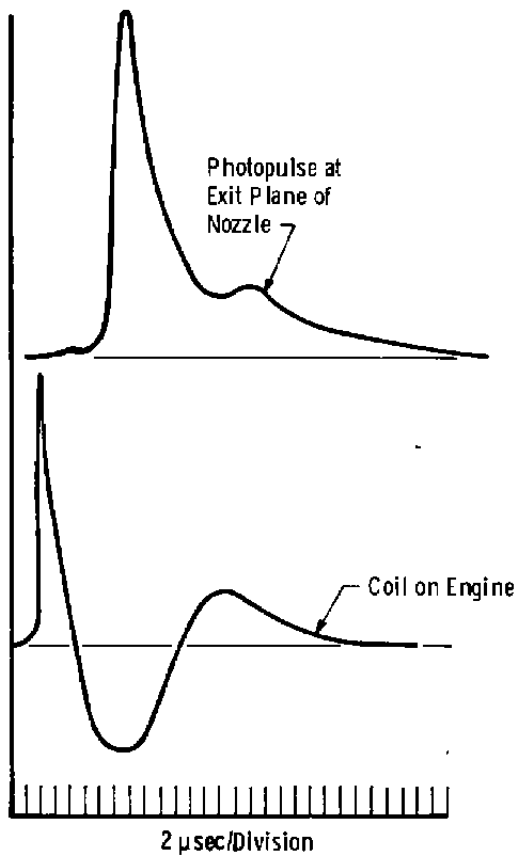


Figure 5. Millipound engine firing.

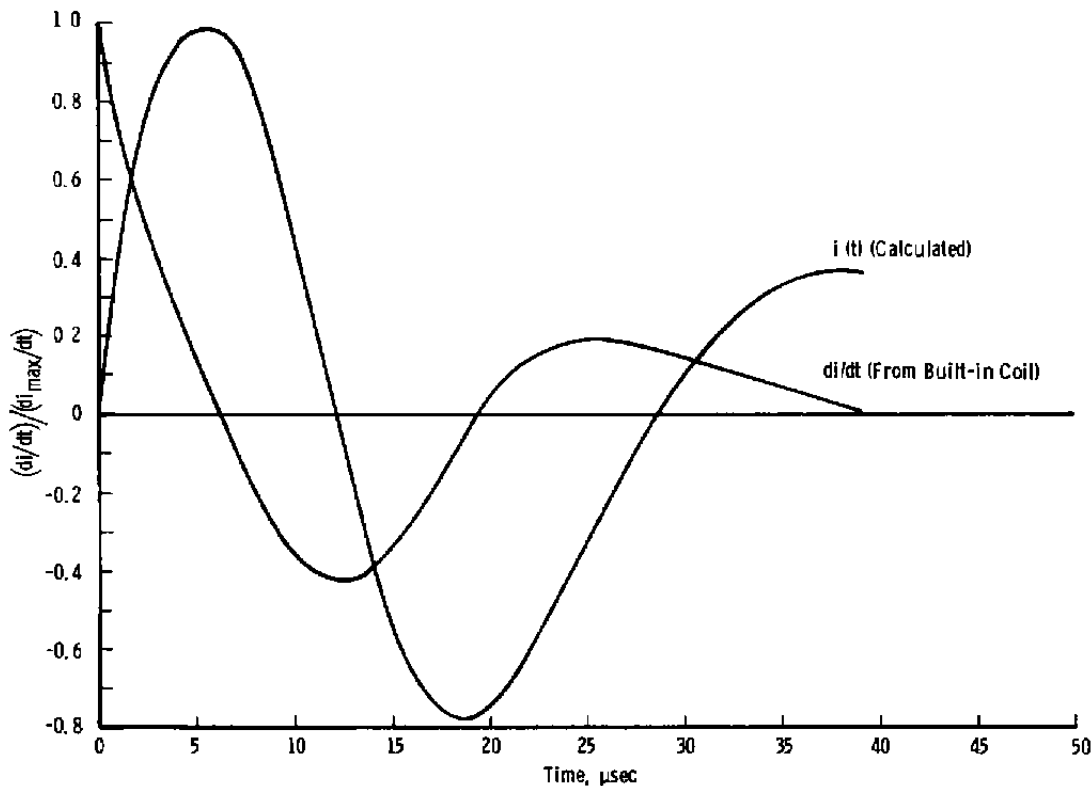


Figure 6. Current pulse (plasma engine).

The known value of the capacitance, the observed frequency (which can be seen to be varying slightly during the discharge cycle), and the measured decay were used in the equation for a damped oscillator to determine approximate values of inductance and resistance of the engine and plasma. It was found that in order to reproduce the observed damping and frequency change one could consider the discharge to consist of three separate plasma discharges, where the inductance varied linearly from 5×10^{-8} to 8×10^{-8} Henrys during each cycle and the resistances of the plasma discharges were 1.9×10^{-3} ohms and 5.9×10^{-3} ohms for the first two pulses and a greater value for the third discharge. The last resistance would not be calculated since there was insufficient signal to determine the frequency during this part of the cycle.

Evidence of the reality of a triple discharge is contained in the photopulse and is also reflected in the complex signal detected by the Faraday cup (Fig. 7). It appears that with this engine, more plasma is contained in the second and third periods of the discharge than with the previous short electrode engine. Unfortunately, there is insufficient data from the short electrode engine to make a positive comparison.

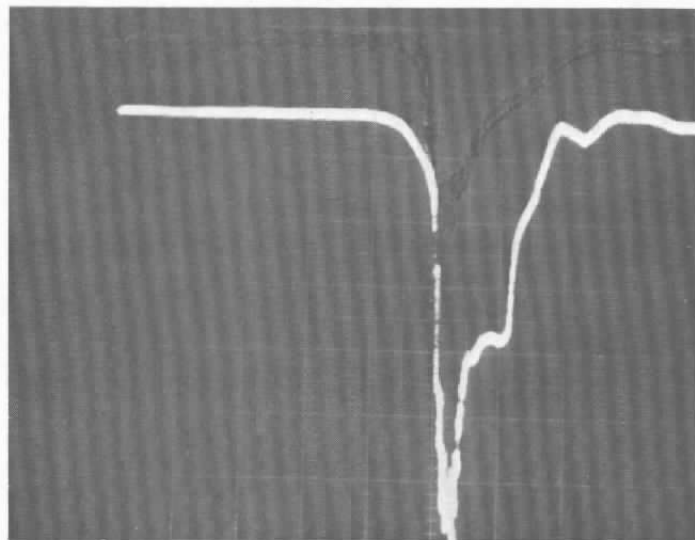


Figure 7. Faraday cup signal from millipound engine (long electrodes).

3.2 SPECIES PRODUCED BY THE ENGINE

Teflon is composed of a linear polymer chain of C_2F_4 molecules. Under vacuum pyrolysis it breaks down into 94 percent C_2F_4 , 2.6 percent C_3F_6 , 0.86 percent CF_4 , and 0.73 percent C_4F_8 . All of these are gases at standard atmospheric conditions. A plot of vapor pressure versus temperature is presented in Fig. 8. Under vacuum conditions in a typical space simulation chamber (10^{-5} torr) these gases could be expected to collect on liquid nitrogen-cooled surfaces with C_4F_8 condensing on surfaces at temperatures as high as $125^{\circ}K$.

A small sample of the Teflon fuel was mounted in a tungsten filament and evaporated in the test chamber. Figure 9 presents a mass spectrum produced by this vacuum pyrolysis. It should be noted that a further breakdown of the gases occurs as these species enter the ionization region of the mass spectrometer. Under the electron bombardment of the mass spectrometer the gases produce a characteristic cracking pattern. The contributions of the minor species can be ignored when compared to the signal levels from the C_2F_4 component. The observed cracking pattern agrees with that observed when gaseous C_2F_4 was bled into the test cell.

In addition to the gases produced by the pyrolysis of the Teflon, it was also noted that a slight coating of material had collected on the insulated supporting studs. Thus, a second evaporation experiment was conducted in which an ATR (Attenuated Total Reflectance)

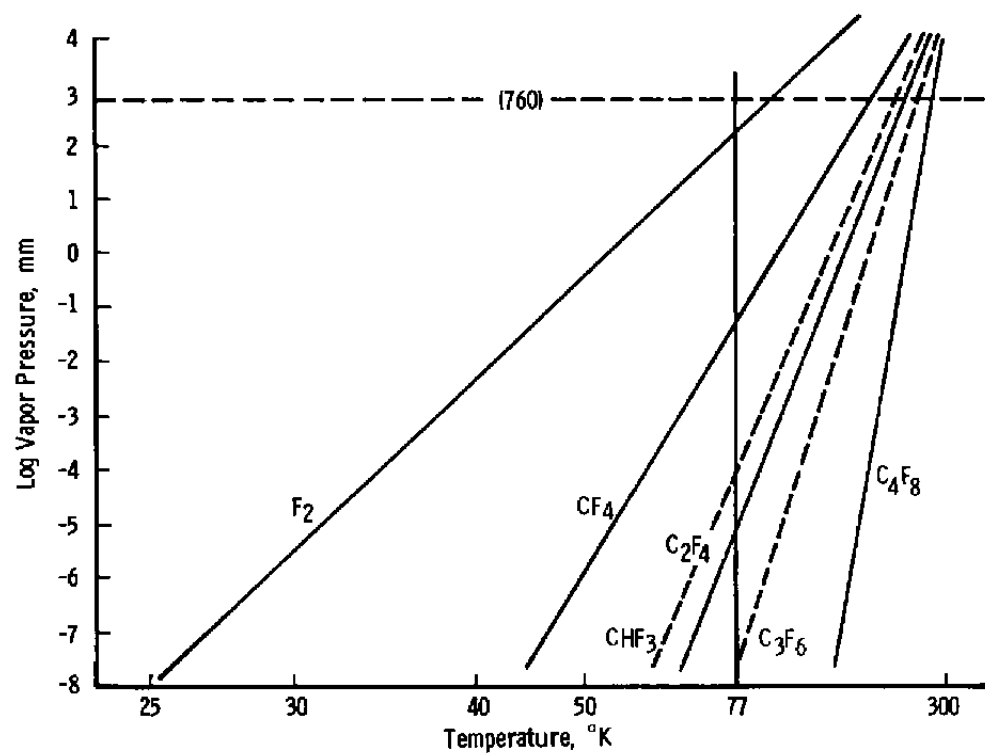


Figure 8. Vapor pressures of pyrolysis products.

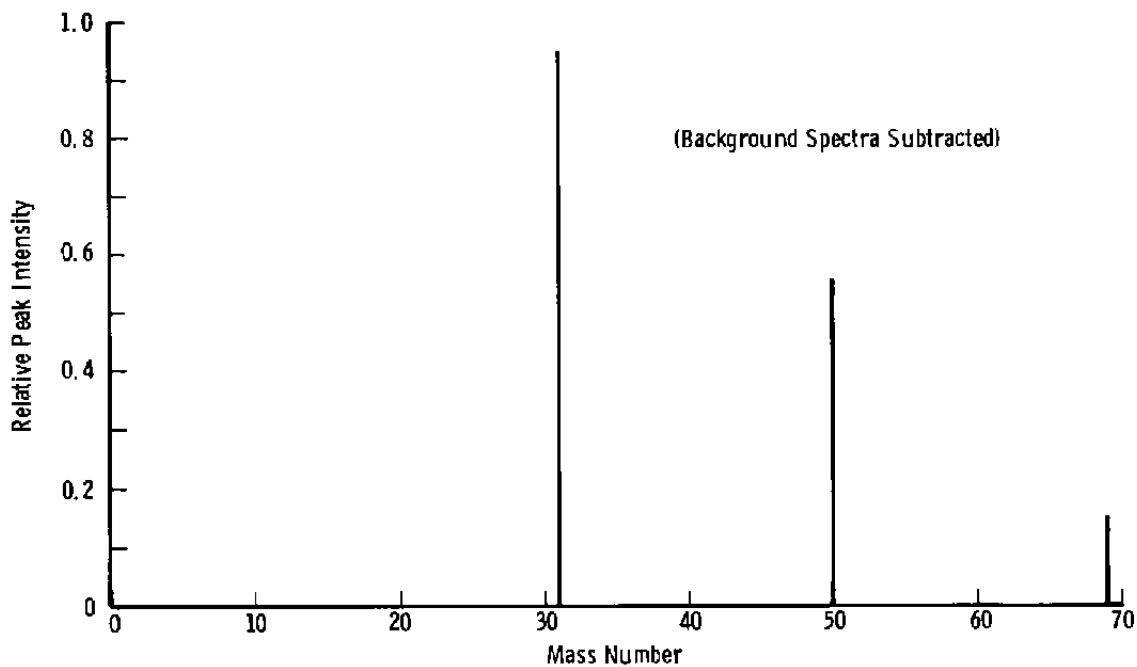


Figure 9. Mass spectra from vacuum pyrolysis of Teflon®

plate was located by the Teflon-loaded filament. The resulting coating on the ATR plate was analyzed using infrared absorption spectroscopy. These data show that under moderate pyrolysis rates significant numbers of the polymer chains in addition to the gaseous products are sputtered from the Teflon sample. These molecules collect on surfaces and retain the IR absorption characteristics of the original Teflon.

Further comments on material collected from the operation of the pulsed plasma engine are contained in Section 3.5.

3.2.1 Gas Species (Ion Gage)

Each engine pulse is followed by a rapid pressure rise in the vacuum chamber which then decays to a base pressure as the vacuum pumps remove the gases. A typical history of the total chamber pressure from multiple pulses of the millipound engine is presented in Fig. 10.

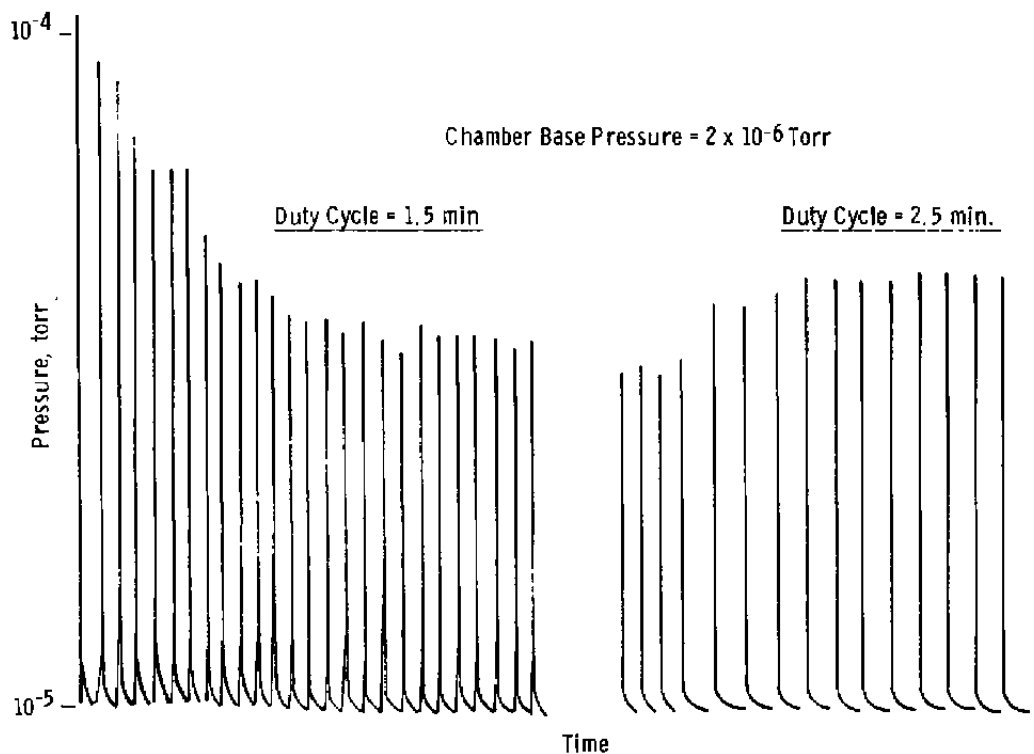


Figure 10. Vacuum chamber pressure history.

The sequence represents the startup of engine firings after an overnight shutdown of the engine; it continues through a period where the pressure pulses become quite repeatable and then shows the effect produced when the duty cycle is changed from firing every 1.5 minutes to every 2.5 minutes. The initial high pressure peaks can be explained as a general cleaning of

adsorbed gases from the vacuum chamber walls. After several pulses, these gases have been reduced to some equilibrium value. An unexpected pressure increase is observed when the duty cycle is reduced. It was thought that the additional time between firings would permit the vacuum pumps to reduce the chamber pressure to a little lower value and thus reduce the total pressure rise. The fact that the maximum pressure actually increases suggests that a significant part of the pressure rise is still due to gases being driven from chamber walls and that these gases are accumulating as adsorbed species during the entire period between engine firings. This indicates that the pumping process thus consists not only of the diffusion pumps but also the chamber surfaces recently cleaned by the plasma. The data presented in Fig. 10 are for the vacuum chamber surfaces at room temperature. The chamber base pressure is lower, but the pressure peaks are higher when the walls are cooled to cryogenic temperatures.

3.2.2 Gas Species (Mass Spectrometer)

Attempts were made to monitor the plasma pulse from the engine by skimming from the centerline of the plasma. These attempts were not successful for the following reasons. First the strong UV pulse from the engine saturated the electron multiplier of the mass spectrometer. Then the mass spectrometer was relocated with the multiplier shielded from the UV. A small orifice was aligned with the mass spectrometer ionization section to allow the gas species to enter. In this orientation the secondary electrons produced by the plasma impacting the UV shield again saturated the mass spectrometer electronics.

Rather than looking at the instantaneous plasma, the mass spectrometer was thus used to look at the gas species which accumulated in the vacuum chamber after an engine pulse. The results from the micropound engine were inconclusive. The pressure rise in the chamber was dominated by mass 28 with a gradual increase, after multiple shots, of background spectra associated with pump oils. There was a slight increase in mass numbers 19 and 20, which could be an indication of fluorine from the Teflon; however, no significant increase in masses 31, 51, 69, 81, or 100 was observed. Attempts to monitor individual mass peaks associated with C_2F_4 were not successful due to the low signal levels for each engine pulse; monitoring was also complicated by the erratic pulses produced by this engine.

The results from the millipound engine were more productive, though not conclusive. After repetitive pulses of the engine, mass peaks were observed to increase at $m = 12, 16, 19, 20, 28, 31, 50$, and 69. These include mass numbers associated with the species expected from Teflon. They compare well with the cracking pattern from the pyrolyzed Teflon but also include some additional mass numbers (Fig. 11). The 20 peak is significant and can be associated only with HF since the other possibilities, neon or argon, are not reasonable. The experiment was repeated with the walls cooled to 77°K.

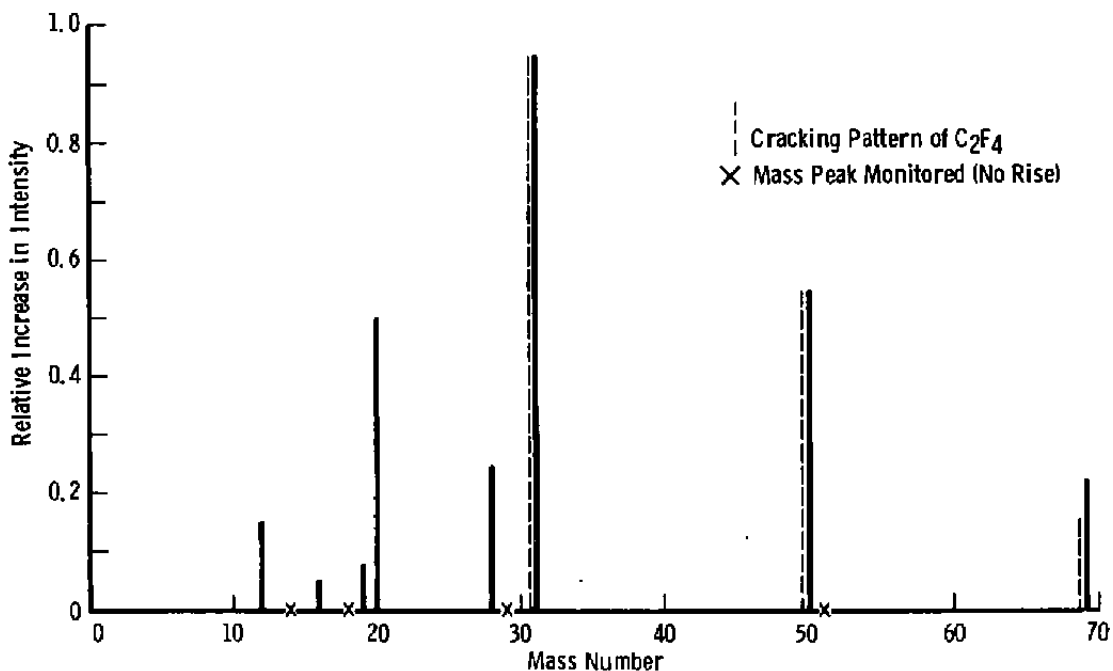
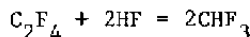


Figure 11. Mass spectra from engine pulses (300°K cryoliner).

With the LN₂ liner cold, the gas cracking pattern changes significantly and suggests a change in the gas species responsible for the pressure rise. The observed pattern is noted in Fig. 12. The ratio of the 69, 51, 50, and 31 peaks no longer matches the C₂F₄ from the warm chamber, but now matches that of a companion freon, CHF₃. In addition, with the cold liner, the m = 20 peak is now reduced significantly. This could indicate chemistry occurring on the cryopanels, and it is tempting to suggest that



The engine firings were repeated, and the mass spectrometer was tuned to a specific mass peak. The output was monitored on an oscilloscope and thus recorded the temporal history of the particular species. The data are presented in Figs. 13a and b. The following general observations are made:

- With the chamber liner at 300°K there is a significant pulse of HF gas in the chamber. This gas pressure decays much more rapidly than any other species, thus confirming a highly reactive gas (i.e., HF). When the liner is cooled to 77°K, there is no indication of a mass increase at M = 20.
- Coupled with this lack of HF when the liner is at 77°K are the two sets of data at mass 19 and mass 51. Each of these shows an initial contribution to the total

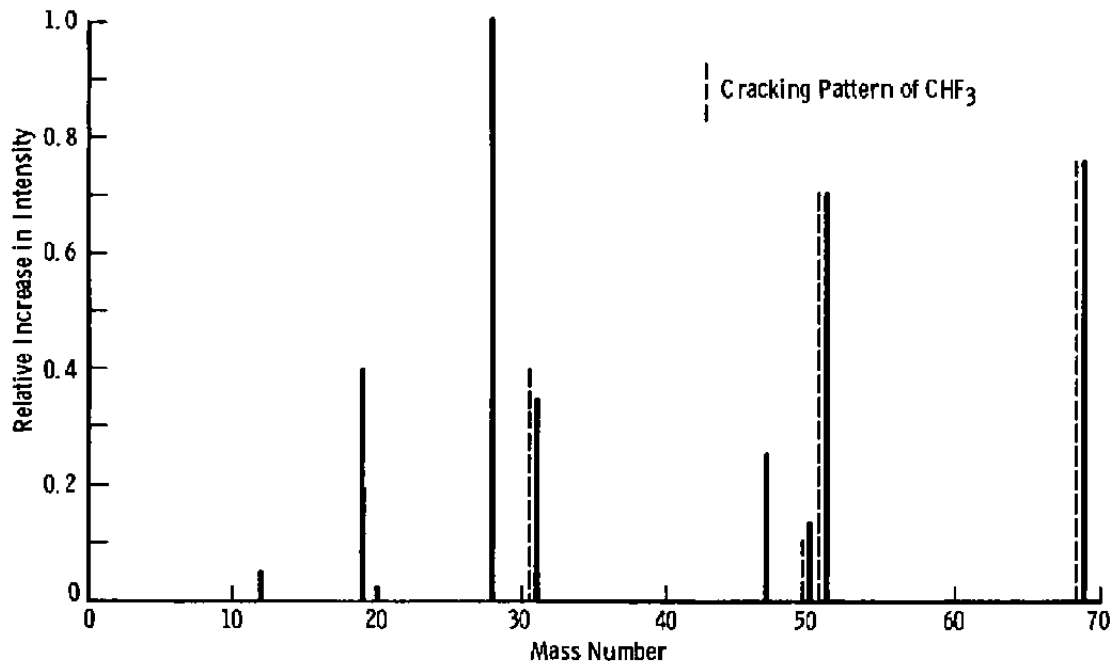


Figure 12. Mass spectra from engine pulses (77°K cryoliner).

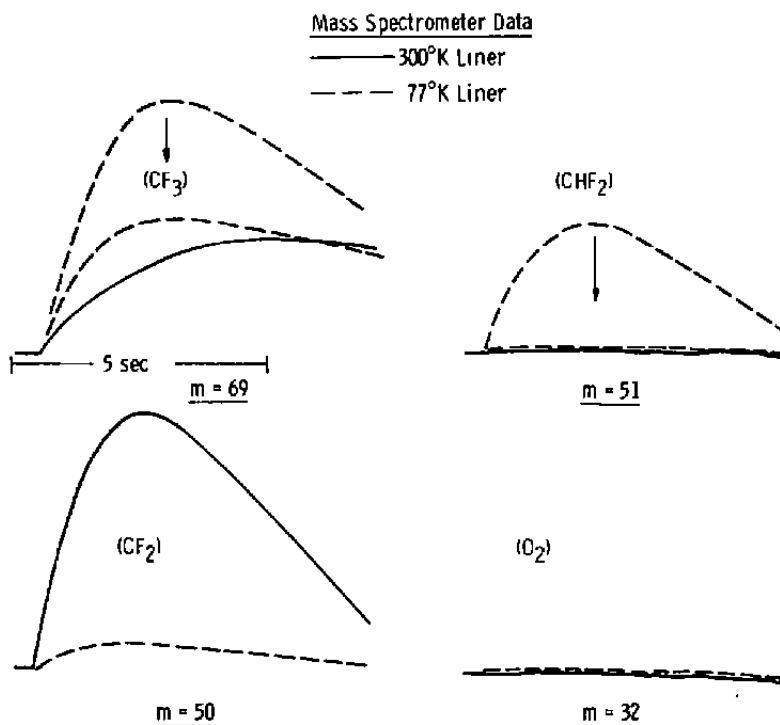


Figure 13. Mass spectrometer data: partial pressure profiles from a single engine pulse.

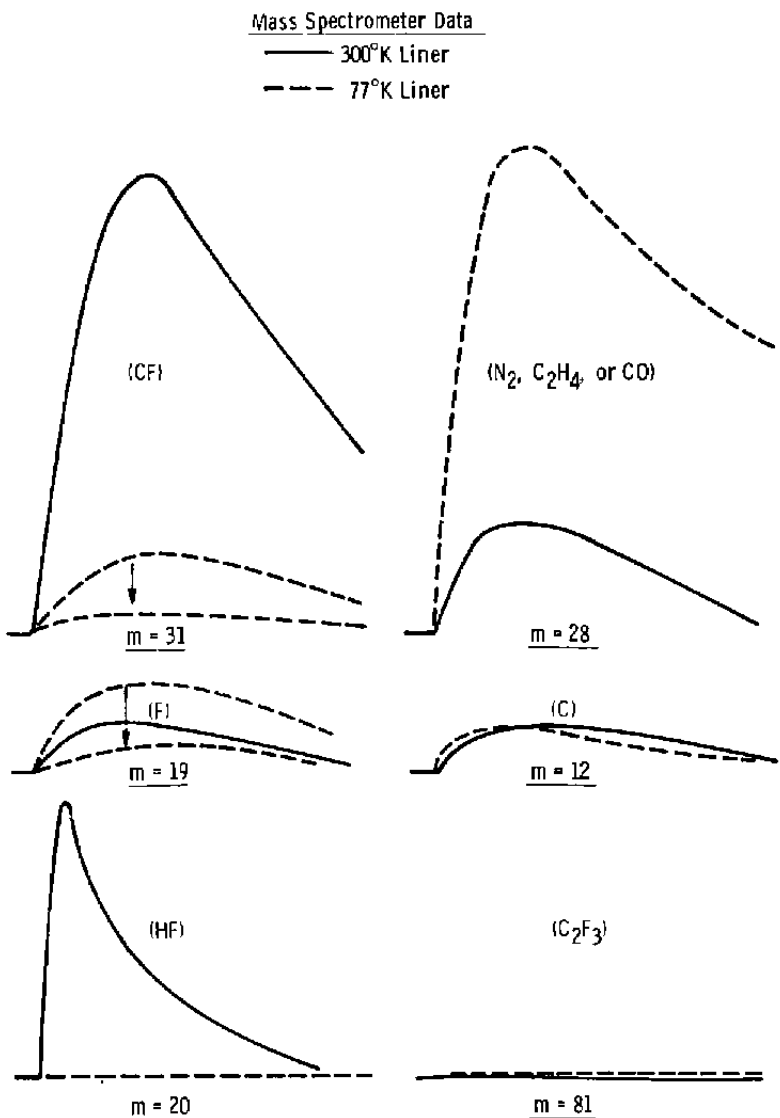


Figure 13. Concluded.

chamber pressure. However, with each subsequent engine firing, the intensity drops until after 10 to 20 shots there are no further pressure rises. This would indicate a surface reaction on the cold liner involving the HF and an accumulating layer of C_2F_4 . (Note the low levels of masses 31 and 50 with the 77°K liner; this is a result of C_2F_4 cryopumping.)

c. The mass 28 peak shows just the reverse trend. There is a larger increase in this gas partial pressure when the liner is cooled to 77°K. One explanation for these data is that this gas (N_2) is physically adsorbed on the walls of the chamber and is being sputtered by the plasma. This process can be considered mechanical and

thus unrelated to surface chemistry. The lack of a comparable rise in the 32 peak (O_2) suggests the source of the N_2 to be a slight leak in the LN_2 system rather than an air leak to the vacuum chamber.

These data do not present a complete picture of what is happening in the engine exhaust species/wall interactions, but they strongly confirm that there are chemical reactions occurring. These may be spontaneous reactions, or they may be driven by the energy supplied in the strong vacuum ultraviolet (VUV) photon pulse from each engine firing. Further experiments are planned with the mass spectrometer to better define the problem. It is apparent at this point, however, that in a baffle system the surfaces exposed to the first plume encounter should be at least at room temperature, and it may even be preferable to operate them hot to avoid any condensation and accumulation of material leading to surface reactions.

3.2.3 Gas Species (UV Radiation Measurements)

3.2.3.1 Micropound Engine

A small spectrometer was used to determine the feasibility of using the UV-visible spectra from each engine pulse as a diagnostic tool. Figure 14 presents a plan view of the instrumentation used for this study.

An f/3, 0.2-m spectrometer with a concave, holographic grating of 175 lines/mm had a resolution of about 20 Å when fitted with a 50- μm entrance slit width. The spectrometer was mounted in a case which could be purged for removal of ultraviolet-absorbing oxygen molecules. The detector was an intensified linear photodiode array having 512 elements and sensitive to light from 1700- to 8000-Å wavelengths. Detector signals were processed and displayed by means of a multichannel analyzer. A quartz lens of approximately 75-mm focal length was adjusted to focus light of 4300-Å wavelength upon the entrance slit. The source was at a distance of 0.79 m from the quartz window of the case. A calcium fluoride (CaF_2) window of 63-mm clear diameter was installed on the test chamber, and a purge tube was affixed between chamber and case windows as shown. A small light source was placed at the plasma engine face and the spectrometer was adjusted until the image of the source was centered on the entrance slit.

One engine pulse was sufficient to obtain the maximum allowable signal on one of the diode elements at less than maximum gain setting. In addition, the entire spectrum was recorded during each pulse. A representative spectrum is shown in Fig. 15. The pulses were essentially equivalent in spectral appearance but were of variable intensity. Background

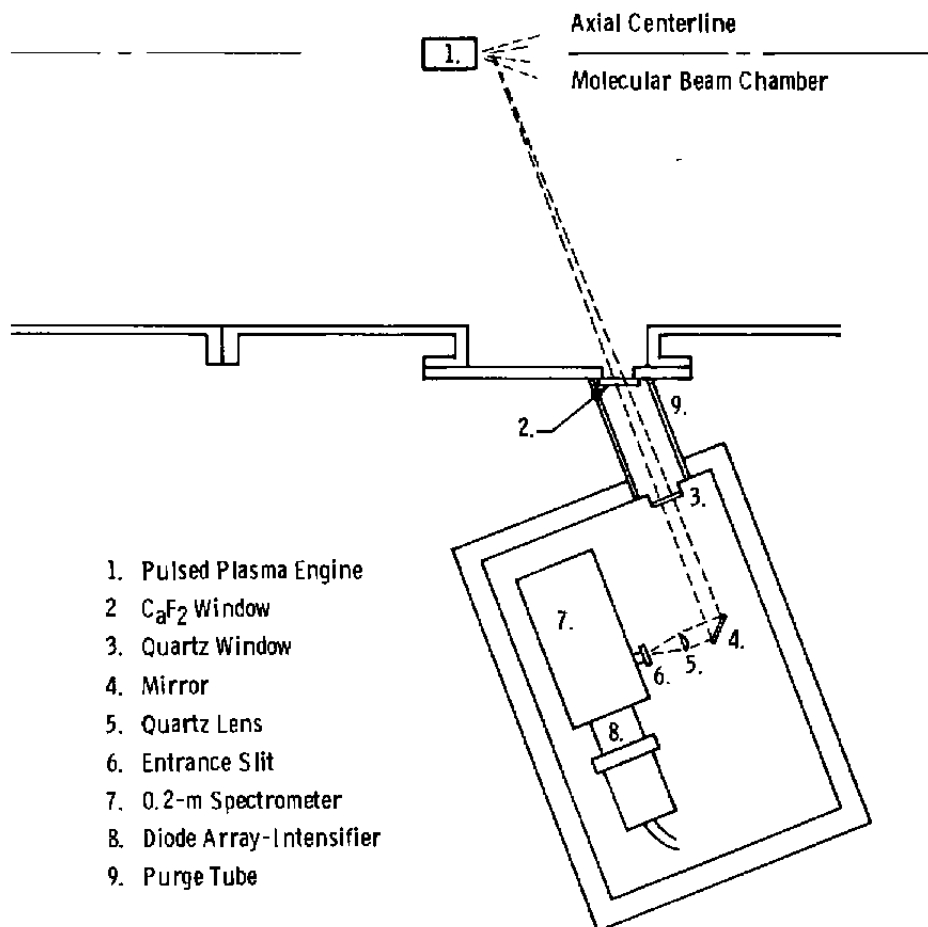


Figure 14. Plan view of optics for UV spectrometer (typical).

signals were obtained by gating the detector an equal time during no-pulse conditions, and these signals were subtracted from the plume signals by means of the multichannel analyzer. A wavelength calibration was obtained by exposure of the spectrometer to light from an Hg lamp; this spectrum is shown in Fig. 16. Identifiable wavelengths are plotted as a function of diode element number in Fig. 17. After a preliminary analysis of the plasma spectrum was made, the four calibration points past 5780 Å were added to the curve in lieu of a linear extrapolation.

Table 1 presents an analysis of the spectra of Fig. 15. Identifications were made with the information contained in Ref. 3. No molecular band systems could be identified; all spectral features appear to be atomic and ionic transitions in singlet or group form. Positive identification of ionized carbon (C^+ , C^{++} , and C^{+++}), atomic hydrogen (H), and ionized fluorine (F^+) were made, while neutral fluorine (F) was less certain. Except for the 7620-Å transition, the unidentified spectra are weak.

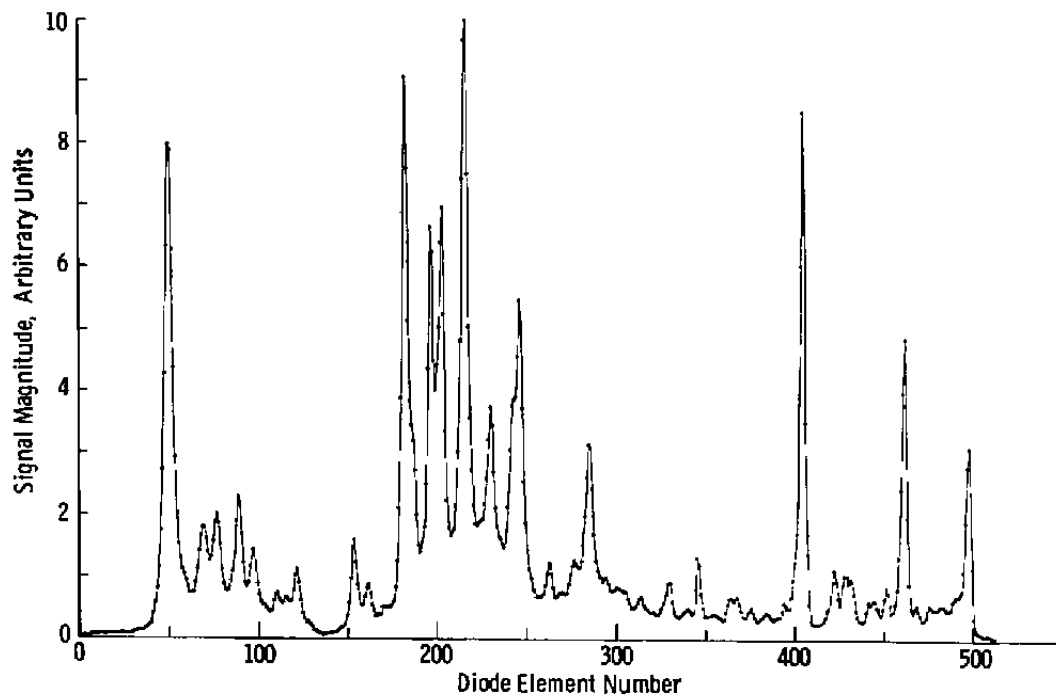


Figure 15. Representative spectra (micropound engine).

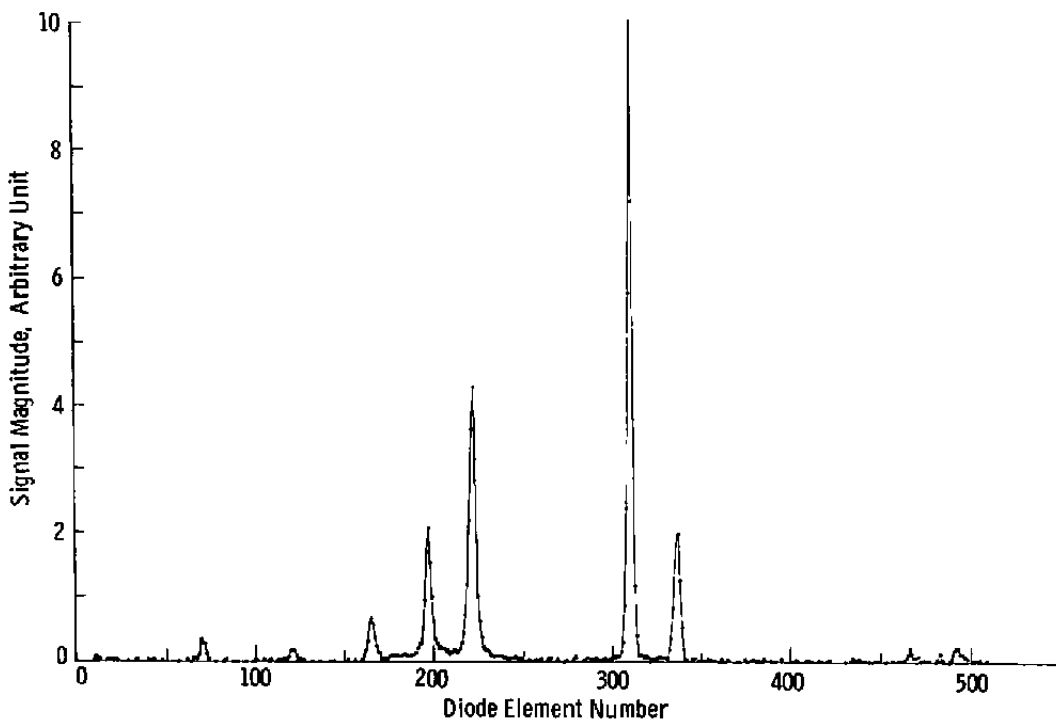


Figure 16. Mercury lamp spectrum for wavelength calibration (micropound engine).

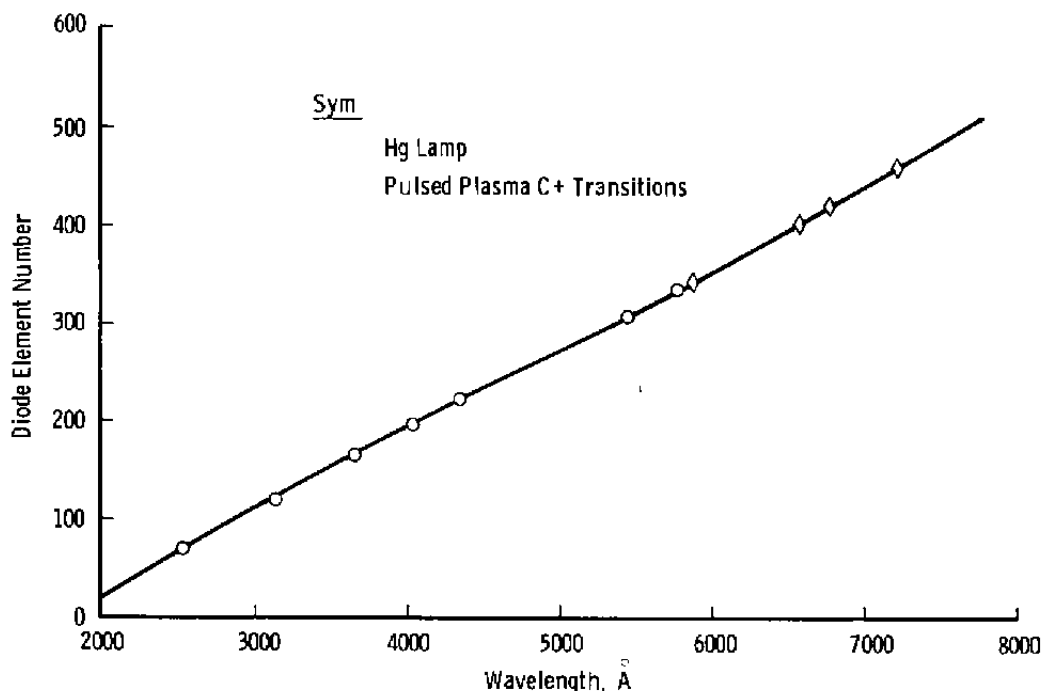


Figure 17. Wavelength calibration (micropound engine).

Table 1. Species Identification for Micropound Engine Plasma

Calibration Wavelength, Å	Species Identification	Calibration Wavelength, Å	Species Identification
2300	S 2297 C ⁺⁺	5510	?
2525	S 2524 C ⁺⁺⁺	5710	S 5696 C ⁺⁺ ?
2610	?	5890	T 5890 C ⁺
2750	T 2747 C ⁺	6100	?
2845	D 2837 C ⁺ ?	6150	?
3000	S 2993 C ⁺	6250	S 6240 F
3130	M 3124 F ⁺⁺ ?, M 3151 F ⁺⁺ ?, M 3177 F ⁺⁺ ?	6350	S 6349 F
3510	M 3504 F ⁺	6460	?
3610	M 3609 C ⁺⁺	6580	D 6580 C ⁺ , 6563 H (ALPHA)
3850	T 3849 F ⁺	6786	M 6786 C ⁺ , S 6774 F
4030	T 4025 F ⁺	6845	S 6834 F, S 6856 F
4115	S 4122 C ⁺⁺ , M 4103 F ⁺ , M 4114 F ⁺	6895	S 6870 F, S 6902 F, S 6910 F
4270	T 4267 C ⁺ , S 4246 F ⁺ , S 4299 F ⁺	7010	?
4450	S 4447 F ⁺	7050	S 7037 F
4650	T 4649 C ⁺⁺ , M 4663 C ⁺⁺ , S 4647 C ⁺⁺⁺	7120	S 7128 F
4860	4861 H (BETA)	7234	T 7234 C ⁺
5140	M 5142 C ⁺	7620	?

S = Singlet D = Doublet T = Triplet M = Multiplet

3.2.3.2 Millipound Engine

The need for increased spectral resolution of the pulsed plasma emitted radiation was evident in the micropound engine study, even though the principal features were positively identified. Therefore, for the determination of the millipound engine spectral radiation, a higher resolution spectrometer was selected.

An F/8, 1.0-m, Czerny-Turner spectrometer having an 1180-groove/mm grating blazed at 4500 Å was positioned at a 45-deg angle relative to the axial centerline of the chamber. An adapter was built that allowed the same photodiode array intensifier-detector used in the micropound engine study to be positioned at the photographic image plane of the spectrometer. The detector's optimum vertical position and focus were achieved by means of the existing vertical racking mechanism and translation of the internal movable mirror, respectively. The final resolution was significantly less than that obtained at the exit slit during spectrometer alignment, and degradation of the focused light by scattering at the intensifier's scintillation faceplate is suspected. A quartz lens of approximately 75-mm focal length was installed in the purge tube and adjusted to focus nozzle exit plane light upon the entrance slit.

An Hg-Ar lamp was used for wavelength calibration. Spectral lines of known wavelength, λ_{true} , were displayed on the multichannel analyzer, and the spectrometer dial wavelength, λ_{dial} , was changed until each line appeared in the middle of the screen at channel number 256. The result of the calibration procedure is shown in Fig. 18. Upon recording a spectrum, it is necessary to know the reciprocal dispersion (Å/channel) in order to calculate the wavelength of a spectral line. To measure this, two lines of known wavelength were centered about channel number 256, and the difference in channels was recorded. This was repeated over the entire wavelength range, and the result is shown in Fig. 19. Using channel number 256 as the reference, one can thus determine the wavelength of any unknown spectral feature.

Polaroid film was also used to record the Hg-Ar lamp spectrum, and reciprocal dispersion values (Å/mm) were measured from the film with a measuring magnifier. These values are more accurate than those from the multichannel analyzer and are plotted in Fig. 19. The curve through the scattered intensifier-detector values was determined by assuming it to be proportional to the film values. Ratios of the intensifier and film values were calculated at seven wavelengths, and the average ratio was 0.0511 ± 0.0009 mm/channel or 19.57 ± 0.34 channels/mm. This value was then used to determine the intensifier-detector curve from the film curve.

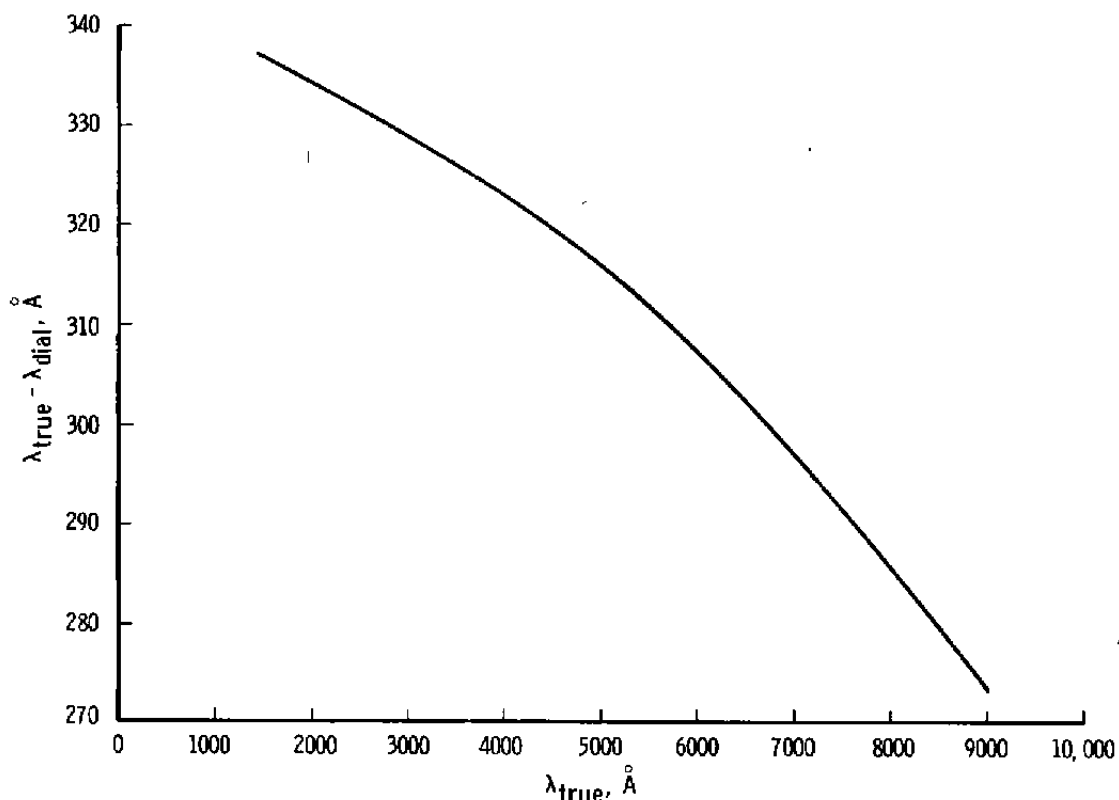


Figure 18. Correction terms for wavelength calibration.

Pulsed plasma spectra were recorded as described previously except for the necessity of stepping the spectrometer in wavelength between pulses. Steps of 150 Å and approximately 450 Å were taken for intensifier-detector and film outputs, respectively. The intensifier gain control was adjusted as needed. Selected intensifier-detector spectra are presented in Fig. 20, and spectra obtained on TRI-X cut film are presented in Fig. 21; species identifications and wavelengths are included. The only molecular spectra identified were those of the C₂ Swan system's (0,0) and (1,0), (2,1), (3,2), and (4,3) bands in the green and blue. Transitions of C, C⁺, C⁺⁺, F, F⁺, H, Al, Mg⁺, Pb and Pb⁺ were identified (Refs. 3 and 4), while indications of F⁺⁺ and CF₂ appear in the spectra. The last three metallic elements are ingredients in the Mykroy material used in the engine (Fig. 22). About twenty percent of all lines are not identified; however, these are all of low intensity. The particular intensifier-detector spectra presented in Fig. 20 show examples of the various species' spectral lines.

In addition to species identification, the relative intensities of spectral lines are functions of the excitation temperature and of the relative species number densities, and estimates of these quantities are useful descriptors of the plasma state. For each atomic element, there is a temperature at which the intensities of emission lines belonging to a particular ionization

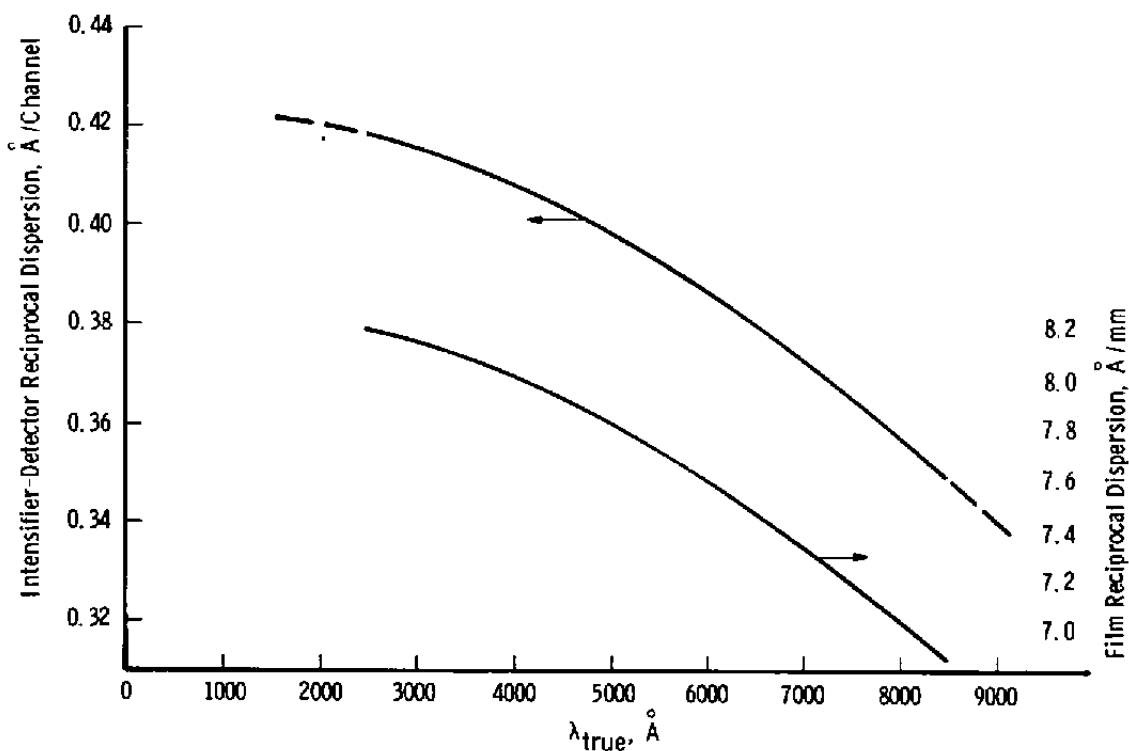
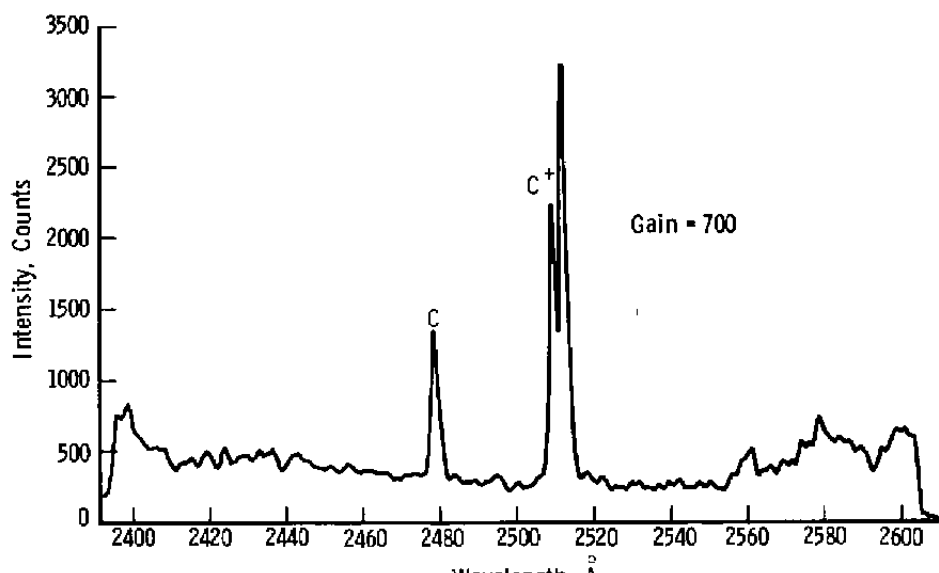


Figure 19. Calibration curves.

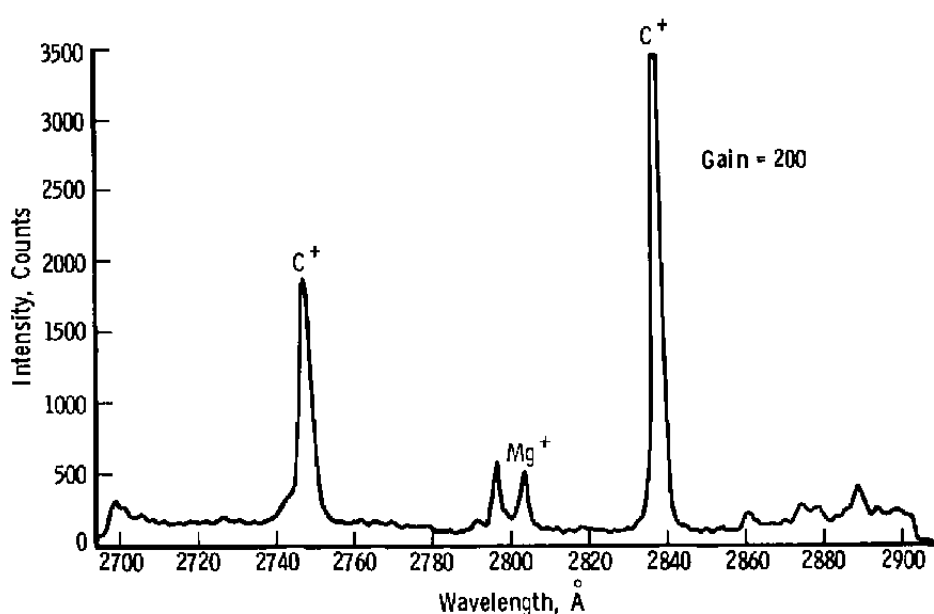
state maximize. These temperatures are tabulated in Ref. 5 for the carbon ionization sequence, and upon a visual inspection of the pulsed plasma spectrum one is led to a temperature estimate of 2 to 3×10^4 °K. The intensity ratios of the spectral lines C⁺ 2297 Å and C⁺ 2509 to 2512 Å are plotted as a function of temperature for various electron densities in Ref. 6, and the aforementioned temperature range is confirmed upon calculating the intensity ratio of those lines. In equation form, the excitation temperature for two lines of the same species and ionization state is (Ref. 5)

$$T = \frac{E_2 - E_1}{k \ln \left(\frac{I_1 A_2 g_2 \lambda_1}{I_2 A_1 g_1 \lambda_2} \right)} \quad (1)$$

where E and g are the upper state energy and statistical weight, respectively, k is the Boltzmann's constant, and I, A, and λ are the intensity, spontaneous emission transition probability, and wavelength of the transition. The two transitions are denoted by subscripts 1 and 2. In spite of low-accuracy transition probability values and line intensity measurements, the temperature calculated from Eq. (1) using the two close-lying F⁺ lines at 4246 and 4299 Å and line values from Ref. 3 was 7.5×10^4 °K, and agreement with the carbon observations is deemed reasonable.



a. 2500-Å region



b. 2800-Å region

Figure 20. Intensifier spectra.

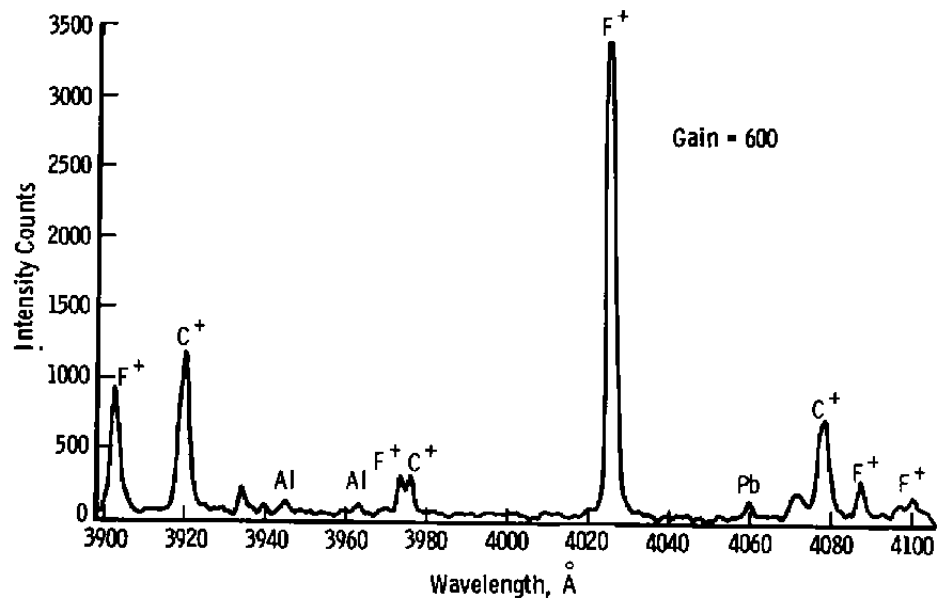
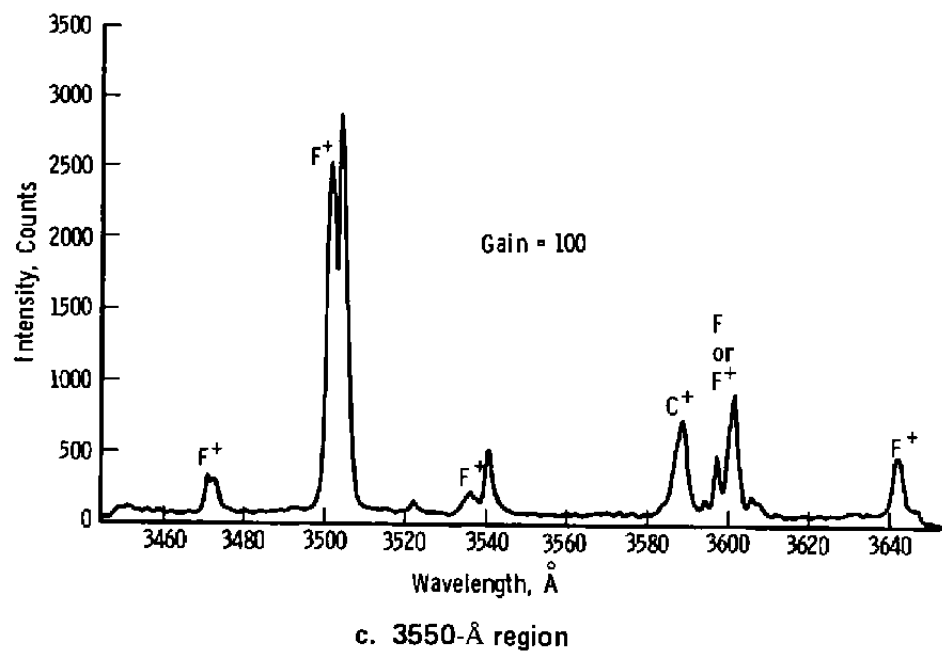
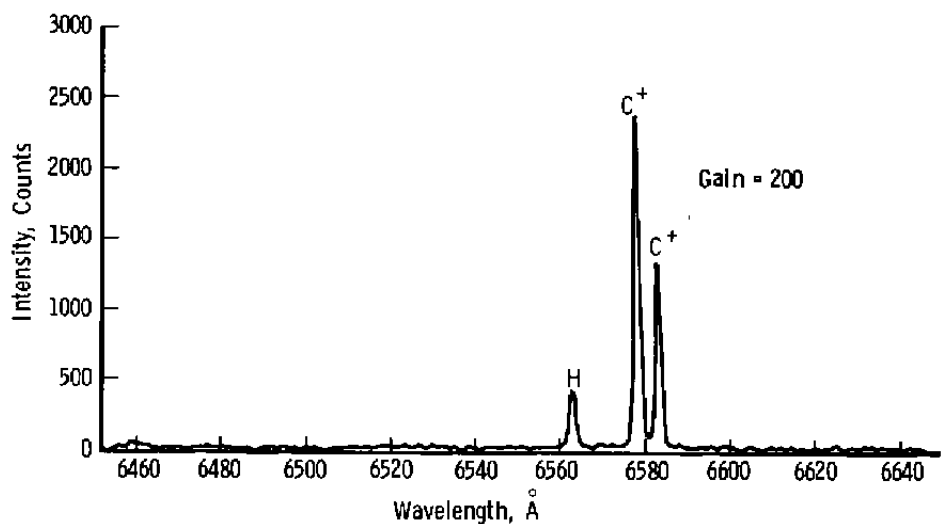
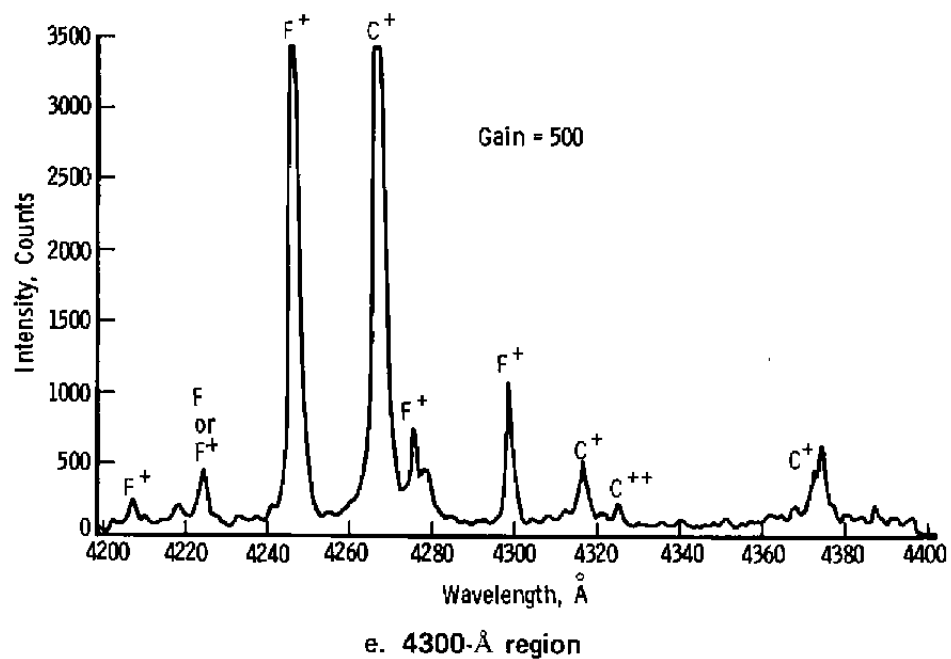
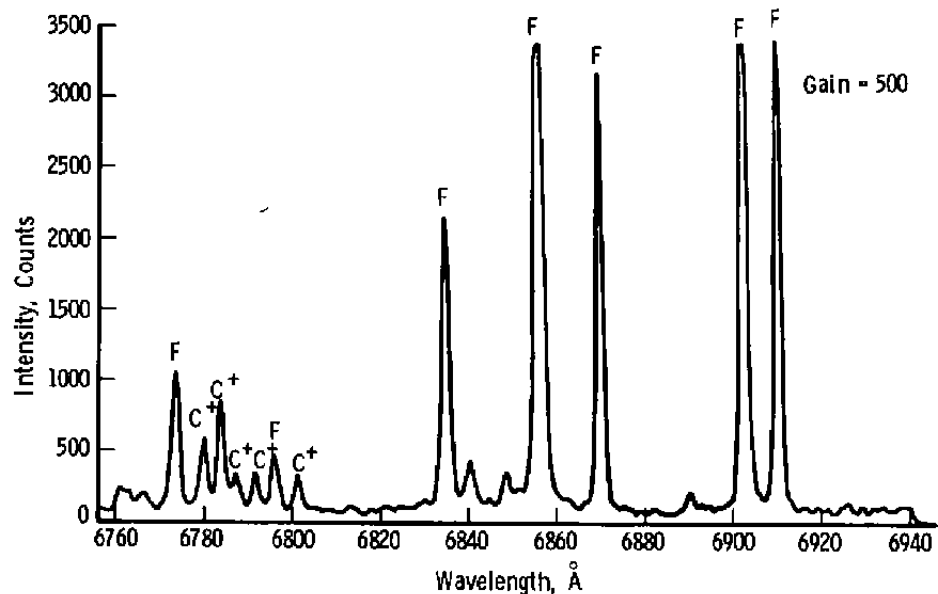


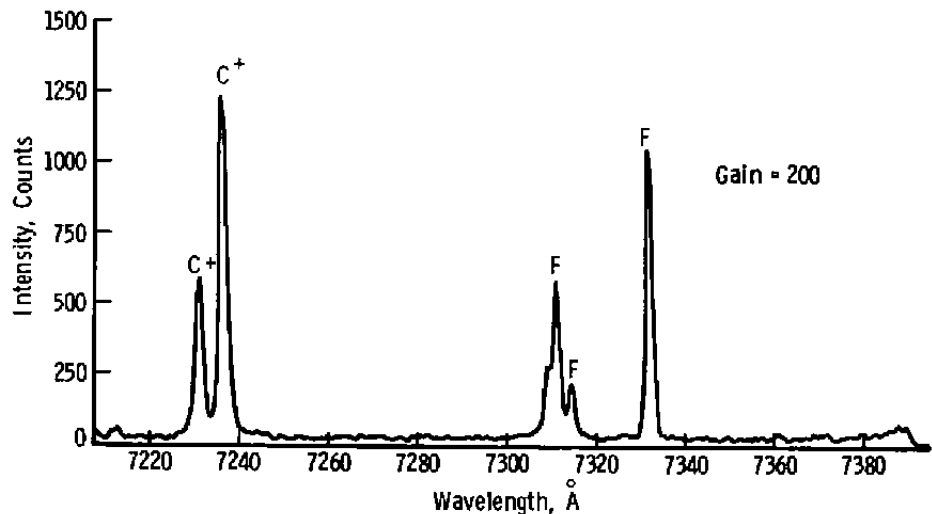
Figure 20. Continued.



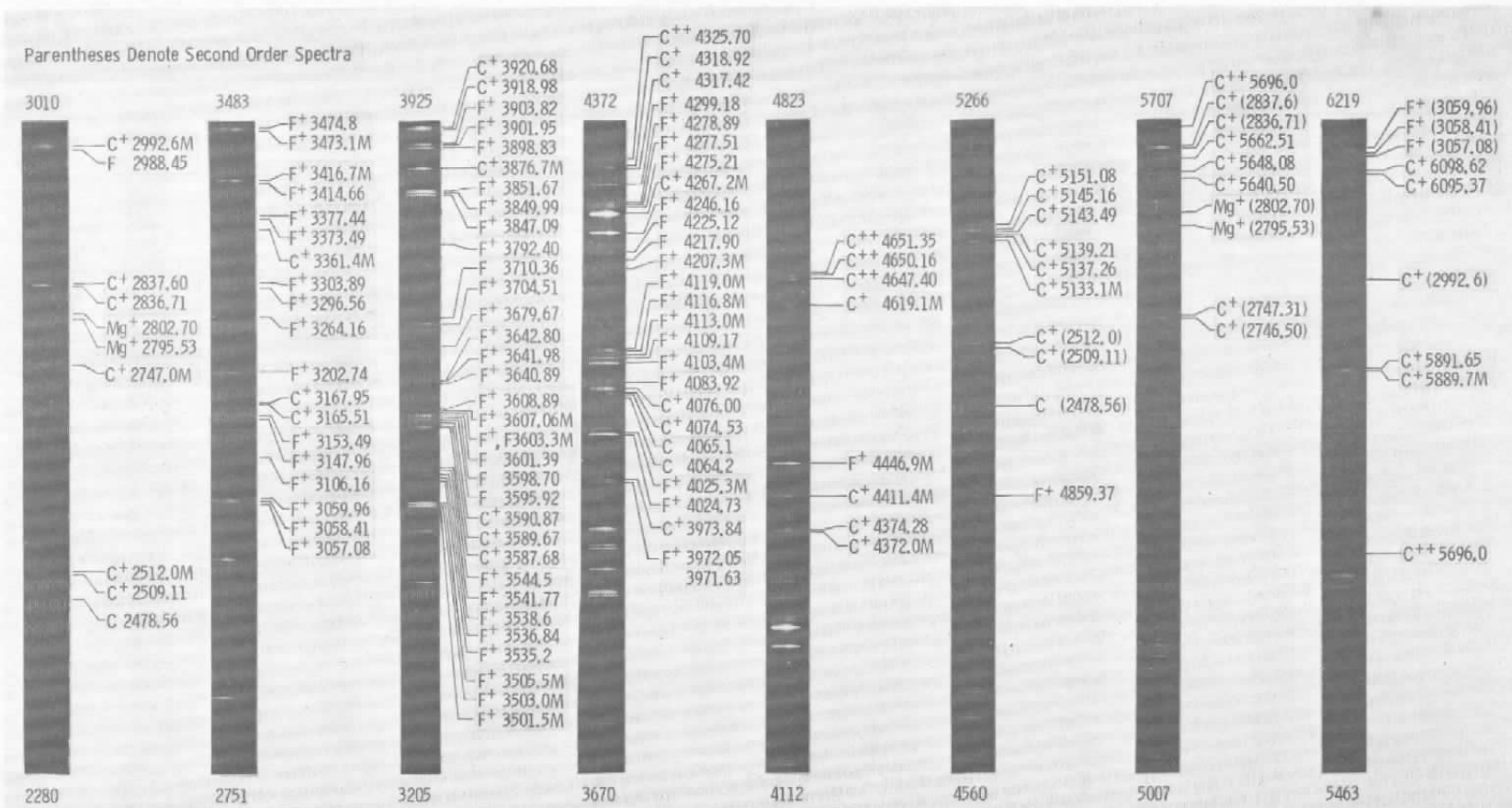
f. 6550-Å region
Figure 20. Continued.



g. 6850-Å region

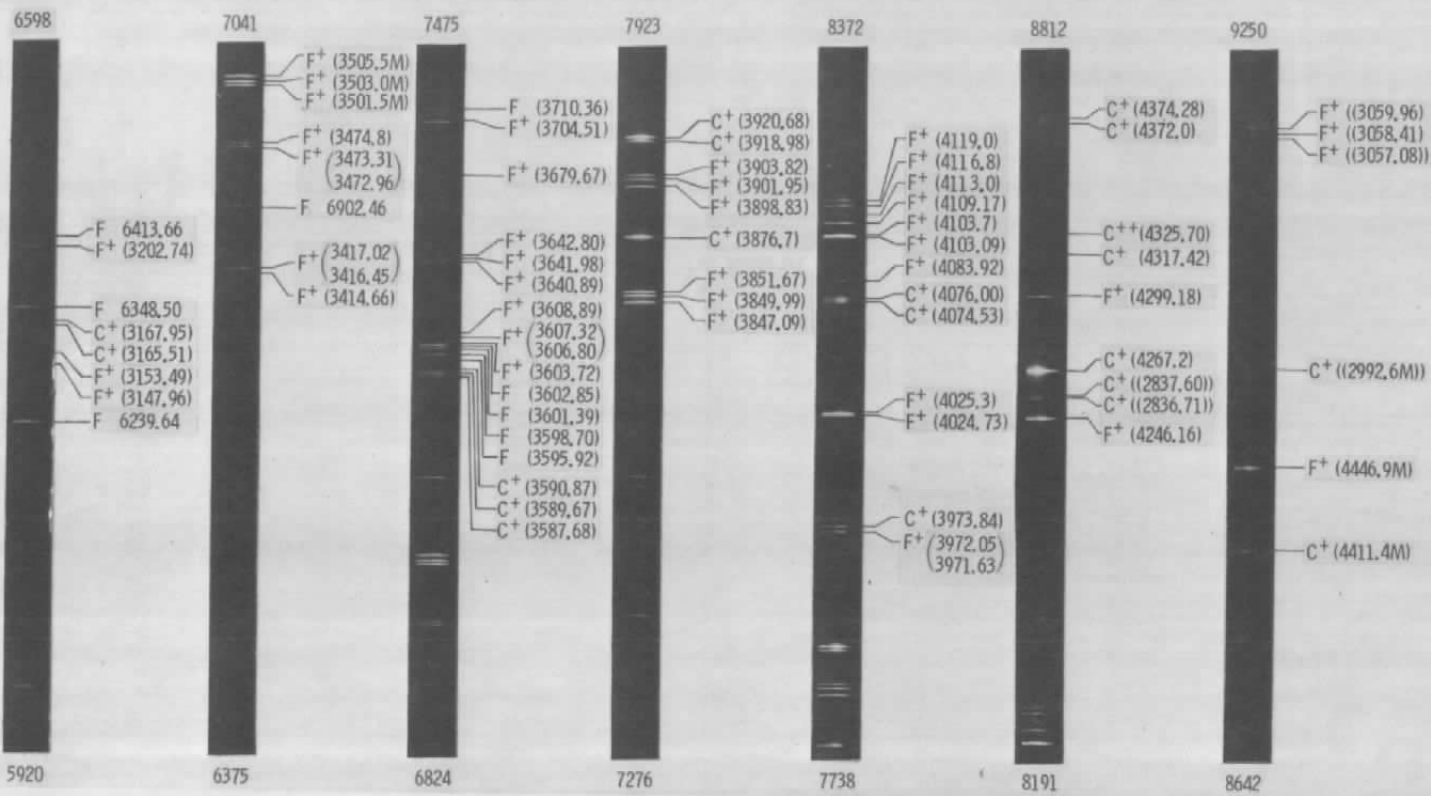


h. 7300-Å region
Figure 20. Concluded.



a. Low wavelength region (λ), Å
 Figure 21. UV spectra on Tri-X film

(Parentheses Denote Second Order Spectra)



b. High wavelength region (λ), Å
Figure 21. Concluded.

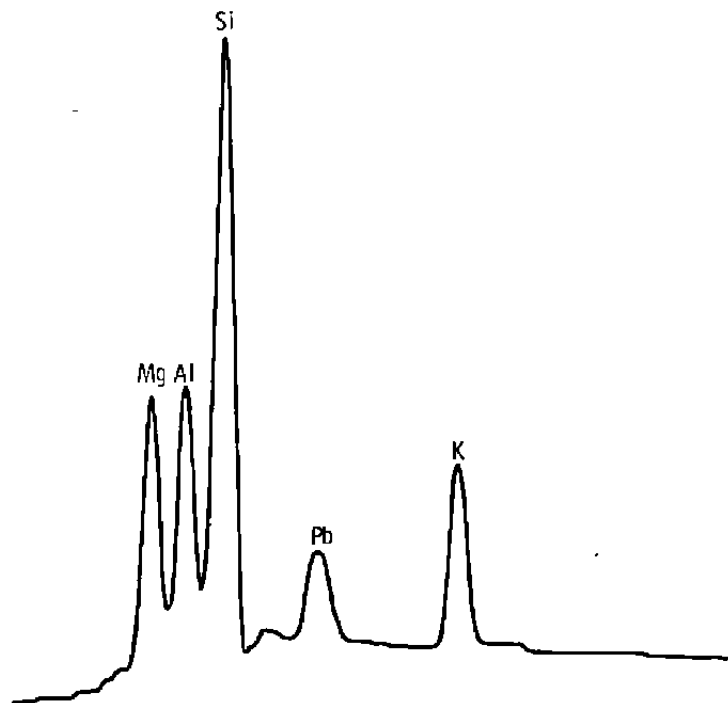


Figure 22. Ceramic insulator in engine (Mykroy material).

A number of estimates of relative number densities between various species and levels of ionization were made using intensifier-detector relative intensity ratios, assumption of a temperature of 3×10^4 K, and approximations to equations found in Ref. 5. The following trends resulted:

1. The higher the carbon or fluorine ionization state, the rarer the ion.
2. The carbon-fluorine number density ratio is approximately one.
3. The number densities of carbon and fluorine are an order of magnitude larger than the metallic species.

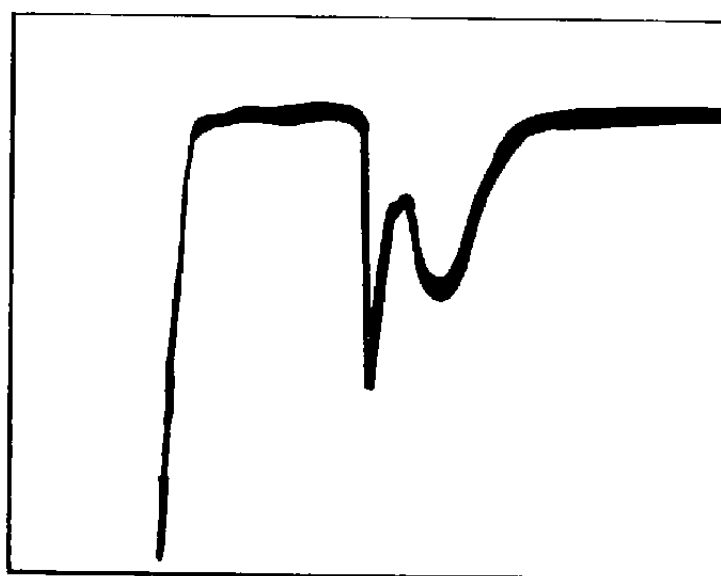
No estimate for the relative number density of C_2 was made; the peak height of the (0,0) bandhead at 5165 Å was about one-tenth of that of the strongest spectral line.

The intensity of the observed UV emissions is sufficiently strong to consider monitoring the temporal history of specific lines. This could possibly yield information on the production of multiply ionized species during the sequence of the oscillatory discharge of the engine capacitors. In addition, there is sufficient indication from theoretical predictions (Ref. 7) to suggest that by far the most intense emissions lie in the vacuum ultraviolet (VUV). Further studies will include a VUV spectrometer close coupled to the vacuum chamber.

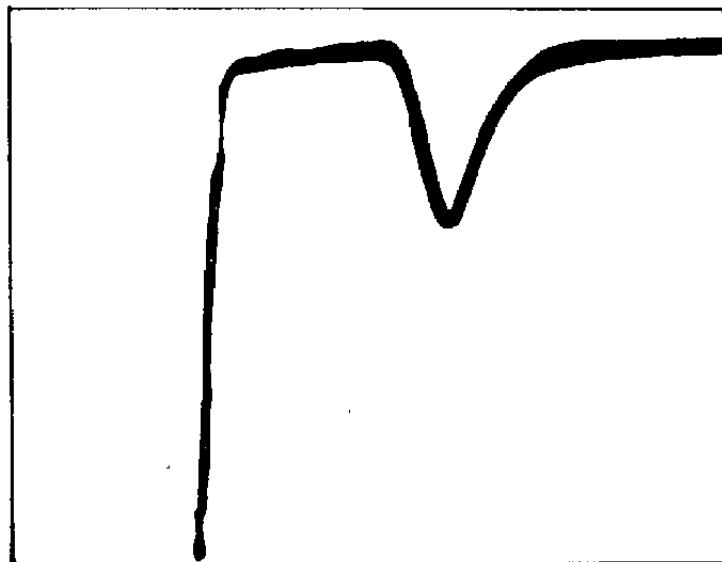
3.2.4 Plasma Ion/Neutral Composition

The question of ion/neutral concentrations in the plasma has not yet been answered. Measurements have been attempted using Faraday cups, Rogowski coils, and electron multipliers as detectors and electrostatic deflection plates as a discriminator. Signals from the micropound engine were too weak and too erratic to be useful. Experiments with the millipound engine consisted of using a pair of skimmers to collimate a beam of particles from the centerline of the plasma. This beam was passed between two parallel deflection plates and then traveled to the detector. The first data were taken using an electron multiplier as a detector. A typical signal is shown in Fig. 23a. The leading spike is identified as positive ions since application of a suitable voltage (20 to 40v) on the parallel plates could deflect it from the detector (Fig. 23b). The remaining signal could be interpreted as neutral molecules with sufficiently high energy to produce an electron shower in the multiplier.

The experiment was repeated using a Faraday cup as the detector. The results were a little different in that the positive ion spike was somewhat suppressed due to a negative precursor, and the "neutral" component was also structured with negative signals. This difference can be explained by considering the fact that the electron multiplier has a strong negatively biased dynode as the impact detector. Thus, any negative electron signals would be effectively filtered. The timing of these electrons, however, is such that they cannot have been emitted from the engine along with the positive ions since they arrive at the detector too late.



a. Electron multiplier signal (0-v deflection)
Figure 23. Electron multiplier signal.



b. Electron multiplier signal (40-v deflection)
Figure 23. Concluded.

Subsequent experiments in which a Rogowski coil was used as a search coil to determine the conditions in the vacuum chamber during a plasma pulse have shown that there are serious questions as to the simple interpretation of the electron multiplier data. With the coil in the engine section of the vacuum chamber and located in the primary plasma beam, it was found that when the engine discharges there is an intense electron shower which is induced by the VUV photons interacting with chamber walls. In addition, there are secondary showers as the plasma bounces from the walls. These electrons are reflected into the plasma and thus could distort the ion/neutral composition. Further evidence that this could indeed be the case was obtained when the two skimmers were replaced with a second pair which had much larger orifices. The general nature of the positive spike followed by a neutral signal was retained; however, the relative intensities of the signals indicated many more ions than neutrals. Also, with the larger beam it was noted that when a deflection voltage was applied to the plates there was a discharge between the plates when the engine fired.

It has also been observed that positive carbon and fluorine ions can survive at least one wall collision and retain their identity as ions. In this experiment the mass spectrometer was installed in the second section of the test chamber and was located off centerline (see Fig. 24). A flat plate was installed to intercept the core skimmed from the plasma pulse. The mass spectrometer was tuned to mass 12, and the output was coupled to a fast scan memory scope. The mass 12 peak output was thus monitored from the initiation of the engine pulse for a period of approximately 100 μ sec. It was noted that the mass spectrometer sees a mass 12 pulse which could correspond to an ion striking the rear wall and traveling back to the

spectrometer. Two interesting observations were made. The first was that this signal increased significantly when the ionization section of the mass spectrometer was turned off. This is interpreted to suggest that the carbon arrives as a positive ion and that any electron field in the mass spectrometer entrance neutralizes and thus eliminates ions which would otherwise be drawn into the mass filter. The second was that the mass spectrometer could be tuned over a much broader range before eliminating the mass 12 peak. This indicates that the ion energy is not so well defined as when the molecule enters the head with thermal velocity, is ionized, and then is extracted through a predetermined electric field. Pre-ionized atoms entering the extractor field with a significant energy spread would thus detune the mass selection. A similar result was noted when the system was tuned to mass 19.

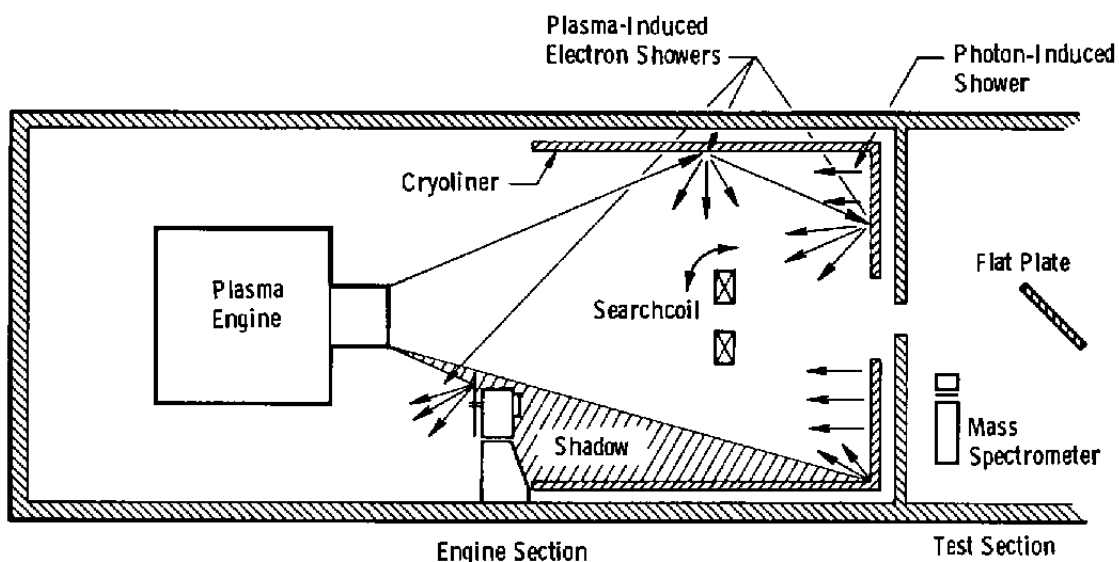


Figure 24. Engine installation.

These experiments have confirmed the need to install a sample baffle system in the Aerodynamic Molecular Beam chamber. Further work on examining the plasma for the neutral/ion concentration will be conducted along with an evaluation of the effectiveness of a baffle to shield the backflow region from secondary reflections of ions and electrons.

3.3 ENERGY ACCOMMODATION COEFFICIENT

Small calorimeters were built and used to measure the energy transfer from the plasma to engineering surfaces. Materials used for the calorimeters were typical of those used in the vacuum chambers and included copper, aluminum, and brass. A schematic of one of the calorimeters is presented in Fig. 25. The flat plate was oriented on the centerline of the engine and could be rotated from normal to parallel to the plasma flow. In addition the

engine could be rotated about the nozzle exit plane so that the calorimeter could also be used to map the plume profile.

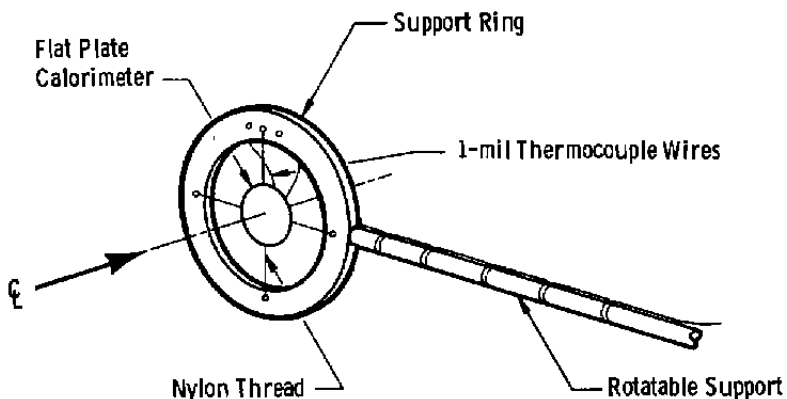


Figure 25. Flat plate calorimeter.

The first experiment was conducted to determine whether the energy transfer was a strong function of angle of incidence. The data consisted of calorimeter temperature rise for engine shots with the calorimeter positioned on centerline and oriented at various angles of incidence. Multiple shots were made at each angle to allow for variability in successive engine pulses.

Since the flat face of the calorimeter is completely immersed in the plasma, then if the energy transfer is independent of the angle of incidence of the plasma, the temperature rise should be a direct function of the cosine of the angle of incidence. The data presented in Fig. 26 indicate that within the accuracy as determined by the repeatability of engine pulses, this is the case. The solid line is a true cosine dependence. The bars presented on the plot indicate the range of temperatures recorded for each angle of incidence.

The energy accommodation experiment was conducted with conical calorimeters as shown in Fig. 27. They were mounted in the same location as the flat plate calorimeters and could be rotated so that the plasma impinged on the outer surface as the apex faced the engine or on the inner surface as the open base faced the engine. Three calorimeters were built with cone angles of 60, 45, and 30 deg, respectively. With the apex of the cone facing the plasma, each molecule will have only one collision with the calorimeter surface, whereas, with the open base facing the plasma, molecules will have multiple collisions before exiting. The number of collisions will be influenced by the included angle of the cone. Since in each case the mass of the calorimeter and the thermocouple detector is the same regardless of the orientation of the cone, the ratio of the temperature rises in the two orientations can be used to assess the value of the energy accommodation coefficient. The GUMRAP program

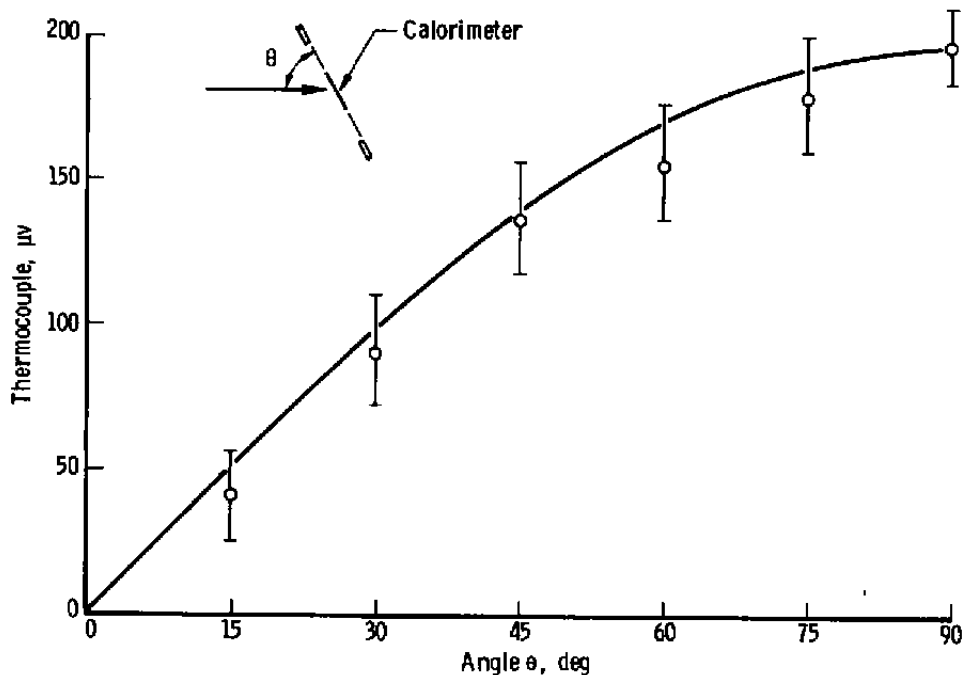


Figure 26. Angular dependence of energy accommodation.

(described in Section 4.0) was used to predict the number of collisions which could be expected for each calorimeter and the fraction of energy which would be absorbed for various accommodation coefficients. Table 2 presents a sample of some of these predictions. The experimental values of the energy accommodation coefficient for the cones ranged around 0.95.

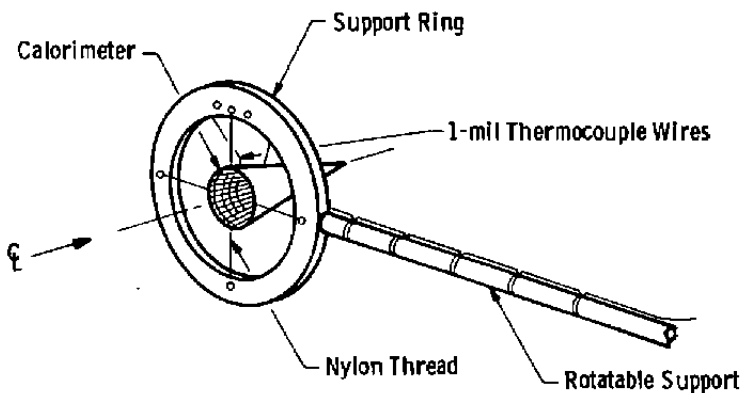


Figure 27. Conical calorimeter.

Table 2. GUMRAP Predictions for Energy Accommodation

Cone Angle, deg	Average Number of Collisions per Molecule	Energy Accommodation Coefficient Assumed	Fractional Energy Absorbed	ΔT Temperature Ratio Expected
30	5.87	0.50	0.9825	1.965
30	10.83	0.90	0.9995	1.110
45	4.98	0.90	0.9993	1.110
60	2.97	0.50	0.8704	1.741
	2.97	0.90	0.9975	1.108
	2.98	0.92	0.9987	1.086
	3.06	0.93	0.9990	1.074
	3.09	0.94	0.9990	1.063
	3.13	0.95	0.9991	1.052
	3.26	0.96	0.9993	1.041
	3.26	0.97	0.9994	1.030

3.4 VELOCITY OF PLASMA

The velocity of the plasma has been measured using several techniques. It is obvious that there can be significant differences in computed velocities when short distances and extremely short time periods are involved. Values from 30,000 m/sec to over 60,000 m/sec were obtained from the various systems used with the micropound engine. Subsequent tests with the millipound engine have indicated reasons why there was such a disparity. The prime variable is in determining what should be taken as time zero. In the first tests the initial pulse from the main capacitor discharge was used as $t = 0$. Since this was not always repeatable with the micropound engine, a photocell was used to detect the light pulse from the discharge to set $t = 0$. The photocell was later abandoned since it was found that the prompt UV photons arriving at the downstream detector (Faraday cups or electron multiplier) gave an initial signal pulse followed by the delayed plasma ions. With the signal levels of the millipound engine an extended flight path with detectors at two different distances was used so that the plasma velocity could be determined without reference to a starting point.

It was noted that these velocities are close to 40,000 m/sec. Using the plasma velocity between detectors and calculating backwards to a time zero placed the plasma consistently at the exit plane of the engine in the middle of the arc discharge. That is at the end of the 15- μ sec discharge cycle and not at the initiation of the UV photon pulse. The variation of the 10 to 15 μ sec in the micropound engine data more than accounts for the variability in the calculated velocities. An example of the time-of-flight (TOF) data is presented in Fig. 28.

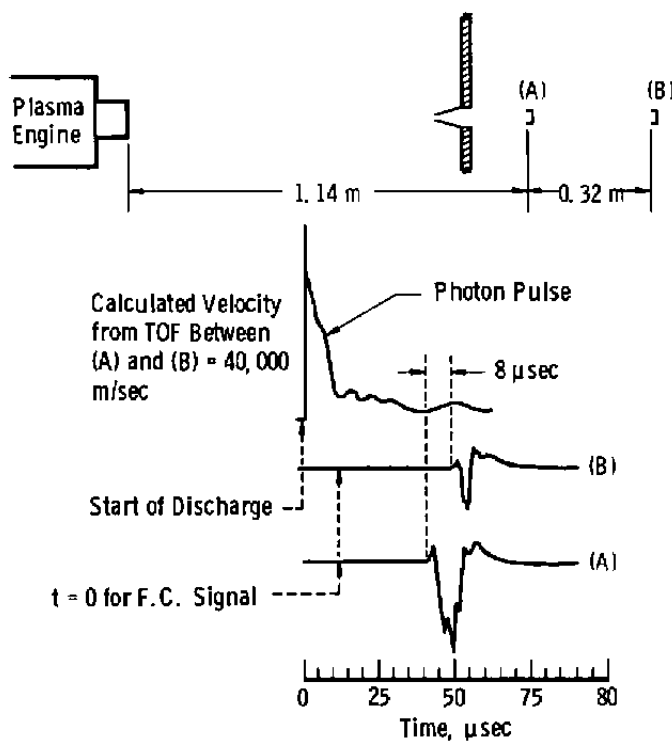


Figure 28. Plasma velocity.

Velocity profiles were taken across the plasma, and no significant variations were noted (Fig. 29). As one approaches the edges of the plasma, the signal level at the detectors drops and it is hard to define the location of the plasma peak. Therefore, it is difficult to determine whether there are any significant velocity changes at the plume edges. It should be noted that all the velocities were determined by rotating the engine and therefore that all velocities represent radial velocities. The axial component of the velocity at any location can be obtained by multiplying the measured value by the cosine of the angle.

3.4.1 Velocity of Material from Chamber Walls

A chopper wheel assembly was used to determine the velocity of material reflected from chamber walls. The chopper system, shown in Fig. 30, consists of a synchronous motor running at 200 rev/sec, turning a 6-in.-diam, 4-mil-thick stainless steel disk. At the edge of the disk are two holes used to chop the particle flux and a third hole which triggers a photocell/lamp system. This trigger pulse is used to fire the plasma engine and thus assures that the particle flux sampling holes are positioned at the same place for each engine shot. Behind each of the sampling holes is located a 3-in.-long detection surface. These surfaces have included a glass microscope slide, a Teflon sheet, and a stainless steel mirror.

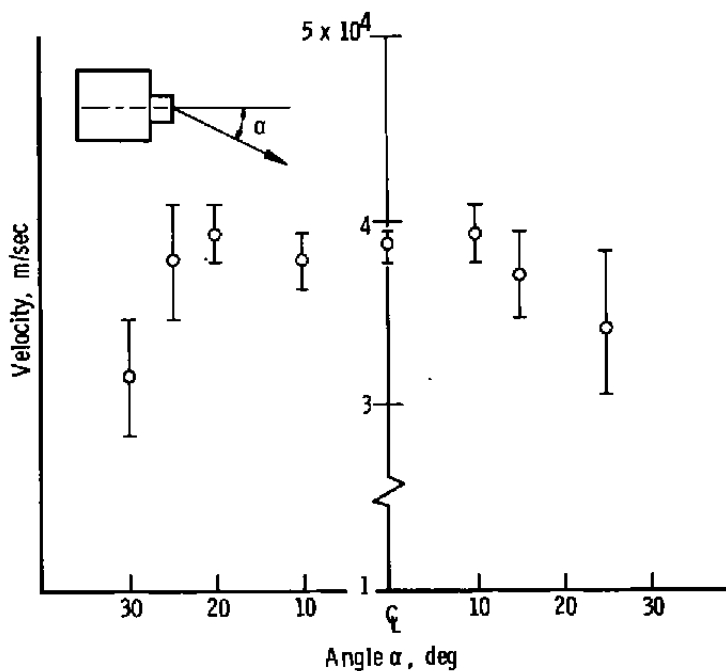
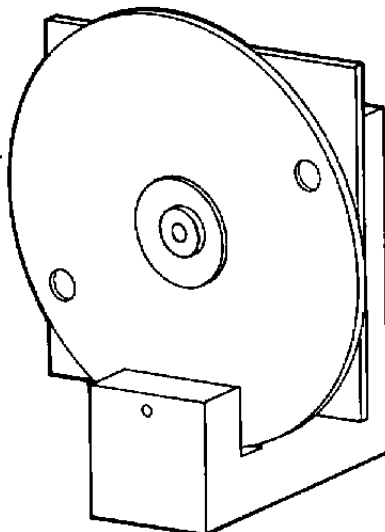


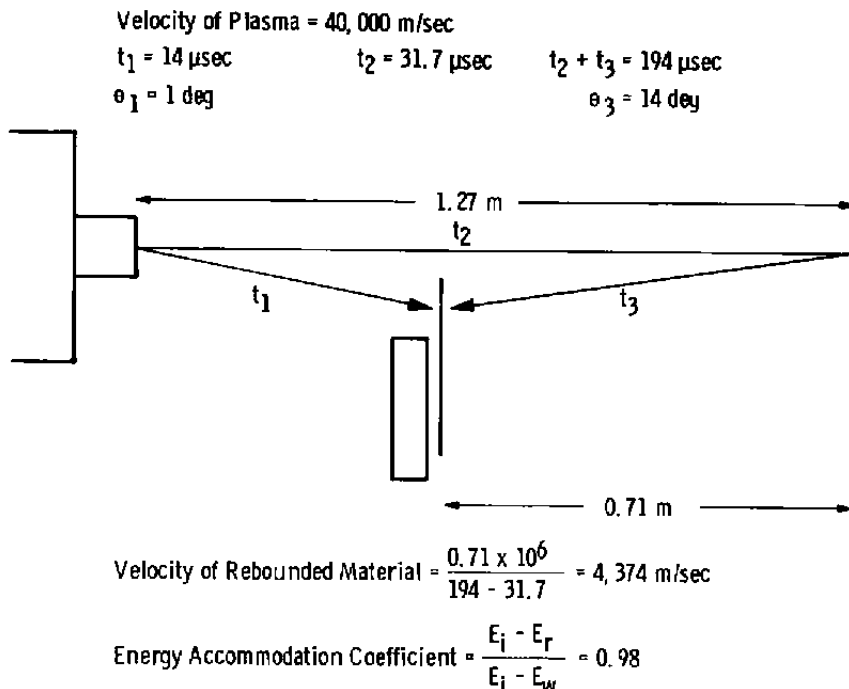
Figure 29. Velocity profile (horizontal).



a. Chopper wheel and witness plates
Figure 30. Chopper wheel.

The first part of the experiment consisted of locating the chopper downstream of the engine with the chopper wheel facing the plasma. After multiple pulses of the engine a circular deposit was collected on the sample plate. The sharp shadow edge and the circularity

of the deposit confirmed the repeatability of the starting of the engine from the photoelectric trigger and the extremely short duration of the plasma pulse.



b. Chopper wheel rotating at 12,000 rpm (13.88 $\mu\text{sec/deg}$)
 Figure 30. Concluded.

After this deposit had collected, the chopper system was carefully rotated 180 deg so that the sampling holes now faced the downstream wall of the chamber. The sample plates were not disturbed. After further engine pulses it was noted that a second deposit had accumulated, which was shifted by several degrees from the first. The rotational velocity of the chopper (from the synchronous drive, calibrated by a strobe system) and the distances being known, it was determined that the velocity of the plasma was $\approx 40,000 \text{ m/sec}$ and the velocity of the rebound material was $\approx 4,400 \text{ m/sec}$. If the rebound material is material from the plasma which has accommodated to the chamber wall temperature, then these data indicate an accommodation coefficient of 0.98. However, one must also consider the possibility that this material had been deposited on the walls from previous firings (possibly outgassing material coming from the engine nozzle after the plasma pulse) and is being sputtered by the plasma. In this case the energy accommodation is indeterminant from this experiment.

3.5 PLUME PROFILES

The flat plate calorimeter was used to map the plume profile of the micropound engine. During this test period the motor was mounted on a single degree of freedom gimbal, and thus data were obtained for just the vertical trace. The data are presented in Fig. 31. The bars on the data indicate the variability of the engine pulses and are in some cases an order of magnitude larger than error bars which could be associated with uncertainties in reading the thermocouple output. There is some indication that the thrust from this engine is not on the geometric centerline.

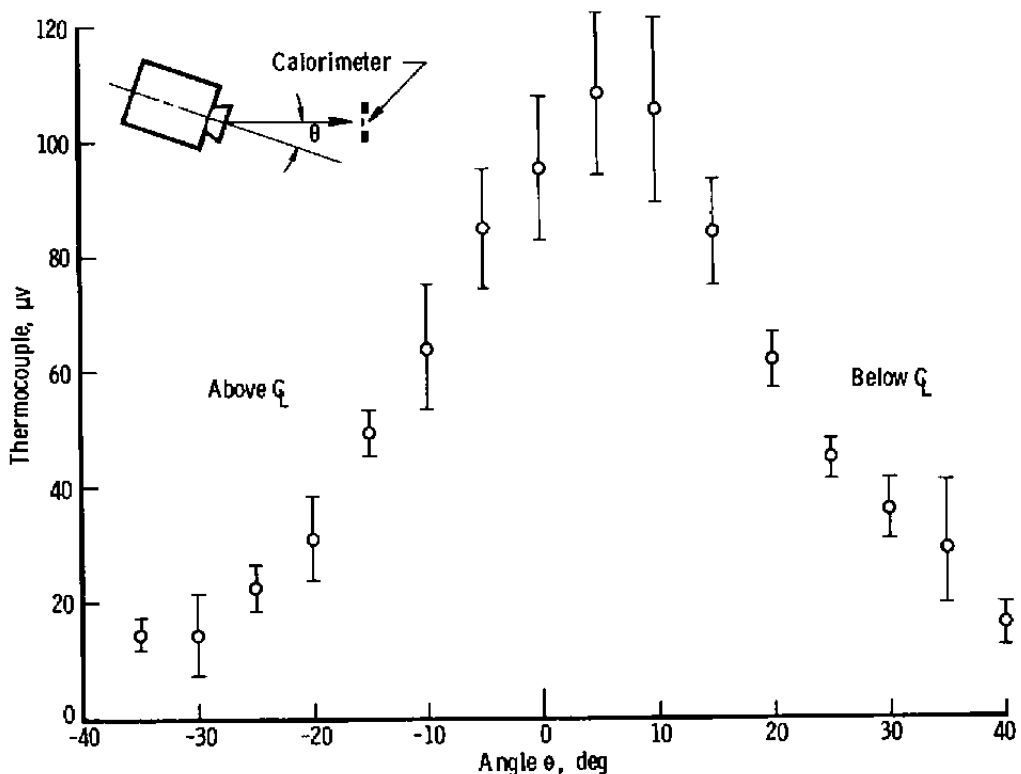


Figure 31. Plume profile of micropound engine.

These tests were repeated with the millipound engine. In this test installation the engine could be rotated in both the horizontal and vertical planes. Data are presented in Figs. 32 and 33. In this motor the peak intensity appears to be on centerline, although the overall intensity would indicate a thrust axis tilted toward the cathode. The plume is reasonably symmetrical in the horizontal plane. The apparent tailing of the intensity at -25 deg is most probably caused by a general heat load on the calorimeter from chamber wall reflections.

This is confirmed by the plume profile as taken by a Rogowski coil detector and presented in Fig. 34. This profile matches the calorimeter profile fairly well about the centerline but shows a much sharper plume boundary.

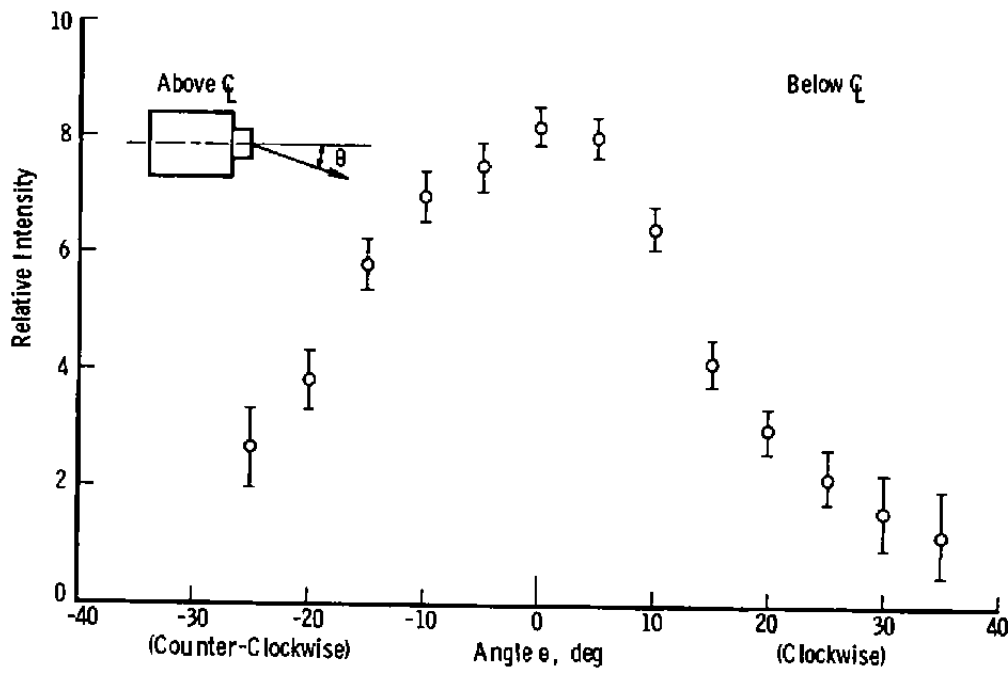


Figure 32. Plume profile of millipound engine (vertical).

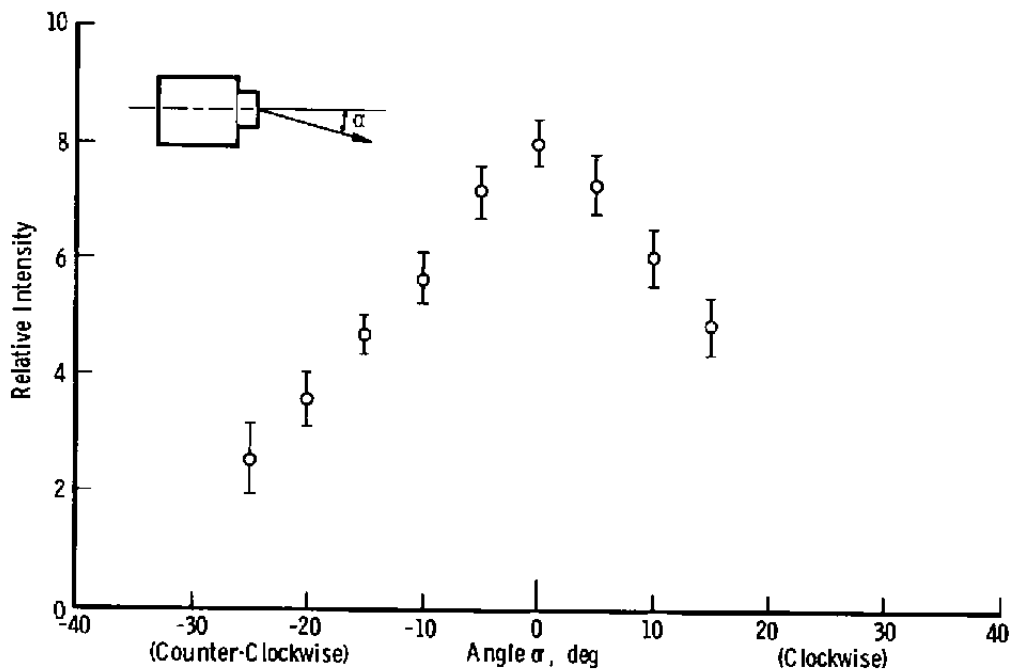


Figure 33. Plume profile of millipound engine (horizontal).

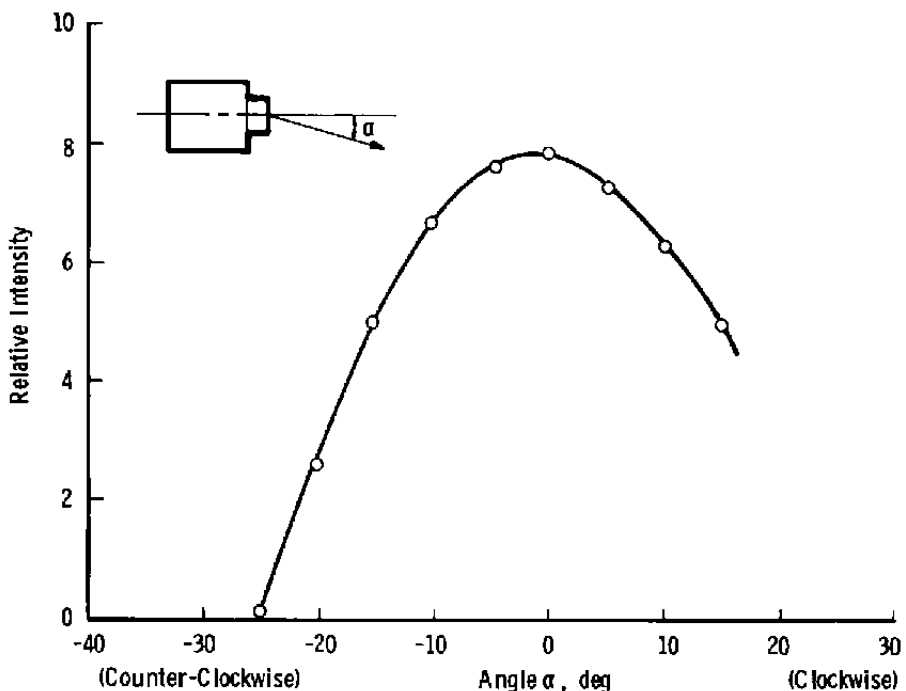


Figure 34. Plume profile (coil) (horizontal).

3.6 CONTAMINATION MEASUREMENTS

It is obvious that contamination measurements made in such a small chamber as the Aerodynamic Molecular Beam Chamber will be more influenced by wall effects than were the previous measurements taken at JPL or Fairchild. However, it was felt that some insight could be obtained on how chamber walls might contribute to the contamination problem.

3.6.1 ATR Plates (Micropound Engine)

An ATR plate was installed in the vacuum chamber during the first test series with the micropound engine. It was located approximately 20 deg off engine centerline, one meter downstream, and facing the plasma flux. A thin film of a light brown solid material collected on the crystal surface. An IR absorption spectrum was recorded on a Beckman spectrometer model IR4250. The instrument was operated in the dual beam mode with a clean and similar KRS-5 ATR plate inserted in the reference beam. The spectra of the engine deposit and a sample of pure Teflon are shown in Fig. 35. A similar comparison is presented in Fig. 36 of the engine deposit and a sample of DC704 diffusion pump oil. As can be seen, there is a closer correlation between the contamination spectrum and the pump oil than there is between the contamination and the Teflon. After this set of test pulses the cryoliner and

inner vacuum chamber walls were degreased with Freon, then scrubbed with a solution of Alconox detergent and water, and finally rinsed with both distilled water and alcohol. Several solvents were tried in an attempt to dissolve the deposit from the ATR crystal; these included freon, acetone, alcohol, methyl chloride, kerosene, benzene, carbon tetrachloride, and distilled water. None of these solvents had any effect. It was found that the deposit could be lifted from the crystal by pressing Scotch tape to the deposit and then rapidly pulling the sticky tape from the surface. The final cleaning of the crystal was accomplished with an abrasive polishing compound which was supplied in a standard refurbishing kit for restoring scratched crystals.

The crystal was replaced in the vacuum chamber and was allowed to collect material during subsequent engine tests. The only difference noted in this second contaminant deposit was that it took much longer to accumulate. The final absorption spectrum was not changed.

The facts that the spectra of the deposit and the pump oil bear strong similarities and that the rate of deposit was significantly reduced after an intensive effort to clean all the interior surfaces of the vacuum chamber both indicate chamber-induced contamination.

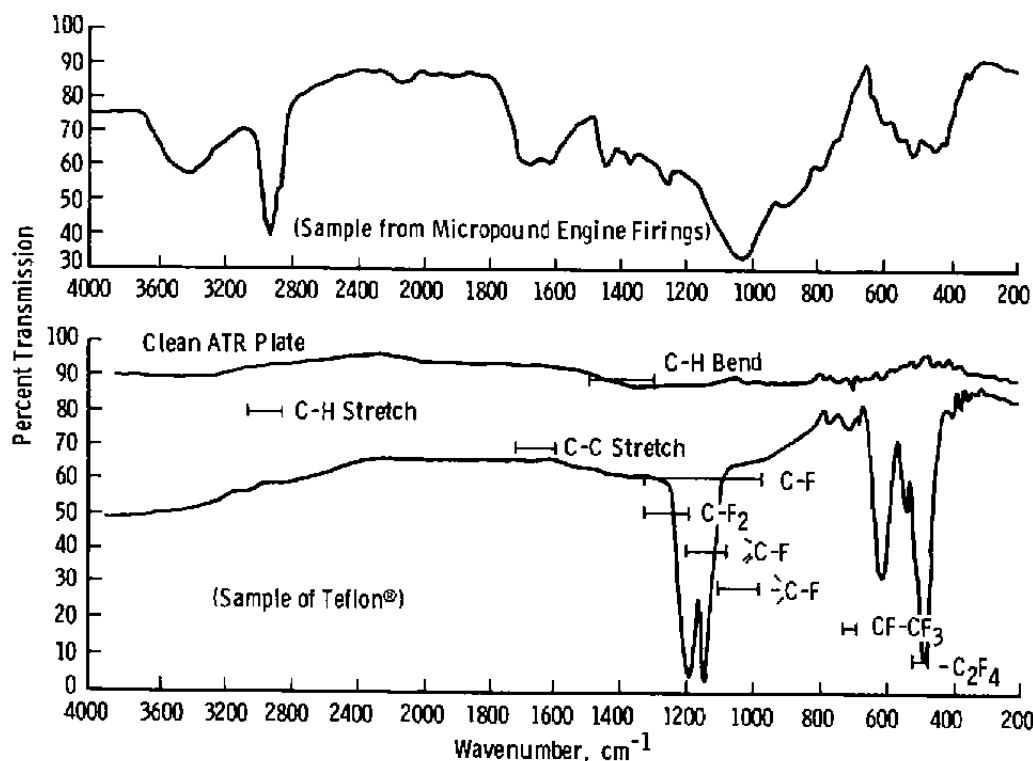


Figure 35. IR absorption spectra of contaminant and fuel.

The fact that the deposit was a solid and resistant to the common solvents suggests a fluorinated polymer.

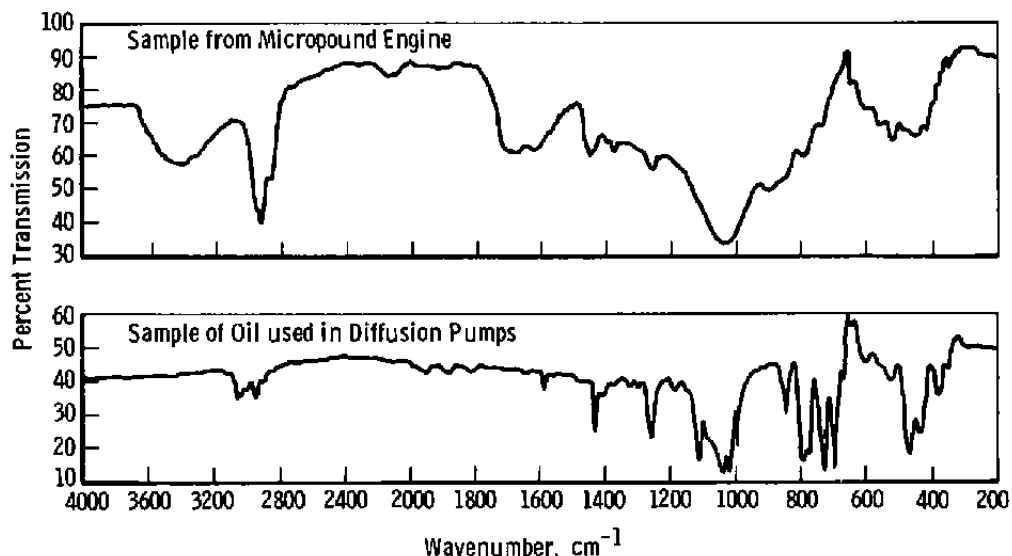
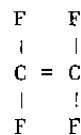


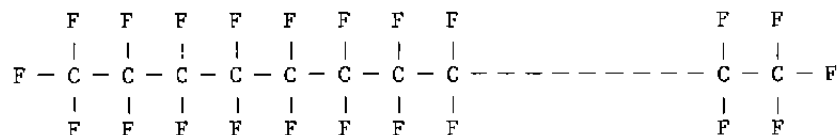
Figure 36. IR absorption spectra of contaminant and DC 704 oil.

3.6.2 ATR Plates (Millipound Engine)

The experiment was repeated when the millipound engine was installed in the vacuum chamber. The plate was removed after 2000 firings, and it was noted that it had accumulated a very thin but observable light brown deposit. The absorption spectrum is presented along with that for pure Teflon in Fig. 37. There are similarities in the absorption bands at 500 and 1200 cm⁻¹. However, there are also new features at 700 and 1700 cm⁻¹. These bands can possibly be explained by partial degradation of the Teflon fuel. Teflon consists of a linear polymer formed from C_2F_4 . As a gas, it has a molecular structure



However, in Teflon, the double carbon bond is broken and the molecules are attached in a linear chain, as follows.



The elements of this chain are more nearly comparable to the molecular structure of the compound C_2F_6 , which has a single carbon bond; i.e.,

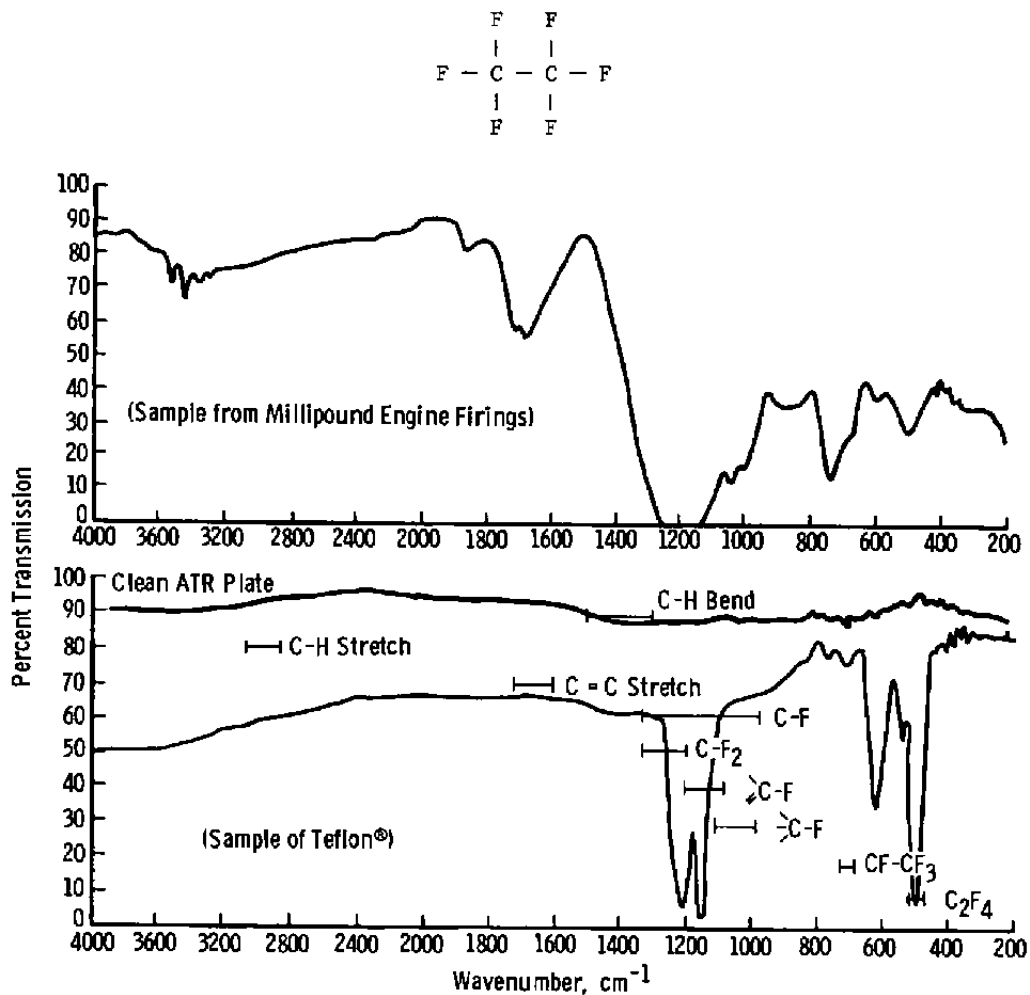
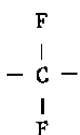
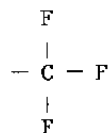


Figure 37. IR absorption spectra of deposit and Teflon® fuel.

The absorption spectrum for C_2F_4 is shown in Fig. 38, and it is noted that the double carbon bond $C = C$ results in an absorption band around 1700 cm^{-1} along with the strong absorption by the C-F bonds around 1200 cm^{-1} . The absorption spectrum for C_2F_6 is presented in Fig. 39. This spectrum again has the very strong absorption bands around 1200 cm^{-1} but also includes a strong absorption at 700 cm^{-1} from the CF_3 molecular cluster. This absorption is very weak in the Teflon spectrum since the bulk of the material consists of the



bonds. However, in the deposit this absorption band is very strong and thus indicates that the long polymer chains have been broken with a significant increase in the



terminations. Also, the presence of the absorption band at 1750 cm^{-1} would indicate that due to the disruptive discharge not only were the polymer chains being broken but considerable restructuring was occurring with the parent gas double carbon bonding becoming significant. Most of the absorption bands of the sample can be associated with processes involving partial decomposition of the Teflon fuel. The small contributions around 3500 cm^{-1} are probably from the C-H bond and thus indicate a minor contribution from test chamber contamination.

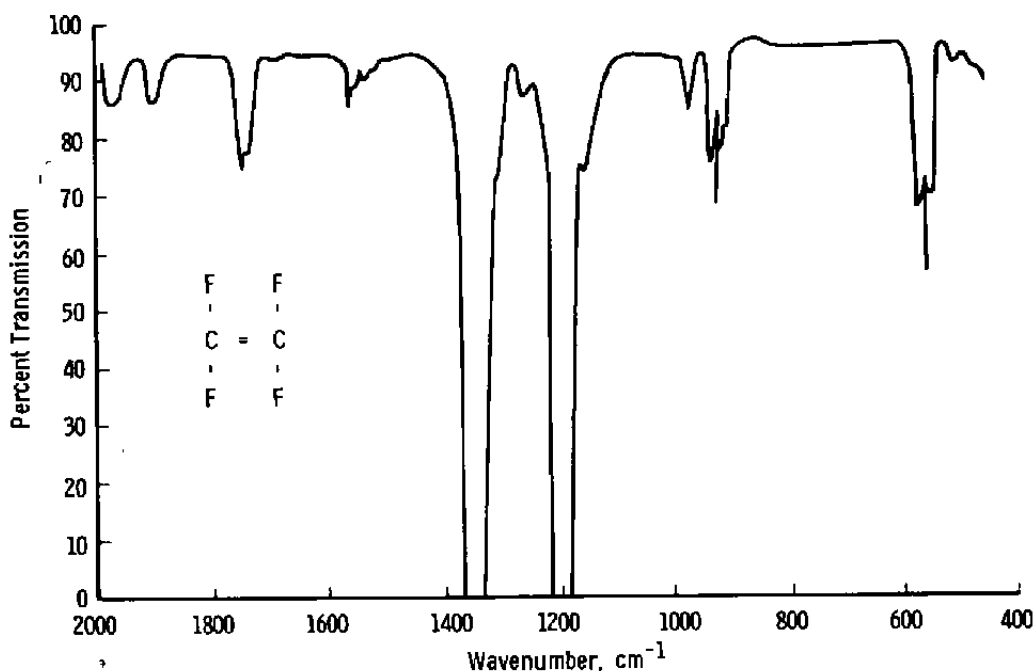


Figure 38. IR absorption spectrum of C_2F_4 .

The following general observations have been made:

1. Distinct shadows from mounting brackets holding the ATR plate suggest line-of-sight deposition from the area of the motor nozzle.
2. Deposition of similar material is observed on the test chamber walls at 90 deg to the nozzle axis at the nozzle exit plane. A cutout section of a mounting support

in this location also showed a slight shadowing effect, indicating some deposition directly from the nozzle. If this is the case, then the material undergoes a much larger expansion upon leaving the nozzle than does the plasma pulse.

3. Some of the material deposited in the backflow region that could not have come directly from the nozzle. This material either rebounded from chamber walls or was sputtered from the downstream chamber walls by subsequent plasma pulses.

The source of the partially degraded Teflon is obviously the plasma engine. However, at what time in the engine pulsing sequence it is produced and how it is transported in the vacuum chamber is not obvious. Further tests will be needed to answer these questions.

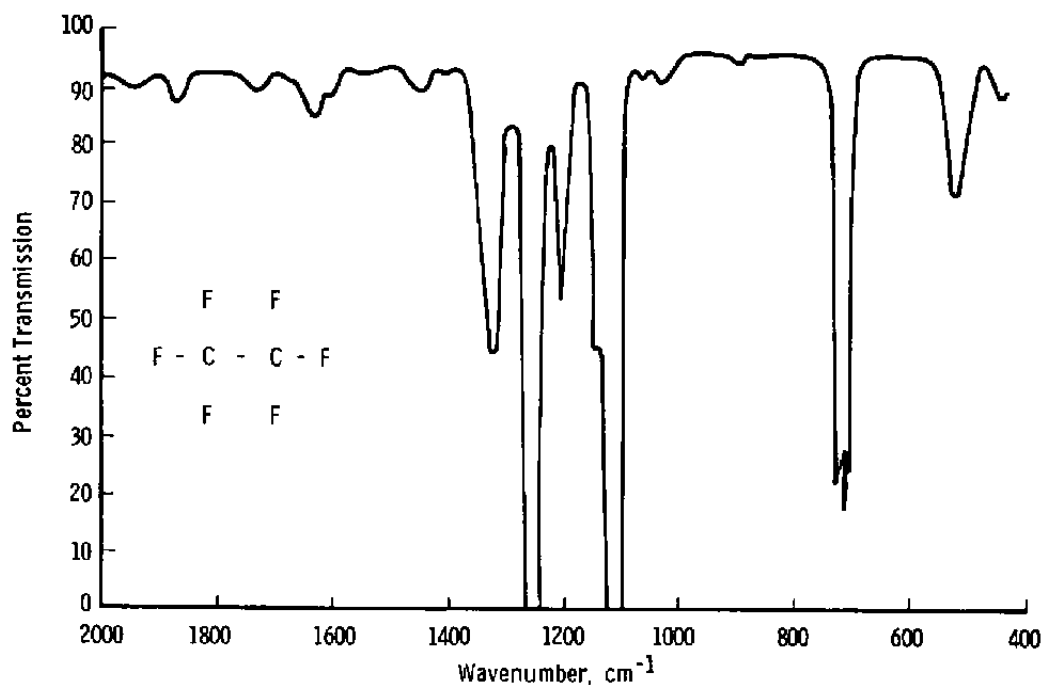


Figure 39. IR absorption spectrum for C_2F_6 .

3.6.3 Witness Plates

Glass microscope slides were installed at the exit plane of the ceramic shield on the millipound engine. The first set were located perpendicular to the nozzle axis (Fig. 40a). After approximately 2000 pulses these plates accumulated a very thin coating of the material described in the previous section. These slides were removed and a second set was installed

which extended approximately 1 cm beyond the nozzle as shown in Fig. 40b. These slides accumulated the same light brown deposit during the first 600 pulses. Sometime during the second 600 pulse series these slides collected a number of circular deposits. Photographs of a typical section of the deposit are shown in Fig. 41. Under the optical microscope the material appears to be composed of a transparent material in which is embedded an abundance of black particles. A photograph of one of the spots is shown in Fig. 42. The sample was viewed by transmittal light. Under the scanning electron microscope (SEM) the surface structure can be seen in more detail. The sequence of SEM photographs in Fig. 43 show that there are numerous sub-micron spheres along the periphery. An X-ray analysis of these spheres indicates that they are copper. An X-ray analysis of the rest of the deposit shows no X-ray spectral emission. However, a slight distortion of the spectrum baseline is evident, which is typical of a hydrocarbon or fluorocarbon sample.

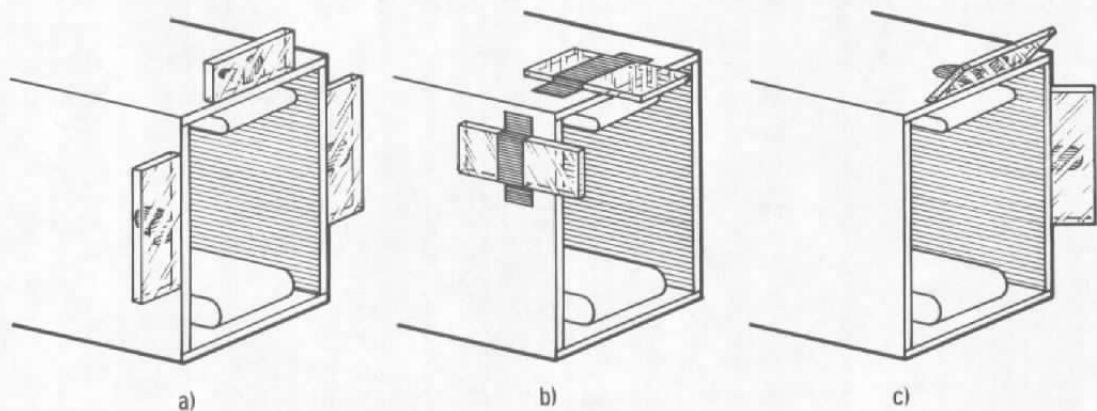


Figure 40. Glass sampling slides on nozzle.

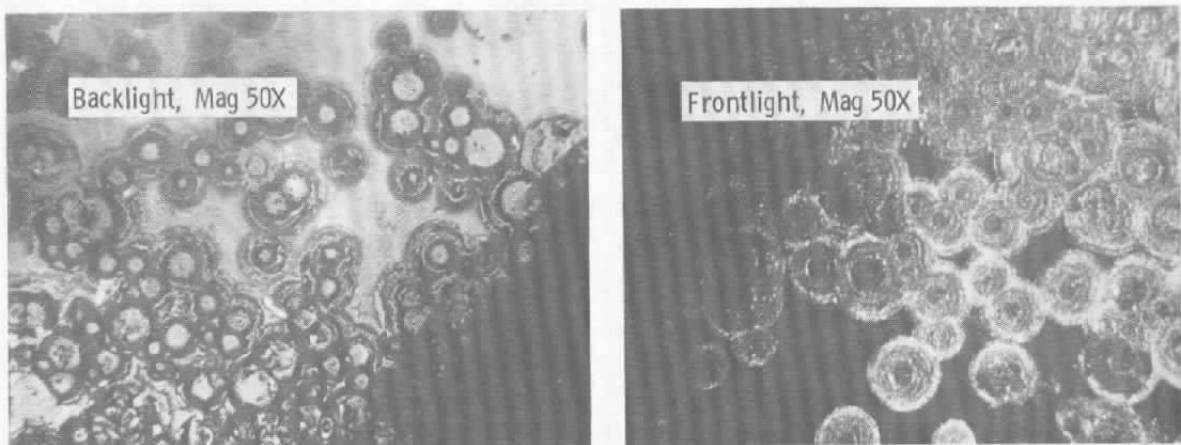


Figure 41. Particles from engine.

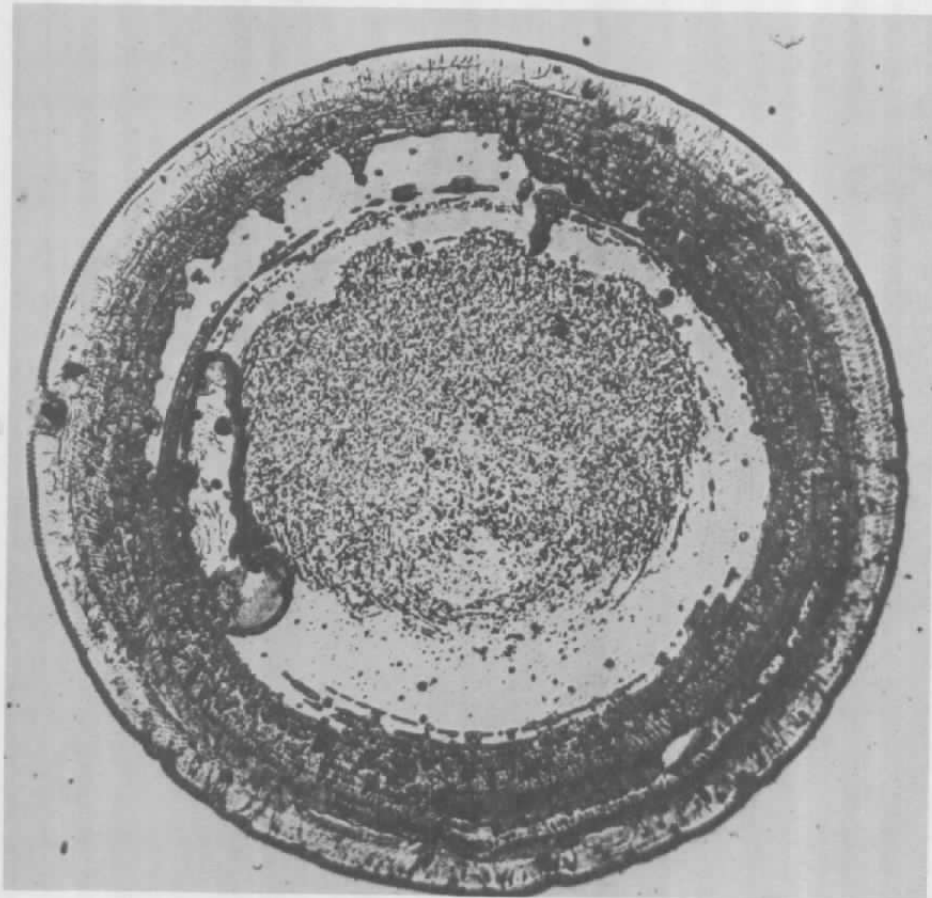


Figure 42. View of single droplet deposited on slide.

The fact that the deposits are circular and in places are overlayed would suggest that they arrived as liquid droplets and either were traveling so that they impacted normal to the sampling plate or, if at an angle of incidence, their longitudinal velocity was quite low. There was no indication of spattering or of elliptical residues on any of the sample slides.

A final test was conducted with a set of sampling plates set at 45 deg as shown in Fig. 40c. After 2000 pulses there was no indication of any droplets deposited. There are two possible explanations: 1) the mechanism for production of such droplets is quite erratic, and none were produced in this series of pulses; 2) the droplets formed and were emitted but were contained in an expansion angle of less than 45 deg. Further monitoring of the engine will be required to resolve this question as well as possibly to determine the mechanism for the droplet formation.

In addition to the witness plates at the nozzle, several plates were installed throughout the engine section of the chamber. Some of these were oriented with their collection surfaces horizontal, and some vertical. The results can be summarized as follows:

Vertical Plates:

- a. Those plates which viewed the nozzle exit accumulated a light brown film.
- b. Plates in the backflow region of the engine accumulated a deposit on that surface which viewed a portion of the test chamber receiving the main flux of the plasma pulse.

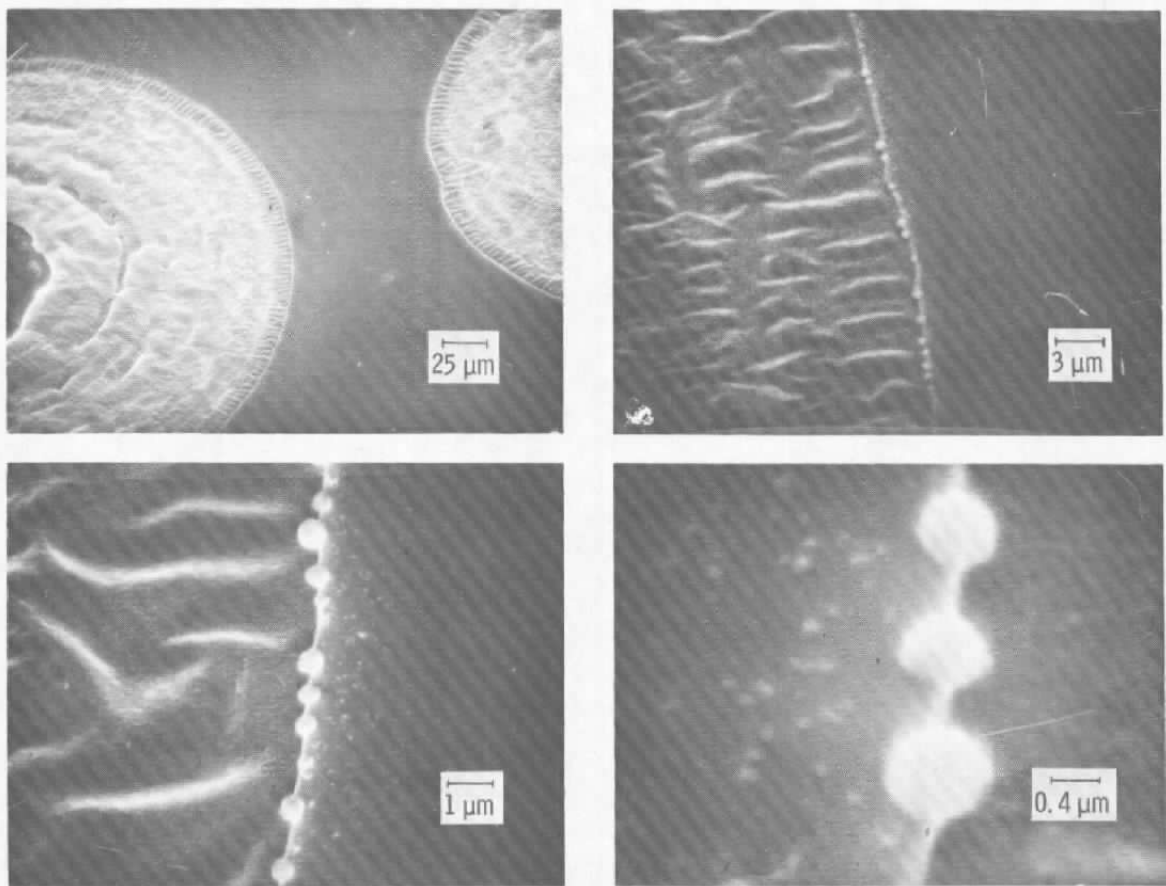


Figure 43. Droplets viewed under SEM.

Horizontal Plates:

- a. Evidence of a light brown deposit was found on those plates which had a field of view similar to that of the previously described vertical plates.
- b. In addition to the film deposits, those plates in the bottom of the chamber had a heavy accumulation of carbon particles. These were uniformly coated over the plates and were fairly uniformly distributed over the whole of the test chamber, including the area behind the engine.
- c. Plates in the upper section of the chamber had few to no carbon particles on their upper surfaces.

The carbon particles found on the witness plates were in the form of flakes varying from 1 to 500 μm in diameter. Scanning electron microscope photographs of typical particles are shown in Figs. 44 and 45. These flakes are similar to the carbon buildup on the anode of the

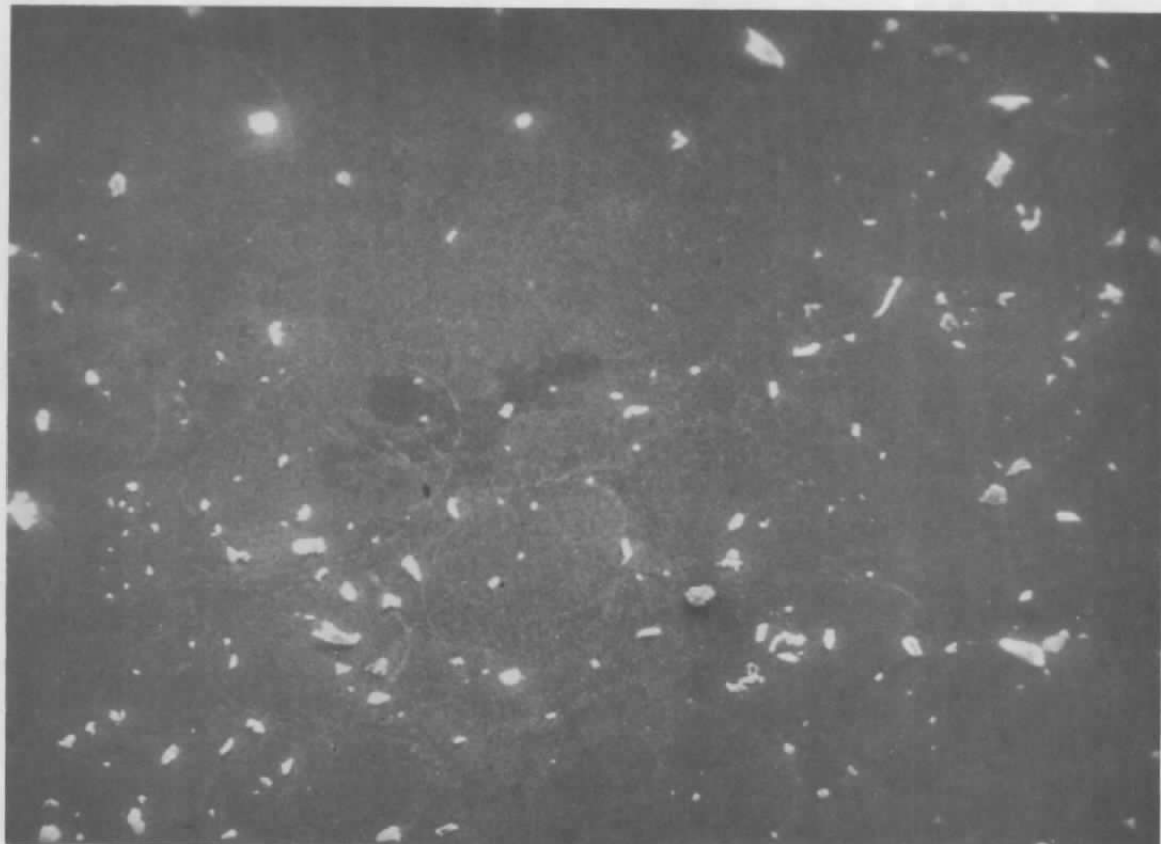


Figure 44. Carbon particles on sample plate (mag. 120X).

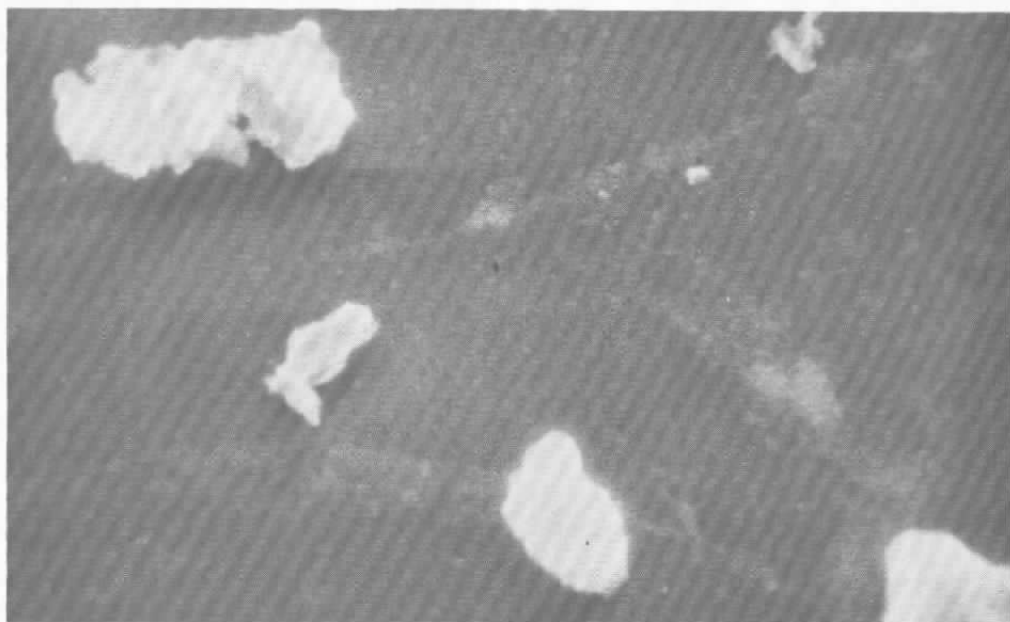


Figure 45. Carbon particles on sample plate (mag. 1200X).

engine as shown in Fig. 46. It is not known whether these particles are emitted with every pulse or whether there is a gradual buildup on the anode and then an intermittent burst. It is also not known whether these particles are transported by gas dynamic forces or whether they are accelerated by electromagnetic fields. It is obvious that they are bouncing around the chamber and gravitationally settling on all the horizontal surfaces in the lower part of the test cell. Some witness plates located in containers with specifically oriented orifices might be used in future tests to help determine the dominant particle trajectories.



Figure 46. Carbon flakes on anode.

4.0 ANALYSIS OF BAFFLE SYSTEMS FOR ENGINE TESTS

A proposed method for reducing the contamination from chamber wall effects would be to use a larger chamber containing a baffle system to entrap the plasma and cryopumps to capture the high energy plasma. Several surface collisions will generally be required to reduce the energy to a level at which cryopumping will occur. A baffle system for the 12V chamber has been devised and is pictured in Fig. 47. A simple parametric study of this baffle design (several similar configurations) has been conducted to analyze the molecular flow characteristics within the chamber to help understand and evaluate the capture efficiency of the design (i.e., reduction of backflow generated by chamber walls). The parametric study was accomplished using an analytical computer code (GUMRAP) for analyzing molecular flow in space simulation chambers.

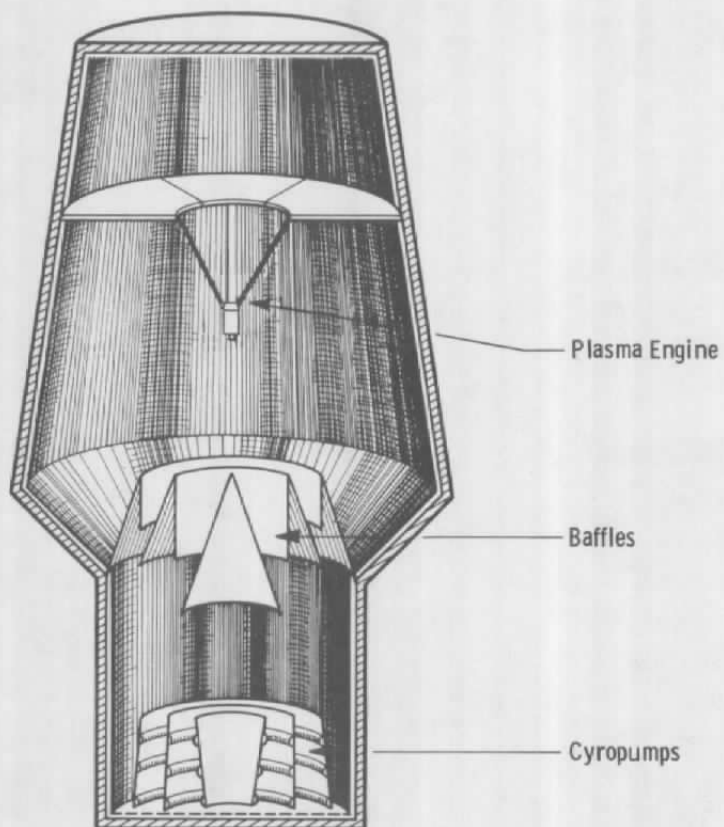


Figure 47. 12V chamber and baffle system.

4.1 GUMRAP COMPUTER CODE

The General Unwanted Molecular Rejection Analysis Program (GUMRAP) was developed (Ref. 8) to analyze molecular flow in space simulation chambers. GUMRAP provides the capabilities for modeling a space simulation chamber having baffles, ducting, and similar complex systems. GUMRAP was developed from an optical analysis program called the General Unwanted Energy Rejection Analysis Program (GUERAP) (Ref. 9), which uses a Monte Carlo ray trace technique to analyze the radiation characteristics of complex optical systems. The geometric and ray trace portions of GUERAP are used in GUMRAP. The major modifications to GUERAP were the elimination of several unnecessary radiation subroutines and the addition of a gas-surface interaction model. The statistical approach (Monte Carlo method) to the solution of molecular flow among surfaces within a space simulation chamber makes it possible to analyze complicated systems not amenable to conventional analytical or other computer methods. The Monte Carlo method is used to represent molecular flow statistically as rays which can be traced through the system. Each surface collision encountered is simulated using a reciprocity gas-surface interaction model (Refs. 8, 10, and 11).

4.1.1 System Configuration

The basis of the GUMRAP program is to trace probable molecular paths within the system as the molecule interacts with surfaces along its path. The present GUMRAP program is concerned only with molecular flow through nonparticipating media. Thus, interactions occur only when a molecule intercepts a surface within the system.

The system configuration consists of two special surfaces designated the entrance and exit apertures. The entrance aperture is one in which molecules enter the system according to a probability scheme explained in a later section. The exit aperture is one specified such that molecules which encounter this surface will exit the system. Molecules which strike the exit aperture plane will terminate ray tracing for that particular molecule, and a new molecule will be generated at the entrance aperture. The exit and entrance apertures are two of thirty possible surfaces specified to simulate a total system.

In order to detect gas-surface interceptions, it is necessary to represent the surfaces by some type of mathematical expression. Analytical equations are used in GUMRAP to define the surfaces and surface boundaries (constraints). Several simple surfaces (planar, spherical, conical, etc.) had been developed (Ref. 9) as the basis of a general chamber system. When a surface is to be defined and does not correspond to one of the simple surfaces, it must be specified via the coefficients of a general quadratic equation. Only surfaces which can be

expressed as general quadratic equations are entered into the program. A detailed explanation of the method for representing system coordinates, simple surfaces, and general surfaces, and for entering data into the program is given in the GUMRAP user's manual (Ref. 8).

4.1.2 Input Parameters and Output

A brief description of the various input parameters is presented in this subsection. There are several types of inputs to GUMRAP, including the following:

1. Geometric inputs for system configuration definition.
2. Properties of the surfaces that make up the geometric system.
3. Properties of incident molecular beams in regard to molecular weight, velocity, initial direction of molecular beam, and maximum angular deviation from beam centerline.
4. Input data in regard to random number generation.
5. Options for printing output.

All data entered are via the name list statement format, a standard feature of FORTRAN.

Several types of surface properties can be specified for each surface in the system. Up to 25 different combinations can be specified for a single surface. The surface properties which can be specified include the following:

1. The probability that a molecule will be reflected from a surface according to a reciprocity model.
2. The probability that a molecule will be reflected from a surface specularly.
3. The probability that a molecule will be reflected diffusely with no change in speed.
4. The surface temperature in degrees, Kelvin.
5. The tangential energy accommodation, α_x and α_z .
6. The normal energy accommodation, α_y .

If the probability of molecular reflection according to the reciprocity model is zero, then the last three surface parameters (temperature and accommodation coefficients) can be omitted since they are necessary only for the reciprocity model.

The Monte Carlo method in GUMRAP uses a pseudorandom number sequence generation subroutine. This number generator requires an initial starting value (seed) which is an odd integer less than 2^{31} . Variance of this starting value has negligible effect on the statistical results of the program as long as the total number of molecules entered (must be specified also) is large.

Several output options are available (each must be specified) to analyze the results of the molecular flow and to verify that all input parameters have been properly specified. The first output generated "echoes" the input data cards for verification. A summary of all geometrical surface and constraint coefficients is printed. A summary of the surface properties is printed to insure that each parameter has been properly specified. All program control parameters are listed systematically. All of the output described above is printed automatically. Other types of output describing the results from each execution of GUMRAP can be requested and include the following:

1. Molecular ray tracing of each surface collision, the geometric location of each collision, and the energy before and after the collision for a specified number of the total molecules traced through the system.
2. A spatial molecular distribution on the exit aperture.
3. A spatial energy distribution on the exit aperture.
4. A summary of the number and total energy of exiting molecules as a function of the number of collisions before exiting.
5. A radial molecular count distribution of molecules on the exit aperture.
6. Spatial and angular molecular count distribution on the exit aperture.
7. Thermal energy absorbed by surface per unit of external energy generated and number of molecular collisions.
8. Surface collision history of previous surface encounters (indicates the surface from which molecules were reflected when colliding with another surface).

9. Distribution of surface energy exchange (indicates the previous surface from which a molecule transfers energy during a surface collision).

The last two outputs (8 and 9) are new additions to GUMRAP. A subroutine, OUTP, has been added to GUMRAP to print, in matrix form, the total number of molecules colliding with a surface and the relative percentage arriving from each of the other surfaces.

4.1.3 Molecular Beam Source

Two aspects of GUMRAP should be noted. These are:

1. The method by which molecules are generated (velocity and distribution) at the entrance aperture.
2. The characteristics of the gas-surface interaction model.

The model uses a mono-energetic source which is uniform over the surface of the entrance aperture. This is in contrast with measurements of the plasma which have a narrow velocity distribution and indication of a density gradient from centerline to the plume boundary. The gas-surface interaction model has been slightly changed to allow specific surfaces to cryopump. The molecular beam source described in this subsection, and the gas-surface interaction model is explained in Subsection 4.1.4.

The Monte Carlo molecular generation technique allows only one molecule to enter the system and exist at any given time during execution. One of the surfaces composing the geometric system is designated the entrance aperture. The molecules are generated uniformly over the entrance aperture in a given beam direction and have a specified maximum divergence at any point on the entrance aperture.

Figure 48 illustrates a typical diverging molecular beam passing through a circular entrance aperture. The aperture shown is oriented on the X-Y plane of the system coordinates, although this is not necessary. The molecules enter the aperture by the randomized Monte Carlo technique. The direction of the molecular beam as a whole is defined by the elevation angle, ϕ , and the azimuthal angle, θ . The divergence of the beam (half angle, δ) is specified and provides a maximum angular deviation from the general beam direction. The molecular speed is constant for entering molecules; however, the direction is randomly selected within the divergence of the beam as illustrated in Fig. 48. If δ is specified as zero, the direction of every molecule will be the same and will correspond to the specified beam direction.

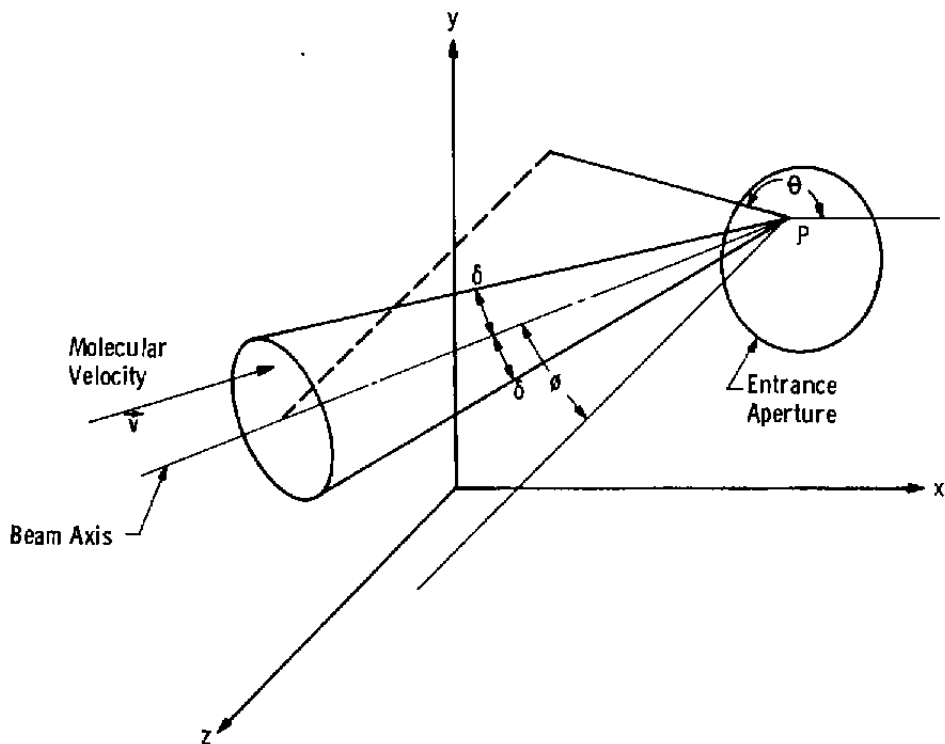


Figure 48. Entrance aperture and molecular beam geometry.

4.1.4 Gas-Surface Interaction Model

The gas-surface interaction model developed by Kinslow (Refs. 8, 10, and 11) is used in GUMRAP to model the surface interactions in the space chamber. Kinslow assumes that the interactions between a gas and a surface are time-independent and may be expressed mathematically by means of a scattering kernel (Ref. 11). The scattering kernel relates the probability that a molecule with velocity V will be scattered by a surface into a velocity close to V as illustrated in Fig. 49.

Physically the scattering kernel, expressed in rectangular coordinates, gives the probability that a molecule with velocity components v_x , v_y , and v_z will be reflected from a surface with velocity components v_x , v_y , and v_z . When the Monte Carlo method is used, there are two distinct techniques which can be used to determine the reflected velocities from the scattering kernel (Ref. 12). The method used by Kinslow (Ref. 8) in GUMRAP is the rejection technique, which is used frequently when involved mathematical equations are necessary for the evaluation of inverse probability functions. A complete explanation of the scattering kernel and its derivation, as well as a description of the Monte Carlo solution to the scattering kernel, is given in Refs. 8 and 12. The gas-surface model developed

by Kinslow describes scattering of a monatomic gas from an isotropic surface and has been successful in predicting the scattering characteristics of high energy argon beams from engineering surfaces. No comparable data have been examined to compare Kinslow's predictions with high energy ion beams scattered by engineering surfaces.

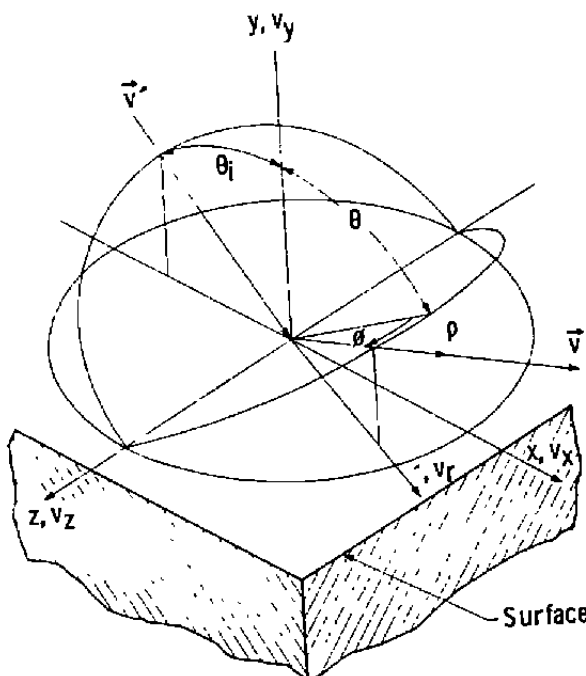


Figure 49. Coordinate systems for gas-surface interaction.

4.2 SYSTEM MODELING

The 12V chamber with baffles and cryogenic pumps (schematically illustrated in Fig. 47) was modeled using GUMRAP. For purposes of analysis, it is assumed that only the molecules which are reflected from the lower portion of the chamber and which propagate back to the plane of the plasma engine's nozzle will cause contamination due to the test chamber. Several geometrical chamber configurations were modeled with the entrance and exit planes at the same geometrical location (coincident and concentric) as illustrated in Fig. 50. The chamber configurations vary either from changes in the baffle design and/or cryopump orientation as illustrated in Fig. 51.

4.2.1 Plasma Beam Simulation

The plasma engine, when positioned as illustrated in Fig. 47, will eject plasma downward toward the baffle system into the section of the chamber which contains the cryopumps. The

plasma nozzle is simulated, using GUMRAP, by specifying the entrance aperture's position and relative size to be comparable to the mounting location within the 12V chamber.

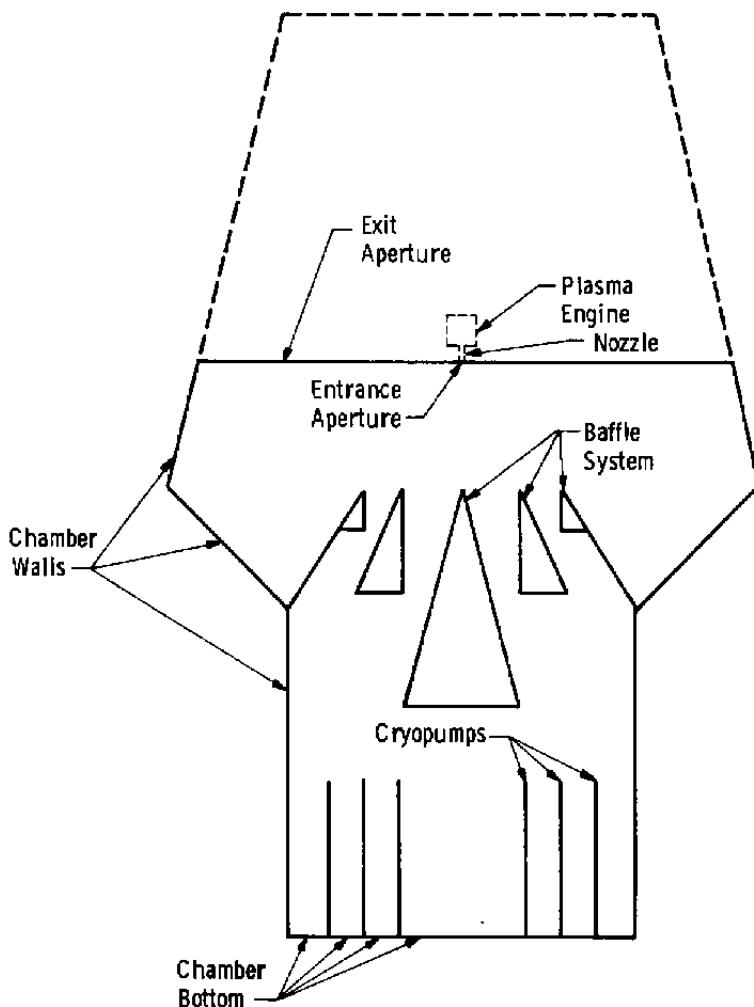


Figure 50. Example of chamber configurations modeled using GUMRAP.

The molecular beam in GUMRAP, which simulates the plasma pulse, enters the entrance aperture from above and has a maximum half-angle divergence, δ , equal to 35 deg. The distance between the entrance aperture and the baffle system was selected such that all molecules entering the system would either strike the baffles or directly enter the section of the chamber containing the cryopumps. The maximum beam divergence of 35 deg was selected as a result of the relative intensity measurements taken as a function of off-axis angle (see Fig. 32). Experimental measurements of the plasma indicate a narrow plasma speed profile; however, the intensity profile varies. The present version of GUMRAP

provides a capability to model a monoenergetic beam with each molecule having an equally likely directional probability but generated in a direction within the maximum divergence from the specified beam direction. This results in constant initial molecular speeds and a beam intensity profile which is also constant for each execution of GUMRAP. An initial molecular speed of 40,000 m/sec was specified to correspond to experimental data. A molecular weight of 18 was specified for each molecule generated. The parameters specifying the molecular beam remained the same for all chamber configurations modeled. A total of 10,000 molecules was generated for each execution of GUMRAP. A large number of molecules was necessary to provide a statistically symmetric density distribution of exiting molecules. It was desirable to select a number of molecules which would provide a satisfactory statistical distribution and at the same time use as little computational time as possible.

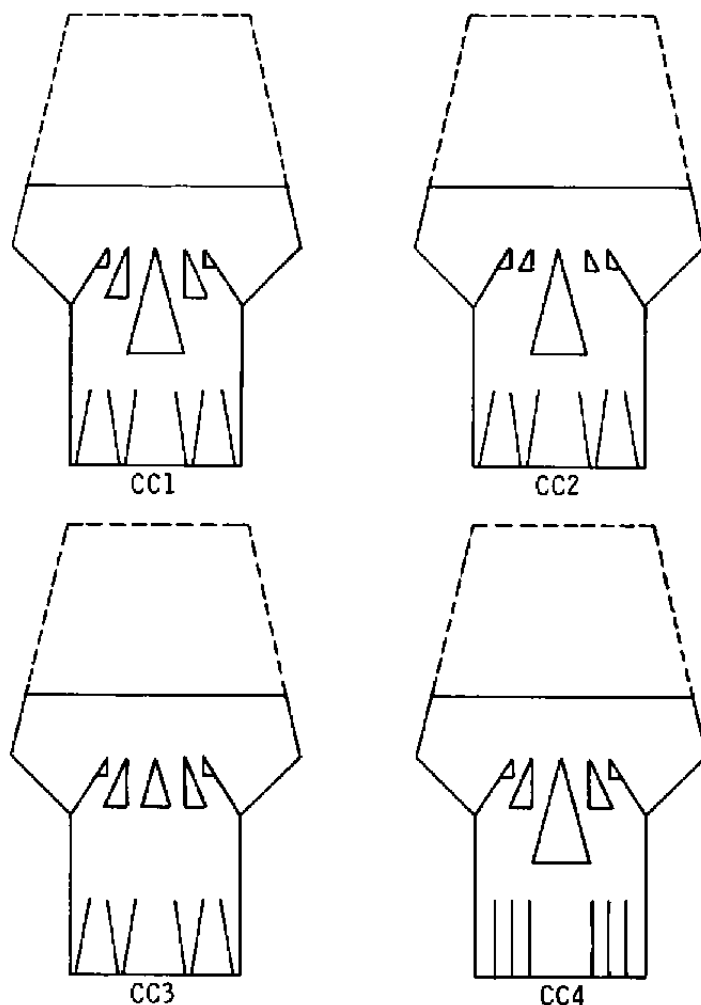


Figure 51. Chamber configurations (CC) modeled using GUMRAP.

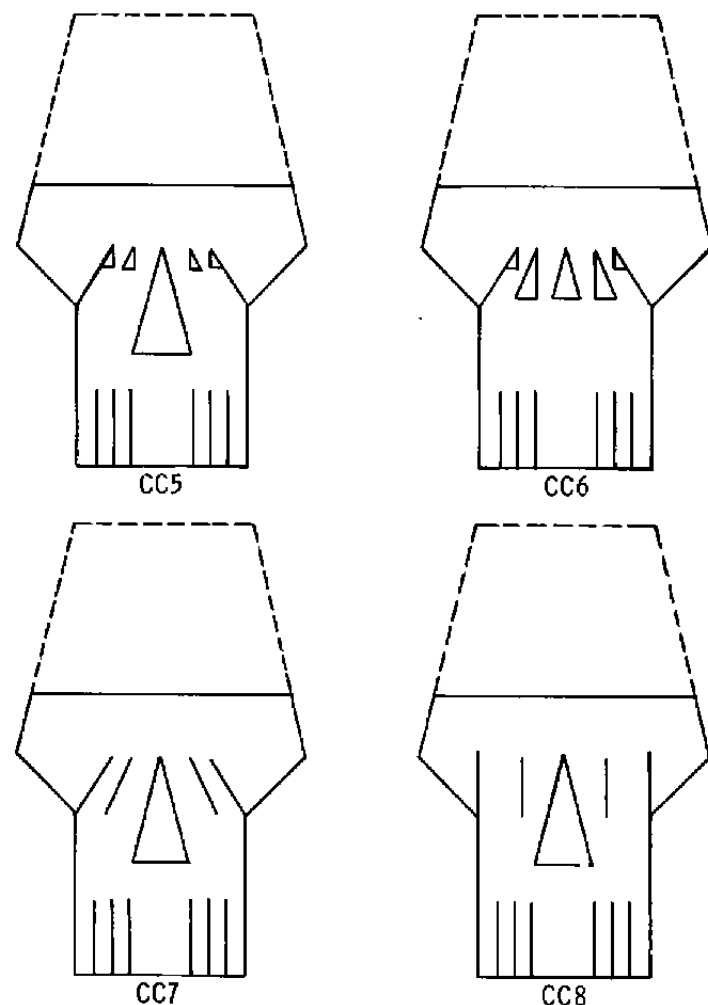


Figure 51. Concluded

4.2.2 Surface Simulation

Experimental investigations (Refs. 13 and 14) of atomic and molecular beam deposition on cryogenically cooled surfaces indicate that many factors are to be considered. Results considered of particular importance in this regard are those on the condensation, sticking, or capture coefficients, "critical temperature" for condensation, and binding energies of condensed atoms on surfaces. As many factors as possible should be considered when analyzing cryopumping effects. The gas-surface interaction model used in GUMRAP cannot simulate the effects of cryopumping. To provide a means for comparing the different chamber configurations, a simple modification was made to GUMRAP to simulate cryopumping effects. This requires a calculation of the energy of the molecule after each wall collision and a decision as to whether there is sufficient energy for it to leave the surface.

Normal use of GUMRAP requires specification of the maximum number of surface collisions for each molecular ray trace desirable or a default value of 20 is used. Addition of the cryopumping capability to GUMRAP causes molecular ray tracing to terminate when a molecule is cryopumped by a cryosurface or when the exit aperture is encountered. To simulate cryopumping of molecules, the energy (speed) of each molecule is compared to a maximum energy specified and is tested at each surface collision. If the speed of a molecule is less than a specified value and the surface encountered is a cryogenically cooled surface, then cryopumping occurs. If both of these conditions exist simultaneously during a molecular collision, ray tracing terminates and the kinetic energy of the molecule is transferred to the surface. A new molecule is then generated at the entrance and traced through each collision until it either is cryopumped or exits the system.

The criteria for cryopumping in this series of computer studies was that molecules striking a cryosurface and having a kinetic energy less than 1.0 ev would be cryopumped. (Since the molecular speed is checked at each collision, a maximum speed is specified at 3275 m/sec for a molecule having an atomic mass of 18.) Two cases were executed using a maximum energy of 0.1 ev for cryopumping to occur. Even though the physics of a gas-surface interaction is considerably more complicated, the energy level specified provides an approximation to simulate cryopumping. This simulation provides a method by which different chamber configurations can be compared.

All accommodation coefficients were specified at 0.9 for modeling the gas-surface interactions. Experimental determination of the accommodation coefficients indicated values of 0.9 or greater. Since the accommodation coefficient is independent of incident angle (Fig. 26), the tangential and normal components (α_x , α_y , and α_z) were given equal values.

The surface temperature of the baffles is specified at 300°K for all cases executed. The bottom of the chamber and the cryopumps were specified at 77 and 20°K, respectively. The temperature of the chamber walls was set at 300°K, and for a few chamber configurations the chamber wall's temperature was set to 77°K. The different cases are listed and discussed in Section 4.3. These temperatures are selected as a result of general vacuum and cryogenic systems using liquid nitrogen and gaseous helium for cryopumping space simulation chambers.

4.3 RESULTS OF THE CRYOPUMPING SIMULATION

As stated earlier, the objective of using a baffle system and cryopumping section is to reduce the number of molecules reflected from the chamber walls and returning to the plane

of the plasma engine nozzle. By simulating the 12V chamber containing the baffle system, cryopumps, and plasma engines, a method is available to parametrically assess different chamber configurations. A summary of the results of this simple parametric study is presented in this section.

Table 3 lists the percent of molecules (relative to 10,000 generated) which reached the exit aperture for all cases executed. Table 3 is broken into three groups to differentiate between three common characteristics which some of the chamber configurations have (Fig. 51). The first group exhibits cryopumps having conic geometries, and the second group consists of different baffle designs with the cryopumps being cylindrical (constant radius for each cropump over its total length). The last group also has cylindrical cryopumps but differs by having only a single outer baffle.

Table 3. Percent of Molecules Reaching the Exit Plane

Conic Cryosurfaces in Bottom			
OCW = 300°K		OCW = 77°K	
CC1	CC2	CC3	CC3
0.87	0.72	0.91	0.28

Circular Cryosurfaces in Bottom						
OCW = 300°K					OCW = 77°K	
CC4, NC	CC4	CC5	CC6	CC4, $\alpha = 0.5$	CC4, NC	CC4
12.85	1.65	2.10	4.09	1.69	12.60	0.94

Singlet Outer Upper Baffles		
OCW = 300°K		OCW = 77°K
CC7	CC8	CC7
1.64	5.55	1.12

CC = Chamber Configuration

NC = No Cryopumping

OCW = Outer Chamber Wall

$\alpha = 0.9$ for all cases except as noted.

A baffle concept similar to that illustrated in Fig. 47 was modeled by the geometric configuration CC4. This chamber configuration (CC4) was executed first, followed by variations CC5 and CC6. With a chamber wall temperature of 300°K, accommdation coefficients equal to 0.9, and a maximum cryopumping energy of 1.0 ev, the percent of

molecules reaching the exit plane for CC4 is only 1.65 percent. The percent for CC5 and CC6, having similar conditions, is greater than CC4 but still less than 10 percent. Lowering the outer chamber wall temperature from 300 to 77°K reduced the exiting molecules by an additional 50 percent. Reducing the cryopumping energy criteria from 1.0 to 0.1 ev increased the number of exiting molecules slightly.

When the surface collision exits were examined (output data), it was apparent that approximately half of the exiting molecules had encountered only two surface collisions. The two-surface collision exiting molecules were not striking the baffle system but were first striking the cryopump and the bottom of the chamber and then exiting directly without striking any other surface. Changing the orientation of the cryopumps from circular to conic geometries eliminated the two-surface collisions. This change increased the probability of cryopumping those molecules which would normally exit after only two surface collisions.

An interesting phenomenon occurs when the cryopumps are changed from cylindrical to conic geometries. Chamber configurations CC1, CC2, and CC3 correspond (same baffle arrangement) to CC4, CC5, and CC6, respectively. The relative percent of exiting molecules increases going from CC4 to CC6, whereas it decreases going from CC1 to CC3. Again, this is explained by considering the two-surface collision exits occurring in CC4, CC5, and CC6. If the number of two-surface collisions is subtracted from each of the totals for CC4, CC5, and CC6, then the percentage of exiting molecules follows the same position (decreasing) in going from CC1 to CC3.

The last two chamber configurations, CC7 and CC8, have simpler baffle arrangements, and an increase in the percentage of exiting molecules occurs. Similar to CC4, CC5, and CC6, there is a large percentage of two-surface collision exits.

In all cases the percentage of molecules exiting decreases when the chamber wall temperature is reduced to 77°K. The conic cryopumps also help to reduce the number of exiting molecules. The chamber configurations used to model the 12V chamber had close to the maximum number of surfaces allowed in using the current GUMRAP program. Other baffle arrangements may prove to be more efficient than the ones modeled but will require more surfaces. Modifications to GUMRAP could increase the maximum number of surfaces allowed, providing the capability to model more elaborate chamber configurations if needed.

5.0 SUMMARY

5.1 OPERATION OF PLASMA ENGINES

The pulses from the micropound engine were quite erratic. This operating problem, coupled with the low signal levels, made it difficult to define its operating characteristics in sufficient detail to make comparisons with the millipound engine. However, the micropound engine was very useful in providing a plasma source with which to evaluate several diagnostic techniques.

The performance of the millipound engines was more repeatable, and the signal levels from most of the diagnostics were well above the noise. The long electrode version appears to have a more complex structure to the plasma pulse than the short electrode engine. This observation, however, is made with a relatively small amount of data from the short electrode plasma engine.

5.2 SPECIES PRODUCED BY THE ENGINE

The gases produced by the millipound engine are similar to those evolved in vacuum pyrolysis of Teflon. The dominant species are C_2F_4 and C_3F_6 . It was also observed that HF was produced, though there is some question as to whether this is a direct product of the engine or a secondary product formed from plasma/wall reactions. Secondary products which were identified as chamber wall reactions included significant quantities of CHF_3 .

The UV radiation data indicated multiply ionized carbon and fluorine atoms in the plasma. Attempts to measure the ion/neutral concentration in the plasma were not successful due to test chamber wall effects.

5.3 ENERGY ACCOMMODATION COEFFICIENT

Experiments conducted with calorimeters indicate a high accommodation coefficient (> 0.9); for purposes of evaluating baffles, this value can be considered to be independent of the angle of incidence.

5.4 VELOCITY OF PLASMA

The plasma ion velocities were measured at 40,000 m/sec. Attempts to measure a neutral component in the engine plume which might be traveling more slowly have not met with any success to date.

5.5 PLUME PROFILE

The plasma profile, as measured by calorimeters and a Rogowski coil, is well within the ± 40 deg cone as suggested by previous studies. For the long electrode millipound engine the horizontal plane boundaries are within ± 25 deg.

5.6 CONTAMINATION MEASUREMENTS

There are at least four types of material produced by the millipound engine which are potential contaminants:

1. *C_2F_4* — This is emitted as a gas, most probably during the cool-down period after the plasma has left the engine.
2. *Teflon sublimate* — This material is partially degraded Teflon. It is observed as a solid film coated on the inner surfaces of the nozzle and over most surfaces of the vacuum chamber. It apparently is deposited at the molecular level since SEM studies at high magnification show no structure which would indicate droplet or particle boundaries. The IR absorption properties of this material suggest that it has a much lower molecular weight than the 10^6 estimated for the virgin Teflon.
3. *An intermittent sputtering of a mixture of carbon, copper, and Teflon* — This mixture appears as particles which were collected on sample plates at the lip of the nozzle.
4. *Carbon flakes* — These particles appear to be shed from the carbon buildup which occurs on the electrodes.

5.7 ANALYSIS OF BAFFLE SYSTEMS

A computer code has been developed and used to compare various baffle configurations which might be used to trap the very energetic molecules emitted by the plasma engine. From this study a baffle array and an associated cyropumping system have been identified which should reduce the backscatter from the vacuum chamber walls to less than 0.3 percent.

6.0 CONCLUSIONS

The results from these tests with the pulsed plasma engines indicate that an effective baffling and cryopumping system could be built which would capture the high energy plasma and minimize molecular backscatter. However, there are several factors which would suggest that a full-scale test to try to measure backflow contamination from the engine might be premature.

1. The engine used at AEDC to develop the plasma pulse for the plasma/surface experiments is not typical of the flight version.
2. There is not sufficient information concerning the operating characteristics and the possible contamination mechanisms to develop a mathematical model for the millipound engine. These data can be obtained more economically in the smaller research chamber.
3. There is strong evidence that the plasma pulse is followed by hot gas expansion which would be backscattered by the proposed plasma baffle system. This gas may be the most significant component of any contamination from an operational engine in space.
4. There is a strong secondary electron emission when the plasma interacts with chamber walls or baffle surfaces. This electron pulse together with the strong UV radiation from the engine presents severe problems in using such diagnostic tools as mass spectrometers, fast response ion gages, Faraday cups, and electron multipliers.

In lieu of an immediate contamination measurement program in the AEDC 12V vacuum chamber, the following tests are suggested.

ENGINE MODIFICATION

This will require modifying the engine to conform to the current design for the flight version. It will consist of replacing the present 60-mfd capacitors with 80-mfd units and possibly changing the nozzle or shield assembly.

ENGINE OPERATING PARAMETERS

The first tests will be to remap the plasma flow field and measure the velocities to see if the changes in engine configuration have had any influence on the plasma pulses. This work will be accomplished using the present capabilities, i.e., calorimeters, Faraday cups, electron multipliers, Rogowski coils, etc.

EXIT PLANE DATA

There are several diagnostics which might be used to obtain data concerning the conditions at the exit plane of the engine during and immediately following a plasma pulse. Some of them have been demonstrated; others are considered feasible from preliminary information gathered during these tests.

a. Map Ion Species In Plasma at Exit Plane

A VUV spectrometer was used to observe the emissions at the exit plane. The spectrometer viewed approximately a 4-in.-square field starting at the exit plane. This yielded spectra from the plasma mainly on centerline. The field of view will be reduced and a scan of the exit plane made to identify ions at each electrode.

The intensity of the VUV emission is sufficiently intense that the spectrometer can be set at a specific wavelength and the intensity recorded as a function of time. This will provide a map of specific ion concentrations as the plasma passes through the field of view of the spectrometer. These data will be recorded along with a coincidental trace of the discharge current from the capacitor bank in order to compare ion intensities with plasma currents.

b. Velocity of Ions

The velocity of the ions in the plasma as measured by time of flight techniques is on the order of 40,000 m/sec. At this velocity there should be sufficient doppler shift to determine the velocity of specific ions. An attempt will be made to make such a measurement. The data from an axial observation of the plasma should indicate a line broadening with the dominant radiation from the slowly accelerating arc in the engine throat, and a much smaller contribution from the high velocity plasma which has been emitted from the engine.

c. Plasma Photography

Time exposure photographs have been made at the exit of the engine. These photographs indicate some asymmetry which may be due to the current reversal which occurs during the discharge cycle. It is proposed that a Kerr cell be used to obtain photographs of the plasma leaving the electrodes. From the previous photography, it would appear feasible to use 200-nanosecond exposure times. The cell will be triggered with appropriate delays by the present timing sequencer which is used with the engine. This will provide time sequence photographs of the plasma pulses as they leave the engine. The available viewports will permit photographs to be taken both from the side and from above the engine.

d. Exit Plane Magnetic Field

Data will be required in order to model the electromagnetic and aerodynamic forces which are accelerating the plasma and associated gases. A miniature coil sealed in a glass probe will be used to map the magnetic field as a function of time at the exit plane of the engine.

e. Exit Plane Current Flow

A small Ragowski coil will be built and used to map the current flow in the plasma as it leaves the electrodes at the exit plane. These data will be used to complement the high speed photographs in defining the plasma acceleration and separation from the electrodes.

f. Analysis of Teflon

From the tests reported herein it was found that some of the gas species contained hydrogen. Two gases specifically identified were CHF_3 and HF. Early indications pointed to chamber wall contamination as the H_2 source. However, some UV spectra indicate the presence of H in the plasma and thus suggest that the hydrogen may be from the Teflon. Thus, a careful analysis of samples from the Teflon fuel will be made in order to determine any hydrogen content. This would be accomplished by vacuum pyrolysis and mass spectral analysis of Teflon samples at AEDC and by NMR analysis by the Aerospace Corporation.

g. Analysis of Gas Species

The engine produces both gases and particulates in addition to the ionized plasma. Cooled QCM's can collect the gases and possibly trap the particles but can only give a net mass increase per engine pulse. In order to supplement these data with information on gas

species, the mass spectrometer will be installed with collimators so that it can monitor specific mass numbers. Since the mass spectrometer is sensitive to both VUV photons and the chamber-induced electron showers, it will be shielded by a chopper wheel synchronized to the engine firing to block the photons and by a retarding potential grid to deflect the electrons. If necessary, a prototype baffle system will be built for the research chamber to minimize the chamber-induced backflow to the mass spectrometer.

REFERENCES

1. Busby, M. R., Dawbarn, R., Kinslow, M., et al. "Spatial and Velocity Distributions of Monoenergetic N₂ Molecular Beams Scattered from Various Engineering Surfaces." AEDC-TR-71-171, (AD889603L), December 1971.
2. Arnold, F., Dawbarn, R., and Busby, M. R. "Interaction of a Monoenergetic Nitrogen Molecular Beam with a Solid Nitrogen Surface." *Applied Physics Letters*, Vol. 17, No. 4, August 15, 1970.
3. Weise, W. L., Smith, M. W., and Glennon, B. M. *Atomic Transition Probabilities*, Vol. 1, NSRDS-NBS 4, U. S. Government Printing Office, Washington, D. C. 1966.
4. Harrison, G. R. *M.I.T. Wavelength Tables*. John Wiley & Sons, Inc., New York, 1948.
5. Lochte-Holtgreven, W., ed. *Plasma Diagnostics*. North Holland Publishing Co., Amsterdam, 1968.
6. Griem, H. R. *Plasma Spectroscopy*. McGraw Hill, New York, 1964.
7. Norton, B. A. and Wooding, E. R. "A Versatile Pulsed Plasma Light Source Operating in the Vacuum Ultraviolet to Visible Wavelength Region." *Journal of Physics E: Scientific Instruments*, Vol. 10, 1977, pp. 493-495.
8. Kinslow, M. "GUMRAP: A Computer Program for Analyzing Molecular Flow in Complex Enclosures." AEDC-TR-79-76 (AD-A080917), February 1980.
9. Chou, T. S. "GUERAP: General Unwanted Energy Rejection Analysis Program User's Manual." SAMSO-TR-72-314, October 1972.
10. Kinslow, M. "A Mathematical Description of Gas-Surface Interactions Based on Reciprocity." *AIAA Journal*, Vol. 14, No. 10, October 1976, pp. 1358-1361.
11. Kinslow, M. "A Mathematical Description of Gas-Surface Interactions Based Upon Reciprocity." Ph.D. Dissertation, Department of Aerospace Engineering, University of Tennessee, Knoxville, August 1972.

12. Raeside, D. E. "An Introduction to Monte Carlo Methods." *American Journal of Physics*, Vol. 42, January 1974, pp. 20-26.
13. Wexler, S. "Deposition of Atomic Beams." *Reviews of Modern Physics*, Vol. 30, No. 2, April 1958, pp. 402-409.
14. Dawbarn, R., Busby, M. R., and Kinslow, M. "Study of High Energy Gases Impinging on Various Cryosurfaces." AEDC-TR-72-33, April 1972.

NOMENCLATURE

A	Spontaneous emission transition probability
E	Energy
g	Statistical weight factor
I	Intensity
i	Current
°K	Degrees Kelvin
k	Boltzmann's constant
m	Mass
T	Temperature
t	Time
v	Velocity
v	Component of velocity
x,y,z	Mutually orthogonal axes
α	Energy accommodation
δ	Divergence angle from normal
θ	Azimuthal angle
λ	Wavelength
ϕ	Elevation angle

SUBSCRIPTS

i Incident

r Reflected

w Wall